Local Magnetism in Strongly Correlated Electron Systems with Orbital Degrees of Freedom

A DISSERTATION
SUBMITTED TO THE FACULTY OF THE GRADUATE SCHOOL
OF THE UNIVERSITY OF MINNESOTA
BY

Samuel Charles Ducatman

IN PARTIAL FULFILLMENT OF THE REQUIREMENTS
FOR THE DEGREE OF
DOCTOR OF PHILOSOPHY

Natalia Perkins

July, 2017

Acknowledgements

There are many people that have earned my gratitude for their contribution to my time in graduate school. I would like to thank my adviser, Natalia Perkins, and my collaborators, Andrey Chubukov, Rafael Fernandes, and Ioannis Rousochatzakis.

I would also like to thank my friends and fellow students, both at University of Wisconsin-Madison, and here at University of Minnesota: Richard Ruiz, Frank Morton Park, Lucas Morton, Cristian Martinez, Chris Anderson, Zach Billy, Tim Lyon, Alberto Hinojosa, Saurabh Mait, Dushko Kuzmanovski, Yuriy Sizyuk, and Brent Perreault. They helped provide me with motivation, dedication, knowledge, and plenty of good ideas for my research. Graduate school was also much more fun with them as friends.

Several professors and staff did not directly help me with my research, but provided me with career advice. In particular, I would like to thank Jim Reardon and Professor Kenneth Heller.

Lastly, I would like thank those closest to me. My parents and brothers provided invaluable support throughout my life and in graduate school. My fiancé, Adelhaide Stanley, has helped me tremendously especially in the past year.

Dedication

To my My fiancé and love, Adelhaide Stanley.

Abstract

The central aim of my research is to explain the connection between the macroscopic behavior and the microscopic physics of strongly correlated electron systems with orbital degrees of freedom through the use of effective models. My dissertation focuses on the sub-class of these materials where electrons appear to be localized by interactions, and magnetic ions have well measured magnetic moments. This suggests that we can capture the low-energy physics of the material by employing a minimal model featuring localized spins which interact with each other through exchange couplings. I describe $Fe_{1+y}Te$ and β-Li_2IrO_3 with effective models primarily focusing on the spins of the magnetic ions, in this case Fe and Ir, respectively. The goal with both materials is to gain insight and make predictions for experimentalists.

In chapter 2, I focus on $Fe_{1+y}Te$. I describe why we believe the magnetic ground state of this material, with an observed Bragg peak at $\mathbf{Q} = (\pm\frac{\pi}{2}, \frac{\pi}{2})$, can be described by a Heisenberg model with 1st, 2nd, and 3rd neighbor interactions. I present two possible ground states of this model in the small J_1 limit, the bicollinear and plaquette states. In order to predict which ground state the model prefers, I calculate the spin wave spectrum with $1/S$ corrections, and I find the model naturally selects the "plaquette state." I give a brief description of the ways this result could be tested using experimental techniques such as polarized neutron scattering.

In chapter 3, I extend the model used in chapter 2. This is necessary because the Heisenberg model we employed cannot explain why $Fe_{1+y}Te$ undergoes a phase transition as y is increased. We add an additional elements to our calculation; we assume that electrons in some of the Fe 3D orbitals have selectively localized while others remain itinerant. We write a new Hamiltonian, where localized moments acquire a new long-range RKKY-like interaction from interactions with the itinerant electrons. We are able to reproduce the phase diagram found from experimentalists, and make predictions about how $Fe_{1+y}Te$ could potentially be driven into a "stripe" magnetic ground state.

In chapter 4, I examine another strongly correlated material, β-Li_2IrO_3, which exhibits Kitaev physics. I begin with a minimal model employing nearest neighbor

isotropic and anisotropic exchange couplings between neighboring Iridium ions. I calculate the phase diagram, and find two states. I characterize both states in terms of spins along the zigzag chains of the hyperhoneycomb lattice, and calculate linear spin waves for both states. I find that, besides for special points in our phase diagram, the excitations are gapped. As the spectrum has many branches, I calculate the dynamic structure factor to find which branches of the spin wave spectrum have the highest intensity. It will be interesting to compare my dynamic structure factor results to single crystal inelastic neutron scattering, which to this point has not been performed for β-Li_2IrO_3.

Contents

Acknowledgements **i**

Dedication **ii**

Abstract **iii**

List of Tables **viii**

List of Figures **ix**

1 Introduction **1**

1.1 The Iron Based Superconductors 3

1.1.1 A Brief History – From BCS to FeSCs 3

1.1.2 Generic Phase Diagram of the FeSCs 4

1.1.3 $Fe_{1+y}Te$ 7

1.1.4 Our results 8

1.2 Magnetism in Systems with Strong Spin-Orbit Coupling 9

1.2.1 The Interplay of Spin-Orbit Coupling and Electronic Correlations 9

1.2.2 Kitaev Physics 11

1.2.3 Our Results for Spin Dynamics in β-Li_2IrO_3 13

1.3 Outline of the Dissertation 14

2 Magnetism in parent Fe-chalcogenides: quantum fluctuations select a plaquette order **16**

2.1 Introduction 16

2.2 Model . . . 20
2.3 Large-S spin-wave calculations . . . 20
2.4 Experimental Signatures of the ODS State . . . 24
2.5 Summary . . . 25
2.6 Technical Details for Chapter 2 . . . 25

3 Theory of the Evolution of Magnetic Order in Fe_{1+y} Te Compounds with Increasing Interstitial Iron 31
3.1 Introduction . . . 31
3.2 Model . . . 34
3.3 Fermi Surface Evolution . . . 36
3.4 Spin Susceptibility of Itinerant Electrons . . . 38
3.4.1 Bare Susceptibility . . . 38
3.4.2 RPA Susceptibility . . . 40
3.5 The RKKY Exchange Integrals . . . 41
3.5.1 Toy Model for the RKKY Interaction . . . 41
3.5.2 RKKY Interactions Computed in a Realistic Model . . . 44
3.5.3 Derivation of Effective Couplings . . . 45
3.6 Classical Phase Diagram . . . 46
3.7 Summary . . . 49
3.8 Technical Details for Chapter 3 . . . 50
3.8.1 Derivation of Biquadratic Exchange Couplings . . . 50
3.8.2 Classical Energy . . . 53

4 Magnetic Excitations in Hyperhoneycomb Kitaev Systems 55
4.1 Introduction . . . 55
4.2 J-K-Γ model on the Hyperhoneycomb Lattice . . . 58
4.3 Classical Phase Diagram from the Luttinger-Tisza Approach . . . 59
4.4 Classical Ground State From the Relaxation Dynamics Simulations . . . 63
4.4.1 K-Dominant State . . . 64
4.4.2 Γ-Dominant State . . . 66
4.4.3 Symmetry Analysis . . . 69
4.5 Spin Wave Excitations . . . 70

4.5.1 Linear Spin Wave Spectra 71
4.5.2 Dynamical Spin-Spin Structure Factor 76
4.6 Conclusion and Discussion 77
4.7 Technical Details for Chapter 4 78
4.7.1 Structure of the Periodicity-3 State 78
4.7.2 Magnetic Symmetry Analysis 78
4.7.3 Explanation of why $\Delta = 0$ along the Γ-K Phase Boundary . . . 81

5 Conclusion and Discussion **84**

References **87**

Appendix A. Glossary and Acronyms **102**
A.1 Glossary 102
A.2 Acronyms 103

List of Tables

A.1 Acronyms 103

List of Figures

1.1 The crystal structure of different families of Iron based superconductors, copyright Elsevier 5
1.2 The crystal and magnetic transistion from a tetragonal paramagnet to an orthorhombic "stripe" SDW, copyright AAAS 6
1.3 Ground state of a generic FeSC vs doping 7
1.4 The effects of spin-orbit coupling on a $\frac{5}{6}$ filled band. 10
1.5 Density profile of a hole in the pseudospin $J_{\text{eff}} = \frac{1}{2}$ state. 11
1.6 Illustration of the possible geometric orientations of neighboring IrO_6 octahedra that give rise to different types of (dominant) exchange interactions between magnetic $J_{\text{eff}} = \frac{1}{2}$ moments. 12
1.7 The harmonic honeycomb lattices. 13
2.1 The two possible collinear configurations for the $J_1 - J_2 - J_3$ model. . 17
2.2 Classically degenerate spin configurations for the J_1-J_2-J_3 model. 19
2.3 Bare and renormalized (1/S) magnon spectrums of the magnetic ground state of a $J_1 - J_2 - J_3$ model. 26
3.1 The fermi surface for $Fe_{1+y}Te$ as we increase chemical potential. 33
3.2 (a)Dependence of chemical potential μ on amount of excess iron y. (b) Orbitally resolved electron occupation numbers. 37
3.3 (The evolution of the bare spin susceptibility $\chi^0(\mathbf{q}, 0)$ and the RPA spin susceptibility $\chi(\mathbf{q}, 0)$ as excess iron y is increased. 39
3.4 Cuts of the bare spin suscptibility and RPA spin susceptibility along symmetry directions. 42
3.5 Static magnetic susceptibility $\chi(q_x, 0)$ and J^{RKKY} for a simple toy model. 43

3.6 The evolution of (a) J_{ij}^{RKKY} and (b) J_{ij}^{eff} with increasing concentrations of excess iron y. 44
3.7 Magnetic phase diagram of our effective model for $Fe_{1+y}Te$ 47
3.8 The possible spin orderings found in the phase diagram in Fig. 3.7, and the respective structure factors for these magnetic orders. 49
3.9 Dominant modes of lattice distortion in $Fe_{1+y}Te$. 54
4.1 The lattice structure of β-Li_2IrO_3. 59
4.2 Classical phase diagram of the J-K-Γ model on the hyperhoneycomb lattice based on the Luttinger-Tisza method. 60
4.3 Local Fields and Angles and spin-spin correlation functions along x-y chains. 64
4.4 The modulation of S^x, S^y and S^z spin components along a single zigzag chain. 67
4.5 Angles between spins along a single x-y chain as a function of the parameter r. 69
4.6 The intensity plot of the dynamical structure factor of our various ground states. 72
4.7 The$\mathbf{q} = 0$ low energy branches linear of the spin wave spectrum $\omega_{\mathbf{q}=0}$ as a function of the parameter r. 74
4.8 Geometry of the K-dominant and Γ-dominant state along a single zigzag chain. 81

Chapter 1

Introduction

Many important achievements have been made in recent years in the field of complex strongly correlated electron materials, where new collective properties emerge due to strong interactions. Among such collective phenomena are magnetism, superconductivity and orbital ordering. A particularly rich physics can be observed in insulating or metallic compounds of transition metals, mostly transition metal oxides [1]. These systems have fascinated chemists and physicists for many decades with their intriguing structural, magnetic and electronic properties. These diverse properties arise from the simultaneous presence of strongly correlated effects and the keen interplay of different degrees of freedom in these systems: charge, spin and orbital ones as well as crystal lattice. The essential feature that defines these materials is the behavior of electrons in these systems cannot be described effectively in terms of non-interacting entities. This is because the Coulomb repulsion between electrons is strong and single-particle description is not sufficient. Obviously, this significantly complicates the theoretical analysis, especially when various interactions are comparable in their energy scales and perturbative approaches do not work.

Numerous approximation schemes have been employed to circumvent these difficulties, but many theorists in the field have learned that a very productive approach to start studying the complex problem is by first considering simple phenomenological models, known as "effective models". A good effective model will still capture the key physics of a problem and allows for at least basic understanding of the strongly correlated electron system. The relative simplicity of effective models allows for the profound theoretical

analysis, and this often helps us to obtain deep physical insights into the low-energy behavior of the system of interest.

The primary objective of my dissertation is the understanding of the role of electronic correlations and multiple degrees of freedom in the formation of various novel quantum states. In my studies, I start by deriving or justifying the effective low-energy models I will employ. I then study their ground states and elementary excitations using analytical field theory and statistical mechanics approaches and by employing various numerical techniques.

There are two main topics included in my dissertation. The first topic is the analysis of magnetism in parent compounds of iron-based superconductors (FeSCs) which is an integral part of the program to understand the origin of superconductivity in these materials. These materials have attracted a lot of attention in past decade because before the year 2008 [2], the term "high-temperature superconductivity "(HTS) was reserved for Cu-based superconductors (CuSC) [3], in which the superconductivity was discovered in 1986. The transformation from the "Copper age" to the "Iron age" was swift and the term HTS now equally applies to both CuSC and Fe-based superconductors (FeSC) [4]. In fact, the FeSC's "splash" was so large that the data obtained for the Fe-pnictides and chalcogenides in the last decade is comparable to the data collected for other known superconductors over several decades. Not surprisingly, many properties of these compounds are not yet understood and require theoretical analysis.

The second part of my dissertation focuses on the study of magnetic excitations in the Kitaev materials [5, 6, 7] – transition metal oxides with partially filled $4d$ and $5d$ shells on the tri-coordinated lattice structures. These materials belong to another class of the most actively studied strongly correlated electron systems. In these systems, the cooperation of electronic correlations and strong spin-orbit coupling (SOC) can lead to the discovery of novel quantum and classical phases.

A particular motivation for my study of the magnetic excitations in such systems comes from recent experimental discoveries of 3D honeycomb materials, β-Li_2IrO_3 and γ-Li_2IrO_3 compounds [8, 9, 10, 11, 12], which exhibit a very unusual counterrotating spiral order. The spin dynamics of these systems remain largely unknown and I hope that my study will help experimentalists in their future explorations.

In the rest of Chapter 1, we discuss some of the history, relevance, and details of the

FeSCs and systems with strong SOC, beginning with the FeSCs.

1.1 The Iron Based Superconductors

1.1.1 A Brief History – From BCS to FeSCs

The history of the superconductivity starts in 1908 when Kamerlingh Onnes prepared liquid helium for the first time. This achievement, extraordinary in itself, allowed researchers to study the properties of matter at temperatures below 4.3 K. Three years later, Kamerlingh Onnes measured the electric properties of pure mercury, and he discovered that the electrical resistance completely disappeared when the mercury was cooled below 4.2 K [13]. This new state of matter was named superconductivity.

Throughout the early and mid-20th century, scientists found more and more materials with gradually increasing critical temperatures (T_c). However, a microscopic theory of the superconductivity was missing and for many years superconductivity remained an intriguing puzzle. The first microscopic theory was proposed by Bardeen, Cooper and Schriffer (BCS) [14, 15, 16]. In this theory, electrons overcome their mutual electrostatic repulsion and bind into pairs (Cooper pairs) [15] due to the electrons' coupling to vibrations of the crystal lattice [14], dubbed electron-phonon coupling. Unlike normal electrons, below the critical temperature the Cooper pairs condense to a single coherent ground state that forms a rigid superfluid electronic liquid that carries current without dissipation.

The understanding of the superconductivity was assumed to be complete until Bednorz and Müller discovered the superconductivity of layered copper oxides [3]. Importantly, the critical temperature of the cuprates was found to be much higher than ever seen before; several copper based superconductors had T_c higher than 77 K, and this could not be explained with BCS theory. The cuprate superconductors were called unconventional high-T_c superconductors and were extensively studied by both theorists and experimentalists.

The discovery of superconductivity in cuprates was the start of an active search for new superconductors. While the cuprates, with $T_c > 77$ K, might seem ideal for superconducting applications, in practice they are brittle ceramics, not easily turned into wires. In 2008, with the discovery of superconductivity in $LaFeAsO_{1-x}F_x$, interest

exploded in the iron based superconductors [2], another class of high-T_c superconductors. Despite the fact that FeSCs exhibit T_c generally lower, but comparable, to ones in cuprates [17, 18, 19], they are less brittle and therefore easier to fashion into wires [20]. This is because the FeSCs are more metallic than the cuprates.

In addition to the potential practical uses, the FeSCs excited the condensed matter community with the possibility of rich new physics. The differences between the FeSCs and the cuprates extend beyond the superconducting phase. Whereas the cuprate undoped parent compounds are understood to settle into Nèel phase at low temperatures; the FeSC undoped parent compounds, in contrast, settle into a "spin-density wave" (SDW) at low temperatures [21]. In most FeSCs, the superconductivity is found in the proximity of a magnetically ordered SDW-state, indicating that magnetic fluctuations play the key role in promoting the superconducting pairing. For this reason, it is important to study the nature of the magnetism in these systems.

1.1.2 Generic Phase Diagram of the FeSCs

In this section we provide the reader with important details about the structure of the (undoped) parent compounds of the FeSCs. Knowing the structure is particularly important for understanding the magnetism of the parent compounds.

As can be seen in Fig. 1.1 and 1.2, the iron atoms layer into basal ab planes with either pnictide or chalcogenide atoms, depending on the chemical composition, placed above or below the iron plane in a checkerboard pattern [22]. There are two iron atoms per unit cell, but most theoretical groups choose to work in the one-iron unit cell, for convenience of working in an unfolded Brillioun Zone (BZ) in momentum space. Furthermore, it is common to treat the systems as "quasi"-2D by working in the ab plane of the iron atoms, although this cannot be done for compounds of the form XFe_2As_2 (X=Na, K, etc) (Fig. 1.1b).

The schematic phase diagram of generic FeSCs is given in Fig. 1.3. A structural transition from a tetragonal ($\mathbf{a} = \mathbf{b}$) to orthorhombic ($\mathbf{a} \neq \mathbf{b}$) crystal symmetry occurs at temperature T_s, here shown in blue. Fig. 1.2 helps us visualize this transistion, the blue arrows show how the lattice expands in the a direction and contracts in the b direction. At this same temperature, the state enters the "nematic phase", where the spin moments break Z_2 symmetry (but not SO(3) symmetry) [24]. Clearly, the same

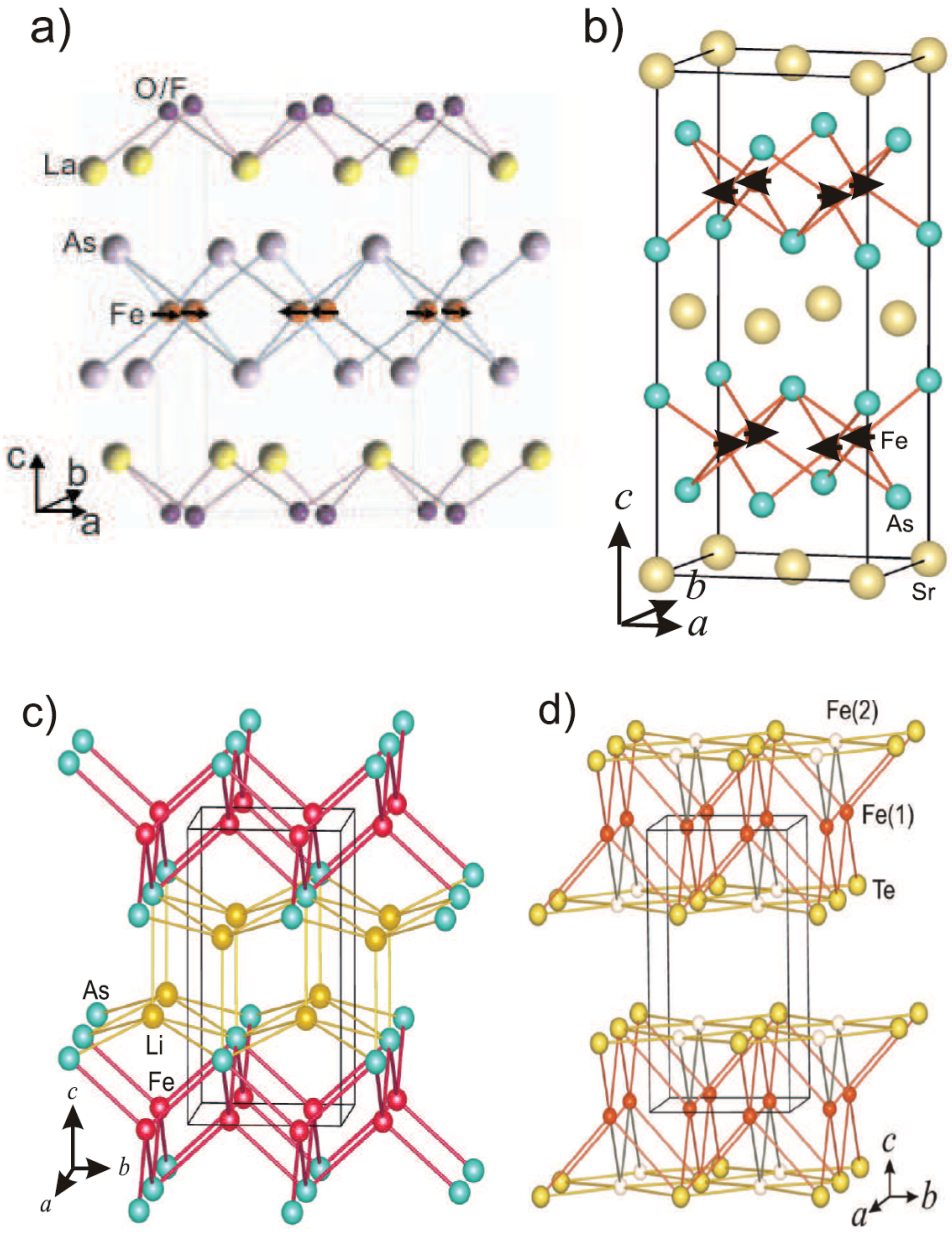

Figure 1.1: The crystal structure of (a) $LaFeAsO_{1-x}F_x$, (b) $SrFe_2As_2$, (c) LiFeAs, (d)$Fe_{1+y}Te$. Notice that each iron atom is tetragonally coordinated by either a pnictide or chalcogenide. At higher temperatures, these compounds have tetragonal unit cells, but at temperatures below T_s, they form orthorhombic unit cells, as in (b). Below T_n, the iron spins form SDW order, as shown in (a)(b), although this can be more clearly seen in 1.2. Notice that (d) has excess iron, placed interstitially in the Tellerium plane. Reprinted from [22], copyright Elsevier.

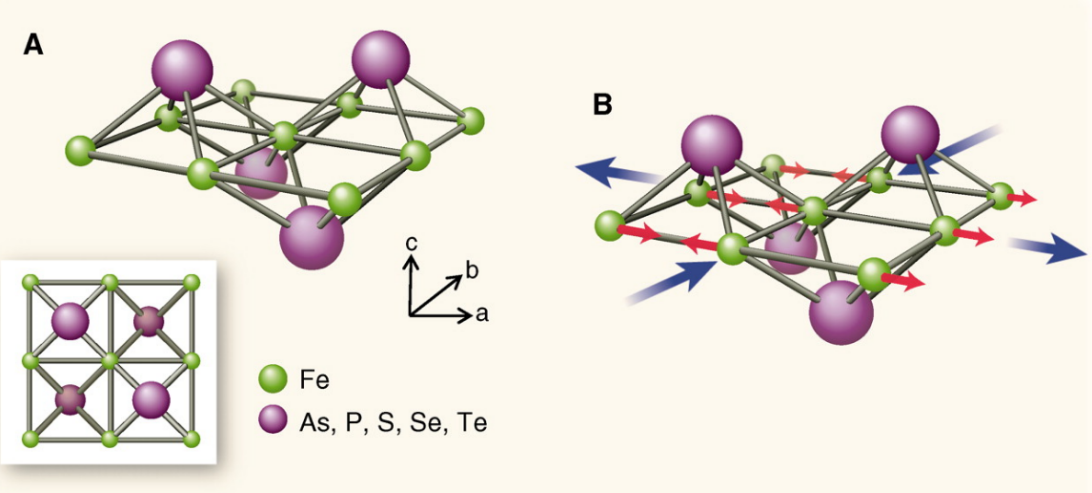

Figure 1.2: (a) Above the T_s, the state has a tetragonal unit cell and is paramagnetic. (b) Below T_s, the state transistions into an orthorhombic unit cell where $a > b$ (blue arrows), and below T_n, the spins order into a "stripe" magnetic order (red arrows), with ferromagnetic stripes in the b direction. Reprinted from [23], copyright AAAS.

lowering of symmetry happening in the structural unit cell and the magnetic moments shows the connection between the two. The transition into the magnetic order, shown in red, occurs at T_N which can happen concurrently or at slightly lower temperatures than T_s (here, it shown at a slightly lower temperature.) The SDW-order, with a wave vector of $\mathbf{Q}$=$(\pi, 0)$ or $(0, \pi)$, breaks both Z_2 and SO(3) symmetries. This magnetic order is commonly known as "stripe" magnetic order, due to the presence of ferromagnetic stripes, and is shown by the red arrows in Fig. 1.2b. The superconducting phase (SC), which can occur due to either electron or hole doping, is shown by the gold domes. Interestingly, the SDW (red) phase can co-exist with the SC phase (gold).

We learn from Fig. 1.3 that it is not enough to study only the superconducting phase of the FeSCs. In order to best understand the origins of high-T_c of doped FeSCS, we must also study the interplay of magnetic and structural properties of the parent compounds.

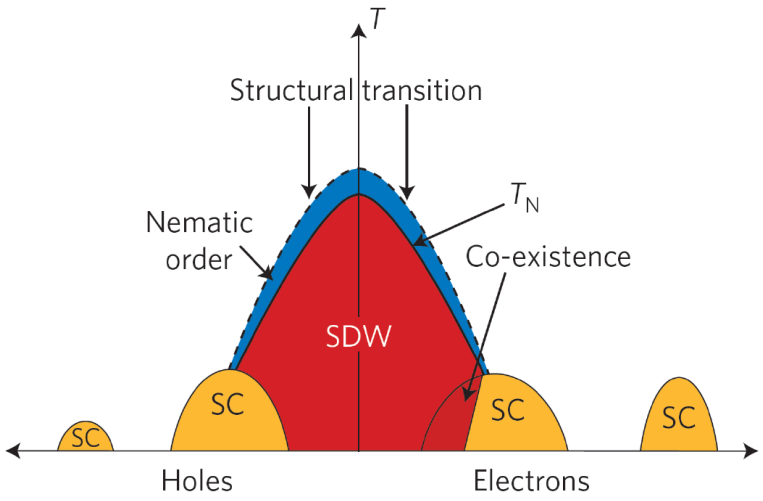

Figure 1.3: The ground state of a generic Iron-based superconductor as a function of doping. The horizontal axis is temperature, the horizontal axis doping. The undoped parent compounds (y-axis) are paramagnets with tetragonal crystal structure at high temperature. As temperatue is lowered, first a phase-transistion to "nematic phase" (blue) with orthorhombic symmetry occurs, and then at T_n a magnetic transistion to a spin-density wave state (red dome). The yellow domes indicate where the doped materials become superconducting. Reproduce with permission from ref. [4]. Copyright Nature Publishing Group.

1.1.3 $\mathbf{Fe_{1+y}Te}$

It seems that the experimental results of FeSC parent compounds are consistent with an effective model of moderately correlated itinerant electrons, which can explain, for example, the SDW "stripe" magnetic order with an ordering vector of $\mathbf{Q} = (\pi, 0)$. This framework is reinforced by the metallic resitivity ρ vs temperature T and the small magnetic moments of the FeSC parent compounds [22].

However, in the 11 family of FeSCs (FeX, X=Se, Te), there is a compound, $Fe_{1+y}Te_{1-x}Se_x$, where a more complicated picture emerges (Fig. 1.1 d). In this formula, there are $1+y$ units Fe per unit chalogenide Te/Se. Optimal doping for SC occurs at x=0.5, and the SC state exhibits spin resonance $\mathbf{Q} = (\pi, 0)$ [25], which fits within the framework described above. However, the parent compound $Fe_{1+y}Te$ magnetically orders with a propagation vector $\mathbf{Q} = (\frac{\pi}{2}, \pm\frac{\pi}{2})$ [26]. In Ref. [26], J. Hu *et al.* further found that at T_n,

$Fe_{1+y}Te$ undergoes a first order phase transistion from a tetragonal paramagnet to the magnetically ordered state with the $\mathbf{Q} = (\frac{\pi}{2},\pm\frac{\pi}{2})$ propagation vector and monoclinic crystal structure. They also found the spins had a magnetic moment of $\approx 2\mu_B$/Fe. Furthermore, the resistivity of $Fe_{1+y}Te$ remains rather flat with T, suggesting non-mettalic behaviour. This indicates that unlike in the other FeSCs, $Fe_{1+y}Te$ can be described with a low energy model of localized spins interacting magnetically through Heisenberg exchanges. First-principle calculations found that $Fe_{1+y}Te$ could be reasonably described by a J_1-J_2-J_3 Heisenberg model [27].

1.1.4 Our results

In chapter 2, we study the magnetic order in Fe-chalcogenides starting from the phenomenological J_1-J_2-J_3 superexchange model [27]. This minimal model does not take into account any structural distortion or effects from excess iron, but nevertheless allows us to capture the main features of the ordering in $Fe_{1+y}Te$. We have shown [28] that the generic magnetic order of $Fe_{1+y}Te$ is not described by a single-$\mathbf{Q}$ vector and can be instead described as a superposition of wavevectors $(\pm\pi/2, \pm\pi/2)$. We also showed that quantum fluctuations stabilize the so-called orthogonal double stripe (ODS) phase which contains two wavevectors $(\pi/2, \pi/2)$ and $(\pi/2, -\pi/2)$. The details of of this analysis are presented in this chapter.

$Fe_{1+y}Te$ cannot be grown without at least some interstitial iron ($y > 0.015$), and one interesting line of research is how varying y changes the the properties of $Fe_{1+y}Te$. Indeed, the magnetic order becomes even more complex upon increasing the excess iron, y. In particular, neutron diffraction results find an incommensurate spiral state, and also possibly a helical state in compounds with larger y. These findings can not be addressed without looking into the microscopic origin of the superexchange processes. In our study [29], we employed a hybrid model with couples localized spins and itinerant electrons [30], with both being present due to orbital-selective localization [31]. In this hybrid model, electrons in the Fe $x^2 - y^2$ and $3z^2 - r^2$ orbitals localize into $S = 1$ moments due to Hund's coupling, but the remaining electrons are treated as itinerant. We use a rigid band approximation for the itinerant electrons, where increasing the excess iron y increases the chemical potential. In addition to the J_1-J_2-J_3 Heisenberg superexchange, local moments acquire an additional long range exchange through the

Ruderman-Kittel-Kasuya-Yosida (RKKY) interaction to the itinerant electrons. The results of this study are presented in chapter 3.

1.2 Magnetism in Systems with Strong Spin-Orbit Coupling

1.2.1 The Interplay of Spin-Orbit Coupling and Electronic Correlations

As we discussed above, in correlated electron systems novel quantum phases and properties often result from an uncommon hierarchy of energy scales. As an example, in magnetic oxides with 5d transition metal ions, such as iridates and osmates, relativistic spin-orbit coupling (SOC) is comparable, or even higher than Coulomb energies [32]. Due to this unusual hierarchy of interactions, physical properties of $5d$-systems differ significantly from those of $3d$-systems [1]. In $3d$-systems, Coulomb interaction and crystal fields are the dominant interactions, and SOC can be treated as a perturbation, whose main role is to give rise to a magnetic anisotropy of either an easy-axis or an easy-plane type. In $5d$-systems, SOC is the dominant interaction rather than a small perturbation, and anisotropic exchange interactions between localized moments do not reduce to conventional easy-plane and easy-axis anisotropies. This is chiefly due to the fact that the form of magnetic interactions is not dictated by spin symmetry alone. Instead, the symmetry of the low-energy Hamiltonians is determined by the combination of spin and lattice symmetries, which opens a possibility to design models with fundamentally new properties [33]. In addition, there is a hope that strong SOC may lead to nontrivial superconductivity [34].

Furthermore, strong SOC may drastically modify the electronic structure; leading to unexpected insulating behavior. It was commonly believed that $5d$-materials should be more metallic and less magnetic than their $3d$- or $4d$-counterparts, in which the localized nature of the $3d$ valence electrons is responsible for the small bandwidth, large correlations, and the suppression of charge fluctuations. This belief was mainly based on the idea that the extended nature of the $5d$ orbitals leads to a broader $5d$–bandwidth and a reduced Coulomb interaction compared to $3d$-systems, and thus $5d$-systems would

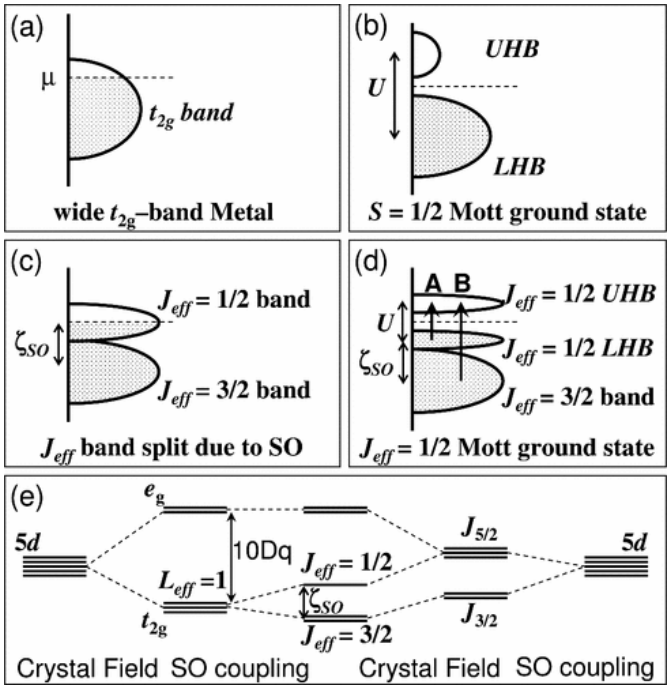

Figure 1.4: (a) The t_{2g} band of Sr_2IrO_4 with 5/6th filling and wide bandwidth. (b) Splitting the band into upper and lower hubbard bands would require an unrealistically strong U. (c) Spin-orbit coupling splits the band into a filled $J_{\text{eff}} = \frac{3}{2}$ band and a half-filled $J_{\text{eff}} = \frac{1}{2}$ band. (d) The $J_{\text{eff}} = \frac{1}{2}$ is much narrower than the original t_{2g} band, so a much smaller U is required to split this band into upper and lower Hubbard bands. (e) An illustration of how the 5d band is first split by crystal field, then S) coupling, and the relevant energy scales. Taken from Ref. [35].

show metallic, paramagnetic behavior. It turns out, however, that many iridates and osmates are Mott insulators or semimetals with non-trivial long-range magnetic orders.

The insulating behavior or iridates in general and, in particular, the insulating behavior of Sr_2IrO_4 [36, 37], which show strong similarity to the parent compound of HTSC cuprates, La_2CuO_4, was understood by Kim *et al.* [35]. They proposed that the key role is played by SOC. Without any interactions, Sr_2IrO_4, which has five electrons in the t_{2g} manifold, would be a metal with 5/6th filling. According to Kim *et al.* [35], splitting of the t_{2_g} into upper and lower Hubbard bands would require unrealistically

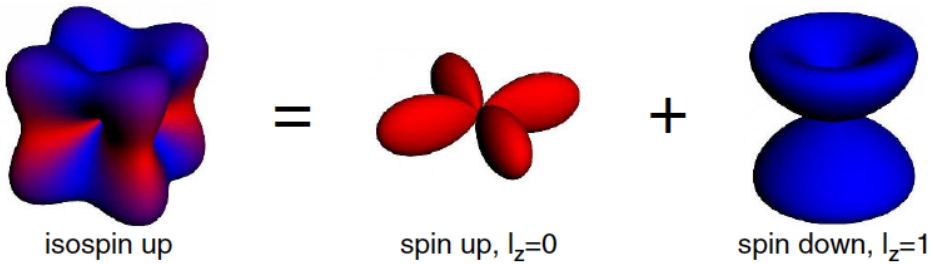

Figure 1.5: Density profile of a hole in the pseudopin-up state. This figure is taken from Ref. [6] .

large magnitude of U. Instead, strong SOC splits the t_{2g} into a filled $J_{\text{eff}} = \frac{3}{2}$ and half-filled $J_{\text{eff}} = \frac{1}{2}$ band. The half-filled $J_{\text{eff}} = \frac{1}{2}$ has much narrower bandwidth as compared to the original t_{2g}, and it can be split into upper and lower Hubbard bands by much weaker U. This process can be seen in Fig. 1.4.

Now, once the charge gap is open and the system is in the Mott-insulated state, the low-energy physics is given by magnetic degrees of freedom, i.e. pseudospins $J_{\text{eff}} = \frac{1}{2}$ moments describing Kramers doublet in which spin and orbital angular momentum are entangled. This entanglement can be clearly seen in Fig. 1.5 showing the density profile of a hole in the pseudospin $J_{\text{eff}} = \frac{1}{2}$, in which peculiar distribution of spin densities in real space is shown by red (spin-up) and blue (spin-down) colors [6].

1.2.2 Kitaev Physics

Once it was understood how some iridates could become Mott insulators, an effort was made to understand the properties of Sr_2IrO_4 and other iridates using effective exchange models of the $J_{\text{eff}} = \frac{1}{2}$ local moments. In 2009, Jackeli and Khaliullin [6] found that the bond geometry of Sr_2IrO_4 led to dominant antiferromagnetic Heisenberg interactions. In addition, they showed that in a different bond geometry realized in A_2IrO_3, effective spin one-half moments interact not only through an isotropic antiferromagnetic Heisenberg exchange interaction, but also through a highly anisotropic ferromagnetic Kitaev exchange interaction. The illustration of possible geometric orientations of neighboring IrO_6 octahedra that give rise to different types of (dominant) exchange interactions

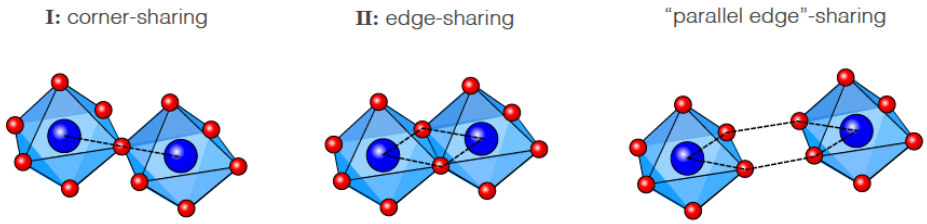

Figure 1.6: Illustration of the possible geometric orientations of neighboring IrO_6 octahedra that give rise to different types of (dominant) exchange interactions between the magnetic moments located on the iridium ion at the center of these octahedra. For the corner-sharing geometry (I) one finds a dominant symmetric Heisenberg exchange; while for the edge-sharing geometries (II), one finds a dominant bond-directional, Kitaev-type exchange. This figure is taken from Ref. [7] .

between magnetic $J_{\text{eff}} = \frac{1}{2}$ moments is given in Fig.1.6.

The Hamiltonian with purely Kitaev interactions on a honeycomb lattice [5] or on any other tricoordinated lattices with 120° bond angles [38] is exactly solvable and its ground state is a quantum spin liquid (QSL) [5]. It is important to note here that QSLs have potential applications in quantum computing, and exhibit unusual and exciting physics such as topological order, fractional excitations, and Majorana fermions. For this reason, there was greatd deal of excitement concerning the edge sharing iridates, since they were seen as QSL candidates.

However, all of the known Kitaev magnets, α-,β- and γ -Li_2IrO_3, α-Na_2IrO_3 and α-$RuCl_3$, order magnetically at low enough temperatures despite the growing experimental evidence that the dominant interaction in all these compounds is precisely the bond-directional Kitaev anisotropy that drives the QSL behavior [5]. Nevertheless, the magnetic ground states that can be realized in these materials are far from being trivial; therefore Kitaev materials provide ample opportunity to study other unconventional forms of magnetism.

Our particular interest is in the three-dimensional Kitaev materials. The exploration of three-dimensional Kitaev materials was started with the independent, but almost concurrent synthesis of two polymorphs of Li_2IrO_3 [8, 9, 10, 11], belonging to the family harmonic honeycomb series $\mathcal{H}_n$: β-Li_2IrO_3 corresponds to $\mathcal{H}_0$ and γ-Li_2IrO_3 corresponds

to $\mathcal{H}_1$. The family of harmonic honeycomb series $\mathcal{H}_n$ consists of bipartite orthorhombic tri-coordinated 3D lattices. The $\mathcal{H}_n$ lattice consists of n rows of coplanar hexagonal plaquettes, followed by a "bridge" layer of c-axis bonds, and then another n rows in a new plane (see Fig. 1.7).

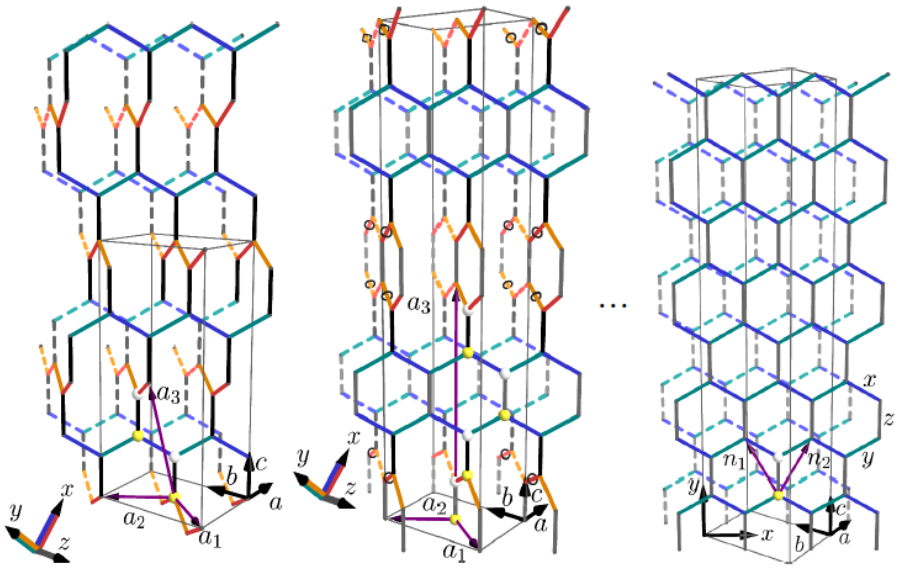

Figure 1.7: The harmonic honeycomb lattices: $\mathcal{H}_0$ (left), $\mathcal{H}_1$ (center), $\mathcal{H}_\infty$(right). Here n counts the number of rows along the c-axis before the orientation of the honeycomb plane switches between the two non-parallel chains of x and y bonds. The $\mathcal{H}_0$ hyperhoneycomb lattice switches chains at every c-bond. The $\mathcal{H}_1$ has one set of c-bonds making rungs (gray) of ladders before a bridge (c-bonds in black) to the opposite ladder. The $\mathcal{H}_\infty$ never switches ladders. The ladders are labeled by red(orange) and blue(green) on $x(y)$-bonds. The primitive unit cell for $n < \infty$ contains $4n+4$ sites. This figure is taken from Ref. [39] .

1.2.3 Our Results for Spin Dynamics in β-Li_2IrO_3

In particular, we focus on the analysis of the microscopic origin and the dynamics of the counterrotating spiral order observed in the β-Li_2IrO_3 compound. Robustly identifying the properties of such a complex magnetic order is rather challenging from both experimental and theoretical perspectives. In chapter 4 we presents the results of

our study. We begin with a minimal J-K-Γ model describing the essential physics in β-Li_2IrO_3 [40, 41]. Our ultimate goal is to compute the spin dynamics in this compound without being restricted to a single zigzag chain, since not all of the features of the experimentally observed ground state can be captured with a one-chain approach. This is, apparently, not an easy task. The computation of spin dynamics is tricky even when all magnetic moments rotate uniformly, through the same **Q**-wavevector. It is, certainly significantly more challenging when a magnetic order consists of a collection of counterrotating incommensurate spirals. To attack this problem, we search for the simplest commensurate state which has the same irreducible representation, similar periodicity, and bears the main feature of the experimentally observed ground state, i.e., the counterrotation. We computed the phase diagram as a function of the relative strengths between the competing isotropic and anisotropic interactions. We found two different ground states in two neighboring regions of the phase diagram matching the main features of experiment, and categorize the differences between these two phases. Neither were single-**Q** states in the structural unit cell, but both were commensurate in an enlarged magnetic unit cell. Finally, we computed the linear spin wave and the predicted inelastic scattering intensity for these states.

1.3 Outline of the Dissertation

Below, I sketch a brief outline of my dissertation:

- In chapter 2, I use a J_1-J_2-J_3 model to describe the low energy physics of $Fe_{1+y}Te$, I introduce the Holstein-Primakoff transformation to calculate spin waves, and I discuss the role of $1/S$ corrections.

- In chapter 3, I expand my model for $Fe_{1+y}Te$ by including itinerant electrons, which are coupled to the local moments through Hund's coupling. This leads to a long range RKKY interaction that I argue is the key to the understanding of the evolution of $Fe_{1+y}Te$ as we increase y. I also briefly touch on the role of magnetoelastic couplings in this system.

- In chapter 4, I use a J-K-Γ model to describe the low-energy physics of β-Li_2IrO_3. I find two possible commensurate ground states in the phase diagram, I describe

the key features of these ground states, and I calculate linear spin waves and the dynamical structure factor for both possible states.

- In chapter 5, I give a brief conclusion and discussion.

Chapter 2

Magnetism in parent Fe-chalcogenides: quantum fluctuations select a plaquette order

2.1 Introduction

The analysis of magnetism in parent compounds of iron-based superconductors (FeSCs) is an integral part of the program to understand the origin of superconductivity in these materials [17, 22, 42, 43, 44, 45, 46, 47, 48, 49, 50, 51]. Parent compounds of Fe-pnictides are moderately correlated metals, whose resistivity increases with increasing T, and the electronic structure is at least qualitatively consistent with that of free electrons on a lattice [4, 45]. Magnetic order in such systems can be reasonably well understood within itinerant scenario [47, 48, 49, 52] due to enhancement of free-electron susceptibility at momenta connecting hole and electron Fermi surfaces (FSs). The locations of the FSs select two possible momenta for the order – $(0, \pi)$ and $(\pi, 0)$– in the Fe-only Brillouin zone (BZ). Electron-electron interaction and the shape of the FSs further reduce the ground state manifold to single-momentum states with either $(0, \pi)$ or $(\pi, 0)$, but not their mixture [49]). In each of these two states spins are ordered in a stripe fashion –

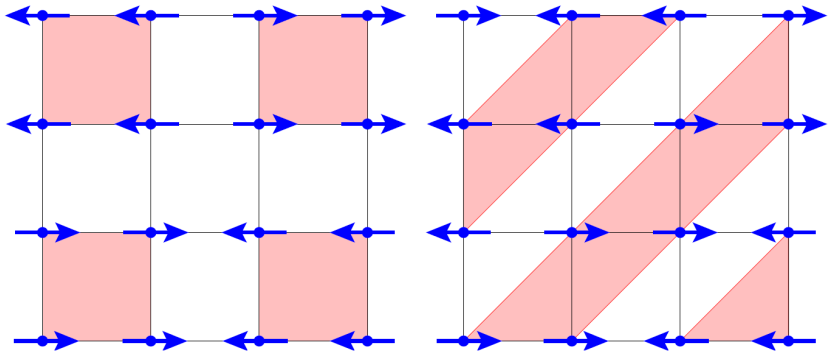

Figure 2.1: The two possible collinear configurations for the J_1-J_2-J_3 model: (a) orthogonal double stripe (ODS) and (b) diagonal double stripe (DDS).

ferromagnetically along one direction in 2D Fe-plane and antiferromagnetically in the other. Such an order breaks C_4 lattice rotational symmetry and causes pre-emptive spin-nematic order [53]. The same magnetic order is selected in the strong coupling approach, which assumes that the system is not far from Mott transition, and magnetic properties are reasonably well described by $J_1 - J_2$ model with nearest and second-nearest neighbor spin exchange [54, 55]. The actual coupling in Fe-pnicties is neither truly small nor strong enough to cause Mott insulating behavior [4], which makes it extremely useful that the two descriptions agree. Upon doping, long-range order is lost, but magnetic fluctuations evolve smoothly and remain peaked at or near $(0, \pi)$ and $(\pi, 0)$ even beyond optimal doping.

There is one family of FeSCs - 11 Fe-chalcogenides $Fe_{1+y}Te_{1-x}Se_x$, in which smooth evolution between parent and optimally doped compounds does not hold. Magnetism in these materials changes considerably between $x = 0$ and $x \sim 0.5$, where the T_c is the largest. Near optimal doping magnetic fluctuations are peaked at or near $(0, \pi)$ and $(\pi, 0)$, as in Fe-pnictides, while magnetic order in a parent compound $Fe_{1+y}Te$ has very different momenta $\pm(\pi/2, \pm\pi/2)$ [26, 25, 56, 57, 58]. Upon doping, the spectral weight at $\pm(\pi/2, \pm\pi/2)$ decreases, and the spectral weight at $(0, \pi)$ and $(\pi, 0)$ increases [25]. The transport properties of $Fe_{1+y}Te$ are also quite different from those of parent compounds of Fe-pnictides: the resistivity, $\rho(T)$, of $Fe_{1+y}Te$ does not show a prominent

increase with increasing T, but instead remains flat and even shows a small increase as T decreases [59]. ARPES studies of $Fe_{1+y}Te$ show that low-energy spectra are very broad [60], consistent with the notion that electrons are not propagating. These observations lead several groups to suggest that parent Fe-chalcogenides are more correlated than parent Fe-pnictides, and magnetism in $Fe_{1+y}Te$ can be understood by assuming that electrons are "almost" localized and interact magnetically via a Heisenberg exchange [27, 61, 62, 63]. This scenario is in line with a more generic idea [64, 65, 66] that in any FeSc, a certain percentage of electronic states are localized and phase separated from itinerant electrons, and the percentage of localized states varies between different materials. An alternative scenario for FeTe, which we don't discuss here, is orbital order[67]

In this chapter we apply the localized electron scenario to $Fe_{1+y}Te$ and verify whether the observed commensurate $\pm(\pi/2, \pm\pi/2)$ order can be obtained in a Heisenberg model with exchange interactions up to third neighbors. Classically, $\pm(\pi/2, \pm\pi/2)$ order is unstable with respect to a spiral order for any non-zero first neighbor exchange, unless one artificially breaks C_4 symmetry and sets interactions to be spatially anisotropic [65, 56]. We analyze the isotropic quantum Heisenberg model and show that quantum fluctuations do stabilize a commensurate $\pm(\pi/2, \pm\pi/2)$ order in some range of parameters. However, this stabilization does not uniquely determine spin configuration as a generic $\pm(\pi/2, \pm\pi/2)$ order is a superposition of two different $Q-$vectors: $\mathbf{Q}_1 = (\pi/2, -\pi/2)$, and $\mathbf{Q}_2 = (\pi/2, \pi/2)$: $\mathbf{S}(\mathbf{r}) = \mathbf{\Delta}_1 \cos \mathbf{Q}_1\mathbf{r} + \mathbf{\Delta}_1^{'} \sin \mathbf{Q}_1\mathbf{r} + \mathbf{\Delta}_2 \cos \mathbf{Q}_2\mathbf{r} + \mathbf{\Delta}_2^{'} \sin \mathbf{Q}_2\mathbf{r}$, with $|\mathbf{\Delta}_i| = |\mathbf{\Delta}_i^{'}| = \Delta$ and $\mathbf{\Delta}_1 \cdot \mathbf{\Delta}_2 = \mathbf{\Delta}_1^{'} \cdot \mathbf{\Delta}_2^{'} = 0$. In Fig. 2.1 we show two prototypical commensurate spin configurations – a single Q bi-collinear spin order ($\mathbf{\Delta}_1 = \mathbf{\Delta}_1^{'} = \mathbf{\Delta}$, $\mathbf{\Delta}_2 = \mathbf{\Delta}_2^{'} = 0$), which breaks C_4, and a double Q plaquette order ($\mathbf{\Delta}_1^{'} = \mathbf{\Delta}_2 = \mathbf{\Delta}$, $\mathbf{\Delta}_1 = \mathbf{\Delta}_2^{'} = 0$), which preserves C_4 symmetry, but breaks Z_4 translational symmetry (four equivalent plaquette states are obtained by moving a black square in Fig. 2.1a by one lattice site in either x or y direction). Bi-collinear spin order is often called diagonal double stripe (DDS), and plaquette order is called orthogonal double stripe (ODS), and we use these notations below. The real-space configuration for both orders is "up-up-down-down" along x and y directions.

Most of previous theoretical and experimental works assumed that the commensurate order is DDS [22] and studied in detail the feedback from this order on electrons

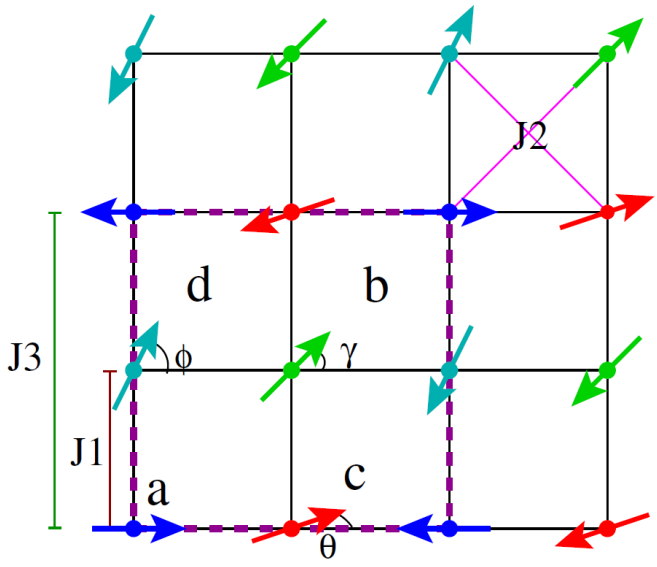

Figure 2.2: Spin order in the classical J_1-J_2-J_3 model at $J_1 = 0$. Classically degenerate configurations form four sublattices, labeled as a, b, c, and d. A configuration with arbitrary γ, θ, and ϕ is a ground state. In our notations, sublattice spins are $\mathbf{\Delta}_1 + \mathbf{\Delta}_2$, $\mathbf{\Delta}_1 - \mathbf{\Delta}_2$, $\mathbf{\Delta}_1^{'} - \mathbf{\Delta}_2^{'}$, and $\mathbf{\Delta}_1^{'} + \mathbf{\Delta}_2^{'}$, respectively.

[56]. We argue that quantum fluctuations of spins actually select ODS order as a stable collinear state for weak but finite nearest-neighbor exchange J_1, while DDS state is unstable for any non-zero J_1. The DDS and the ODS orders have qualitatively different forms of the static structure factor $S(q)$ (two peaks vs four peaks), but this is difficult to detect in real materials because of domains. The authors of [57] however argued that form of $S(q)$ in a paramagnetic phase allows one to distinguish between DDS and ODS, even in the presence of domains, and found that their results are consistent with strong ODS fluctuations. Another argument in favor of the C_4 preserving ODS spin order is the absence of orthogonal distortion in $Fe_{1+y}Te$ – there is a monoclinic distortion below T_N, but this does not break rotational in-plane C_4 symmetry. There is also numerical evidence – ODS order has been found in exact diagonalization studies of J_1-J_2-J_3 model on clusters up to 36 spins [68]. The same ODS order has been found in the mean-field studies of the t-J model in another Fe-chalcogenide $K_{0.8}Fe_{1.6}Se_2$ [69].

2.2 Model

We follow earlier works and model magnetic interactions in $Fe_{1+y}Te$ by a J_1-J_2-J_3 Heisenberg model [27, 62, 68, 70]:

$$H = \sum_{n=1}^{3} J_n \sum_{\langle ij \rangle} \mathbf{S}_i \cdot \mathbf{S}_{i+n} \tag{2.1}$$

where J_1, J_2, and J_3 are antiferromagnetic exchange couplings between first-, second-, and third-nearest neighbors. For $Fe_{1+y}Te$ the values of J_1, J_2, and J_3 have been estimated in [27] and found to be in the range $J_3 > \frac{J_2}{2} \gg J_1$. In this limit, the classical ground state of Eq. 2.1 is a spiral with the pitch vector $\mathbf{Q} = (\pm q, \pm q)$, where $q = \arccos(\frac{-J_1}{2J_2+4J_3})$ [71]. At $J_1 = 0$, the model has an extensive degeneracy, and any order with momentum $\pm(\pi/2, \pm\pi/2)$ is the classical ground state, including DDS, ODS, and an infinite number of other four-sublattice states (Fig. 2.2).

We consider here what happens in the quantum model, at a finite J_1. We show that the ODS state is unambiguously selected by quantum fluctuations to be the ground state in some range of J_1, before a spiral order sets in. Our key reasoning is that only some classically degenerate ground states at $J_1 = 0$ are degenerate by symmetry; others are "accidentally degenerate". The situation is quite similar to the one in the well-known J_1-J_2 model at $J_2 > J_1/2$ [72, 73, 74]. We argue that quantum fluctuations lift accidental degeneracies and gap out some of the spin-wave modes which in the classical limit become unstable (imaginary) at $J_1 \neq 0$. For the DDS state the lifting of the accidental degeneracies does not help, as the modes which become unstable at a finite J_1 are the true Goldstone modes at $J_1 = 0$. On the other hand, for ODS state classically unstable modes are accidental zero modes at $J_1 = 0$, and quantum fluctuations lift the energies of these modes to finite values, making ODS the state stable in a finite range of J_1. We verified that ODS state is indeed the ground state in this range.

2.3 Large-S spin-wave calculations

We consider large value of spin S and study the role of quantum fluctuations within $1/S$ expansion. The computational steps are presented in section 2.6. For $J_1 = 0$, spins on even and odd sites form two non-interacting sublattices, each described by J_2-J_3 model.

This model is identical to "J_1-J_2" model, with diagonal hopping J_2 playing the role of "J_1" and third-neighbor hopping J_3 playing the role of "J_2". One can use this analogy and borrow the results of the quantum analysis of "J_1-J_2" model [72, 73, 74]. For $J_3 > J_2/2$ (which holds in $Fe_{1+y}Te$), quantum fluctuations select stripe configurations within each sublattice, i.e. the angle γ in Fig. 2.2 is locked at $\gamma = 0$ or $\gamma = \pi$, and the angle θ is locked at $\theta = \phi$ or $\theta = \pi + \phi$. The states with $\gamma = 0$ and $\gamma = \pi$ are equivalent up to an interchange of X and Y directions, and below we set $\gamma = 0$. The collinear DDS and ODS states belong to the manifold of selected states and correspond to different locking of the angle ϕ between the nearest-neighbor spins: DDS state corresponds to $\phi = 0, \theta = \pi$ or $\phi = \pi, \theta = 0$, while ODS corresponds to $\phi = \theta = 0$ or $\phi = \theta = \pi$.

To analyze whether a generic state selected by quantum fluctuations at $J_1 = 0$ remains stable at a finite value of J_1, we need to know its excitation spectrum. At $J_1 = 0$, spins on even and odd sites are decoupled, each sublattice is described by its own bose field ($\alpha_{\mathbf{k}}$ for even sites and $\beta_{\mathbf{k}}$ for odd sites), and spin-wave excitations are described by

$$H_{sw} = S(\Omega_{\alpha\mathbf{k}}\alpha^\dagger_{\mathbf{k}}\alpha_{\mathbf{k}} + \Omega_{\beta\mathbf{k}}\beta^\dagger_{\mathbf{k}}\beta_{\mathbf{k}}), \tag{2.2}$$

The classical spin-wave spectrum is the same for all selected states

$$\begin{aligned} &\Omega_{\mathbf{k}} = S(A^2_{\mathbf{k}} - B^2_{\mathbf{k}})^{1/2},\ A_{\mathbf{k}} = 4J_3 + 2J_2\cos(k_x + k_y), \\ &B_{\mathbf{k}} = 2J_2(\cos 2k_x + \cos 2k_y) + 2J_2\cos(k_x - k_y). \end{aligned} \tag{2.3}$$

This spectrum contains nodes at $\pm(\pi/2, \pm\pi/2)$, but some of them are not symmetry-related and are lifted by quantum fluctuations. For the sublattice made of even sites, the order has momentum $\pm(\pi/2, -\pi/2)$ (Fig. 2.2 b), hence the true nodes are located only at these momenta, while the ones at $\pm(\pi/2, \pi/2)$ must be lifted. For the sublattice made out of spins at odd sites, the order has momentum $\pm(\pi/2, \pi/2)$ if we take $\theta = \phi$, like in the ODS, and $\pm(\pi/2, -\pi/2)$ if we take $\theta = \pi + \phi$, like in the DDS. Quantum fluctuations then must lift the nodes at $\pm(\pi/2, -\pi/2)$ and at $\pm(\pi/2, \pi/2)$ for the ODS and the DDS state, respectively. We computed quantum corrections to the spectrum in Eq. 2.3 within perturbation theory to order $1/S$ and indeed found that accidental nodes are lifted by quantum fluctuations and only true Goldstone modes remain (see section 2.6 for details on 1/S corrections).

We next set J_1 to be small but finite and consider which of stripe states, if any, remain stable. The qualitative reasoning is the following: a non-zero J_1 couples the two sublattices and adds to the Hamiltonian (Eq. 2.2) the terms in the form $\alpha^\dagger_{\mathbf{k}}\beta_{\mathbf{k}}$ and $\alpha_{\mathbf{k}}\beta_{\mathbf{k}}$. For the DDS state (or, more accurately, for the DDS family of states as we keep ϕ as a parameter) the stripes on even and odd sites are directed parallel to each other, and the dispersions of $\alpha_{\mathbf{k}}$ and $\beta_{\mathbf{k}}$ fields are identical, including $O(1/S)$ terms. The two dispersions are then gapless at the same momenta $\mathbf{k} = \pm(\pi/2, -\pi/2)$. Around these $\mathbf{k}$ points, the perturbation theory in J_1 is singular, as there is no symmetry requirement which would force the coupling to vanish at $\pm(\pi/2, -\pi/2)$. As a result, the excitations become purely imaginary close enough to $\pm(\pi/2, -\pi/2)$, which implies that the DDS states are unstable at any non-zero J_1. On the other hand, for the ODS family of states, the dispersions $\Omega^\alpha_{\mathbf{k}}$ and $\Omega^\beta_{\mathbf{k}}$ have nodes at different momenta, $\pm(\pi/2, -\pi/2)$ and $\pm(\pi/2, \pi/2)$, respectively. Because of this disparity, perturbation theory near either $\pm(\pi/2, -\pi/2)$ or $\pm(\pi/2, \pi/2)$ is not singular, and corrections in J_1 only gradually shift the values of spin-wave velocities thus keeping ODS states stable.

We verified this reasoning by explicit calculations. We first obtained the J_1-induced interaction in terms of the original Holstein-Primakoff bosons and then re-expressed it in terms of $\alpha_{\mathbf{k}}$ and $\beta_{\mathbf{k}}$ bosons from Eq. 2.2, which are related to the original ones by Bogoliubov transformation. The $u_{\mathbf{k}}v_{\mathbf{k}}$-coefficients of this transformation dress up the interaction terms. For the DDS states, expanding the Hamltonian near the true Goldstone points at $(\pi/2, -\pi/2)$ as $\mathbf{k} = (\pi/2, -\pi/2) + \tilde{\mathbf{k}}$ we obtain $H_{DDS} = H_{sw} + \delta H_{DDS}$, where H_{sw} is given in Eq. 2.2 with

$$\Omega^\alpha_{\tilde{\mathbf{k}}} = \Omega^\beta_{\tilde{\mathbf{k}}} \approx 4S\sqrt{J_3(2J_3 + J_2)}(\tilde{k}_x^2 + \tilde{k}_y^2 - 2a\tilde{k}_x\tilde{k}_y)^{1/2}, \tag{2.4}$$

where $a = \frac{J_2}{2J_3} < 1$, and

$$\delta H_{DDS} = \Delta^{DDS}_{\tilde{\mathbf{k}}}(\alpha^\dagger_{\tilde{\mathbf{k}}}\beta_{\tilde{\mathbf{k}}} + \alpha_{\tilde{\mathbf{k}}}\beta_{-\tilde{\mathbf{k}}} + h.c) \tag{2.5}$$

where

$$\Delta^{DDS}_{\tilde{\mathbf{k}}} = \frac{J_1 S}{2}\left(\frac{2J_3 + J_2}{J_3}\right)^{1/2}\frac{\tilde{k}_y - \tilde{k}_x}{(\tilde{k}_x^2 + \tilde{k}_y^2 - 2a\tilde{k}_x\tilde{k}_y)^{1/2}} \tag{2.6}$$

The coupling term remains finite when $\tilde{k}_{x,y}$ tends to zero, except for special directions. Diagonalizing Eq. 2.5, we find that at low enough $\tilde{k}$ one of the two solutions is $E^2_{\tilde{k}} \approx$

$-2\Omega^{\alpha(\beta)}_{\tilde{\mathbf{k}}}\Delta^{DDS}_{\mathbf{k}}$. A negative $E^2_{\tilde{k}}$ implies that fluctuations around a DDS state grow exponentially with time and make this family of states unstable.

For the ODS states the situation is different because near any of the points $\pm(\pi/2,-\pi/2)$ or $\pm(\pi/2,\pi/2)$, the zero in one of the spin-wave branches is lifted by quantum fluctuations. For example, near $(-\pi/2,\pi/2)$ expanding of the Hamiltonian again gives $H_{ODS}=H_{sw}+\delta H_{ODS}$, however now only $\Omega^{\alpha}_{\tilde{\mathbf{k}}}$ is gapless, while $\Omega^{\beta}_{\tilde{\mathbf{k}}}$ is gapped with the gap of the order $1/S$. The interaction term δH_{ODS} has the same form as in Eq. 2.5, but with

$$\Delta^{ODS}_{\tilde{\mathbf{k}}}=2J_1S^2(2J_3+J_2)\frac{\tilde{k}_y-\tilde{k}_x}{(\Omega^{\alpha}_{\tilde{k}}\Omega^{\beta}_{\tilde{k}})^{1/2}}=O\left(J_1S^{3/2}|\tilde{k}|^{1/2}\right). \tag{2.7}$$

Diagonalizing H_{ODS} we find two solutions,

$$\begin{aligned} E^2_{1,2} &= \frac{1}{2}\Big((\Omega^{\alpha}_{\tilde{k}})^2+(\Omega^{\beta}_{\tilde{k}})^2 \\ &\quad \pm\sqrt{((\Omega^{\alpha}_{\tilde{k}})^2-(\Omega^{\beta}_{\tilde{k}})^2)^2+16(\Delta^{ODS}_{\tilde{\mathbf{k}}})^2\Omega^{\alpha}_{\tilde{k}}.\Omega^{\beta}_{\tilde{k}}}\Big). \end{aligned} \tag{2.8}$$

One of the solutions is gapped to order $1/S$, the other is linear in $\tilde{k}$ with a stiffness which differs from its value at $J_1=0$ by $O(J_1S/J_3)$. We see that the ODS states are stable (for any ϕ) as long as J_1S/J_3 is small.

On a more careful look, we find that the ODS spin order allows for J_1-induced umklapp processes, which also renormalize the dispersions of the ODS states. Indeed, because ODS state breaks Z_4 translational symmetry, the J_1 interaction contains not only the terms at zero transferred momentum, as in Eq. 2.5, but also terms with momentum transfer in multiples of π along each axis. Near $k=(\pi/2,-\pi/2)$, the most relevant of such umklapp terms is the one with momentum $\bar{Q}=(0,\pi)$, which connects a gapless $\alpha_{\tilde{k}}$ boson at $(\pi/2,-\pi/2)$, and a gapless $\beta_{\tilde{k}}$ boson at $(\pi/2,\pi/2)$. However, because breaking of Z_4 is equivalent to breaking local inversion symmetry (a reflection around one column or one row in Fig. 2.1a, the umklapp vertices $\Delta^{U,ODS}_{\tilde{\mathbf{k}}}$ contain extra momentum gradient compared to non-umklapp vertices. In explicit form, we find at small $\tilde{\mathbf{k}}=\mathbf{k}-(\pi/2,-\pi/2)$,

$$\Delta^{U,ODS}_{\tilde{\mathbf{k}}}=-i\frac{J_1}{4}\left(\frac{\Omega^{\alpha}_{\tilde{k}}\Omega^{\beta}_{\tilde{k}+\bar{Q}}}{4J_3^2-J_2^2}\right)^{1/2}\cos\phi\ , \tag{2.9}$$

where $\Omega^{\alpha}_{\tilde{k}}, \Omega^{\beta}_{\tilde{k}+\mathbf{Q}} = 4S(J_3(2J_3 \pm J_2))^{1/2}(\tilde{k}_x^2 + \tilde{k}_y^2 \mp 2\tilde{k}_x\tilde{k}_y)^{1/2}$ and the angle ϕ specifies the spin order within the ODS family of states. We see that $\Delta^{U,ODS}_{\tilde{\mathbf{k}}}$ scales linearly with $\tilde{\mathbf{k}}$, i.e., is of the same order as $\Omega^{\alpha\beta}_{\tilde{k}}$. We computed the corrections to spin-wave velocity and found that they scale as $J_1/\sqrt{4J_3^2 - J_1^2}$, i.e., are small. At the same time, we see from Eq. 2.9 that $\Delta^{U,ODS}_{\tilde{\mathbf{k}}}$ depends on the angle ϕ. Respectively, the corrections to the ground state energy also depend on ϕ and should select which state within the ODS family has the lowest energy. The computation is straightforward and yields $\Delta E_{gr} = -A\cos^2\phi$, with $A > 0$. We see that the collinear ODS state, for which $\phi = 0$ or π, is indeed the state with the lowest energy.

The outcome of our analysis is that the collinear ODS state remains stable and has the lowest energy within a family of similar states. At small J_1, the ODS state has a finite stiffness towards fluctuations which tend to break collinear order in favor of a spiral one. The ODS state remains stable up to $J_1 \sim J_3/S$, at larger J_1 the stiffness changes sign, and the system develops a spiral order.

2.4 Experimental Signatures of the ODS State

Because the ODS state does not break C_4 translational symmetry, it does not cause a pre-emptive spin-nematic order, in contrast to parent compounds of other FeSCs [53]. The data for $Fe_{1+y}Te$ show that the system develops a monoclinic distortion below a certain T, but in-plane C_4 symmetry remains unbroken (it only breaks in doped compounds $Fe_{1+y}Te_{1-x}Se_x$ with $x > 0.5$ [59]). The unbroken C_4 symmetry in the ordered state also manifests itself in the C_4 symmetry of the static structure factor $S(q)$ obtained in neutron scattering experiments [57]. We computed $S(q)$ for both the DDS and the ODS states, and we indeed found that the structure factor for the ODS order has four identical peaks at $(\pm\pi/2, \pm\pi/2)$, while the structure factor for the DDS state has only two peaks at $(\pi/2, -\pi/2)$ and $(-\pi/2, \pi/2)$. While the observed four peaks are consistent with ODS, we caution that the absence of the anisotropy in the structure factor obtained in neutron scattering could be due to the twinning of the crystal. However, as the magnetic domain's structure of the crystal can be controlled using polarized neutrons, the careful analysis of the neutron scattering data might dissect the contribution from different domains. The authors of Ref. [57] made

another argument that, even in a twinned crystal, the form of $S(q)$ throughout the Brillouin zone differentiates between strong DDS and ODS fluctuations, and argued that their data are more consistent with tendency towards ODS order. This again agrees with our results.

2.5 Summary

In this communication we analyzed the type of magnetic order in $Fe_{1+y}Te$ – the parent compound in a family of Fe-chalcogenide superconductors. The magnetic order in this material is different from in other parent compounds of FeSCs – spins are ordered in up-up-down-down fashion (Fig. 2.2). Experiments show [59, 75] that the tendency towards Mott physics is stronger in $Fe_{1+y}Te$ than in other parent compounds of FeSCs, suggesting that the magnetic order in $Fe_{1+y}Te$ can be reasonably well understood within the localized scenario by solving the Heisenberg model with exchange interaction extending up to third neighbors [27]. Several groups argued [27, 26, 56, 76] that the ordered up-up-down-down spin configuration is diagonal double stripe. Such an order breaks C_4 lattice rotational symmetry. We argued, based on our analysis of quantum fluctuations in the Heisenberg model with first, second, and third-neighbor exchange, that such a state is unstable, but another up-up-down-down state – the orthogonal double stripe, is stable and is the ground state in some parameter range. This state (which is also called a plaquette state) breaks Z_4 translational symmetry, preserves C_4 symmetry, and does not cause orthorhombic distortion. Also, its structure factor has four equivalent peaks at $(\pm\pi/2, \pm\pi/2)$, in agreement with recent neutron scattering studies of $Fe_{1+y}Te$ [57]. An interesting issue that deserves further study is whether Z_4 translational symmetry can be broken before a true ODS spin order sets in, as it happens in other systems [77].

2.6 Technical Details for Chapter 2

Here we provide details of our analysis of which generic state is selected by quantum fluctuations in the J_1-J_2-J_3 model (Eq. 2.1) in the limit $J_1 = 0$. In this limit the even and the odd sublattices (see Fig. 2.2) are decoupled. As the analysis of interactions in even and odd sublattices is equivalent, here we only consider the even sublattice.

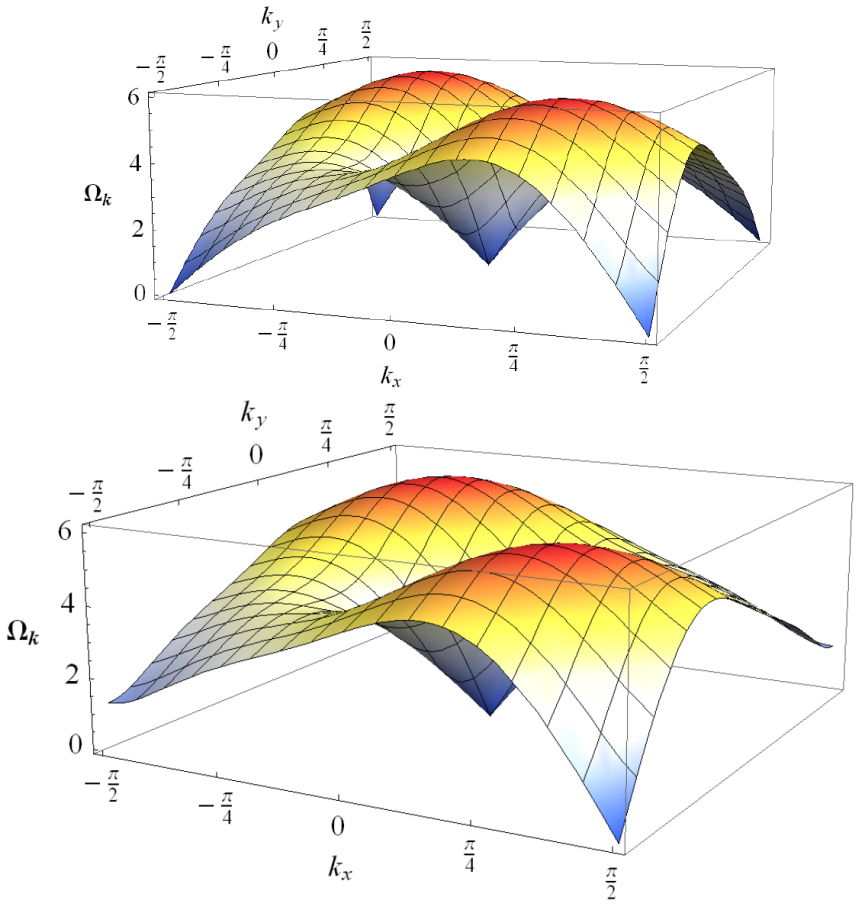

Figure 2.3: Top panel: The bare spectrum Eq. 2.15. Bottom panel: the spectrum renormalized by quantum fluctuations (1/S corrections). The bare spectrum has true Goldstone modes at $\pm\mathbf{Q_1} = \pm(\frac{\pi}{2}, -\frac{\pi}{2})$ and accidental zeroes at $\pm\mathbf{Q}_2 = \pm(\frac{\pi}{2}, \frac{\pi}{2})$ which are removed by quantum fluctuations. To make the gaps visible, we exaggerate corrections due to H_4 term.

In order to describe all possible orderings of the J_2-J_3 model, one needs to introduce the two-site basis, which in Fig. 2.2 we denote as a and b. To avoid the complexity of a two-sublattice notation it is convenient to work within a locally rotated frame of reference in which the magnetic order is ferromagnetic. For $J_3 > J_2/2$, the angle γ between spins on sites a and b is locked at $\gamma = 0$ or $\gamma = \pi$. Thus, we need to perform a uniform rotation with angle 0 or π on b-sites and with angle π on those a-sites on which spins are oppositely directed with respect to the spin at a site at the origin of the lattice. Then the excitation spectrum is described with just one magnon operator, which we introduce using the Holstein-Primakoff transformation for spins:

$$S_i^z = S - a_i^\dagger a_i$$
$$S_i^+ = (2S - a_i^\dagger a_i)^{\frac{1}{2}} a_i \;\; S_i^- = a_i^\dagger (2S - a_i^\dagger a_i)^{\frac{1}{2}},$$

where $a_i^\dagger$ and a_i are magnon creation and annihilation operators.

As we intend to study magnon interactions to first order in $1/S$, we substitute Eq. 2.10 into our Hamiltonian (Eq. 2.1) and then expand it up to the quartic order in the boson fields only and neglect higher orders terms. The Hamiltonian describing interacting bosons is then reads as

$$H = E_0 + S(H_2 + H_4) \tag{2.10}$$

where H_2 and H_4 are the quadratic and the quartic terms, respectively. Introducing Fourier transform $a_i = \sum_{\mathbf{k}} a_{\mathbf{k}}\, e^{i\mathbf{k}\cdot\mathbf{r}_i}/\sqrt{N}$, where $2N$ is the number of lattice points and the momentum $\mathbf{k}$ is defined in the first magnetic BZ, we obtain the explicit expression of the quadratic part of the $J_2 - J_3$ model in the momentum space:

$$H_2 = \;\; \sum_{\mathbf{k}} \Big(A_{\mathbf{k}} a_{\mathbf{k}}^\dagger a_{\mathbf{k}} + \tfrac{B_{\mathbf{k}}}{2} (a_{\mathbf{k}} a_{-\mathbf{k}} + h.c.) \Big) \tag{2.11}$$

where

$$\begin{aligned} A_{\mathbf{k}} &= 4J_3 + 2J_2 \cos(k_x + k_y) \\ B_{\mathbf{k}} &= -2J_3(\cos(2k_x) + \cos(2k_y)) - 2J_2 \cos(k_x - k_y) \end{aligned} \tag{2.12}$$

The quartic part of the large-S expansion is given by

$$\begin{aligned} H_4 = & \frac{J_2}{8NS}\sum_{\{\mathbf{k}_i\}}\delta\Big(\sum_i \mathbf{k}_i\Big)\Big[a^\dagger_{-\mathbf{k}_1}a_{\mathbf{k}_2}a_{\mathbf{k}_3}a_{\mathbf{k}_4}\cos(k_{4x}-k_{4y}) \\ & -a^\dagger_{-\mathbf{k}_1}a^\dagger_{-\mathbf{k}_2}a_{\mathbf{k}_3}a_{\mathbf{k}_4}\cos(k_{4x}+k_{4y}) \\ & -2a^\dagger_{-\mathbf{k}_1}a^\dagger_{-\mathbf{k}_2}a_{\mathbf{k}_3}a_{\mathbf{k}_4}\sin(k_{2x}+k_{4x})\sin(k_{2y}+k_{4y})+h.c.\Big] \\ & +\frac{J_3}{8NS}\sum_{\{\mathbf{k}_i\}}\delta\Big(\sum_i \mathbf{k}_i\Big)\Big[a^\dagger_{-\mathbf{k}_1}a_{\mathbf{k}_2}a_{\mathbf{k}_3}a_{\mathbf{k}_4}(\cos 2k_{4x}+\cos 2k_{4y}) \\ & -a^\dagger_{-\mathbf{k}_1}a^\dagger_{-\mathbf{k}_2}a_{\mathbf{k}_3}a_{\mathbf{k}_4}(\cos 2(k_{2y}+k_{4y})+\cos 2(k_{2x}+k_{4x}))+h.c.\Big] \end{aligned} \tag{2.13}$$

We first diagonalize the quadratic Hamiltonian H_2 by introducing the Bogoliubov transformation, $\alpha_{\mathbf{k}} = u_{\mathbf{k}}a_{\mathbf{k}} - v_{\mathbf{k}}a^\dagger_{-\mathbf{k}}$, where $u_{\mathbf{k}}$ and $v_{\mathbf{k}}$ and the coherence coefficients determined by

$$\begin{aligned} u_{\mathbf{k}} &= \frac{1}{2}\sqrt{\frac{A_{\mathbf{k}}+\Omega_{\mathbf{k}}}{\Omega_{\mathbf{k}}}}\,, \\ v_{\mathbf{k}} &= -\frac{\mathrm{sign}B_{\mathbf{k}}}{2}\sqrt{\frac{A_{\mathbf{k}}-\Omega_{\mathbf{k}}}{\Omega_{\mathbf{k}}}} \end{aligned}$$

and

$$\Omega_{\mathbf{k}} = S\sqrt{A^2_{\mathbf{k}}-B^2_{\mathbf{k}}}\,.$$

The diagonalized Hamiltonian H_2 is then given by

$$H_2 = E_2 + \sum_{\mathbf{k}}\Omega_{\mathbf{k}}\alpha^\dagger_{\mathbf{k}}\alpha_{\mathbf{k}} \tag{2.14}$$

where

$$E_2 = \frac{S}{2}\sum_{\mathbf{k}}(-A_{\mathbf{k}}+\Omega_{\mathbf{k}}) \tag{2.15}$$

gives $1/S$ correction to the classical ground state energy. At vectors $\mathbf{Q}_1 = (\frac{\pi}{2}, -\frac{\pi}{2})$ and $\mathbf{Q}_2 = (\frac{\pi}{2}, \frac{\pi}{2})$, $A_{\mathbf{Q}_{1(2)}} = B_{\mathbf{Q}_{1(2)}} = 4J_3 \pm 2J_2$, where the signs + and - are for the vector Q_1 and the Q_2, respectively. Thus, $\Omega_{\mathbf{Q}_1} = \Omega_{\mathbf{Q}_2} = 0$, however one can easily check that only one of them corresponds to a true Goldstone mode, while the other is an accidental zero in our spectrum. The spectrum at the accidental zeroes will be gapped by quantum

fluctuations. To find which of the two zeroes will be removed by quantum fluctuations, we calculate the 1/S corrections to the spectrum at these points.

The $1/S$ contribution from the quartic Hamiltonian can be obtained through a mean-field decoupling of H_4. We first define the averages

$$\begin{aligned} K_{\mathbf{q}} &= \langle a^\dagger_{\mathbf{q}} a_{\mathbf{q}} \rangle = v^2_{\mathbf{q}} \\ L_{\mathbf{q}} &= \langle a_{\mathbf{q}} a_{-\mathbf{q}} \rangle = \langle a^\dagger_{-\mathbf{q}} a^\dagger_{\mathbf{q}} \rangle = u_{\mathbf{q}} v_{\mathbf{q}} \ . \end{aligned} \tag{2.16}$$

Then in the mean-field the H_4 term reads as

$$\begin{aligned} \bar{H}_4 &= \frac{1}{8NS} \sum_{\mathbf{k},q} \Big(a^\dagger_{\mathbf{k}} a_{\mathbf{k}} F_1(\mathbf{k},\mathbf{q}) + \\ &\qquad (a_{\mathbf{k}} a_{-\mathbf{k}} + a^\dagger_{-\mathbf{k}} a^\dagger_{\mathbf{k}}) \frac{F_2(\mathbf{k},\mathbf{q})}{2} \Big) \end{aligned} \tag{2.17}$$

where

$$\begin{aligned} &F_1(\mathbf{k},\mathbf{q}) = -2J_3 \Big(4K_{\mathbf{q}} (\cos^2(k_x - q_x) + \cos^2(k_y - q_y)) \\ &-L_{\mathbf{q}} (2(\cos 2q_x + \cos 2q_y) + \cos 2k_x + \cos 2k_y) \Big) \\ &-2J_2 \Big(K_{\mathbf{q}} (4 \sin(k_x - q_x) \sin(k_y - q_y) \\ &+2\cos(k_x + k_y) + 2\cos(q_x + q_y)) \\ &-L_{\mathbf{q}} (2\cos(q_x - q_y) + \cos(k_x - k_y)) \Big), \\ &F_2(\mathbf{k},\mathbf{q}) = 2J_3 \Big(K_{\mathbf{q}} (\cos 2q_x + \cos 2q_y \\ &+2(\cos 2k_x + \cos 2k_y)) \\ &-2L_{\mathbf{q}} (\cos 2(k_x - q_x) + \cos 2(k_y - q_y)) \Big) \\ &+2J_2 \Big(K_{\mathbf{q}} (\cos(q_x - q_y) + 2\cos(k_x - k_y)) \\ &+L_{\mathbf{q}} (-4 \sin(k_x - q_x) \sin(k_y - q_y) \\ &- \cos(k_x + k_y) - \cos(q_x + q_y)) \Big) \end{aligned}$$

The quadratic Hamiltonian plus the decoupled H_4 can be expressed as:

$$\begin{aligned} H_2 + \bar{H}_4 = \sum_{\mathbf{k}} \Big[&(A_{\mathbf{k}} + \frac{A^{(4)}_{\mathbf{k}}}{S}) a^\dagger_{\mathbf{k}} a_{\mathbf{k}} + \\ &\frac{1}{2} (B_{\mathbf{k}} + \frac{B^{(4)}_{\mathbf{k}}}{S}) (a_{\mathbf{k}} a_{-\mathbf{k}} + h.c.) \Big] \end{aligned} \tag{2.18}$$

where

$$\begin{aligned} A^{(4)}_{\mathbf{k}} &= \frac{1}{8N}\sum_{\mathbf{q}} F_1(\mathbf{k},\mathbf{q}), \\ B^{(4)}_{\mathbf{k}} &= \frac{1}{8N}\sum_{\mathbf{q}} F_2(\mathbf{k},\mathbf{q}) \end{aligned}$$

Next we compute $A^{(4)}_{\mathbf{k}}$ and $B^{(4)}_{\mathbf{k}}$ at Q_1 and Q_2:

$$\begin{aligned} A^{(4)}_{\mathbf{Q_{1(2)}}} &= \frac{-1}{4N}\sum_{\mathbf{q}} J_3\Big(4K_{\mathbf{q}}(\sin^2(q_x)+\sin^2(q_y)) \\ &\quad -L_{\mathbf{q}}(2(\cos 2q_x+\cos 2q_y)-2)\Big) \\ &\quad +J_2\Big(K_{\mathbf{q}}(\mp 4\cos(q_x)\cos(q_y) \\ &\quad \pm 2+2\cos(q_x+q_y)) \\ &\quad -L_{\mathbf{q}}(2\cos(q_x-q_y)\mp 2)\Big), \\ B^{(4)}_{\mathbf{Q_{1(2)}}} &= \frac{1}{4N}\sum_{\mathbf{q}} J_3\Big(K_{\mathbf{q}}(\cos 2q_x+\cos 2q_y-4) \\ &\quad +2L_{\mathbf{q}}(\cos 2q_x+\cos 2q_y)\Big) \\ &\quad +J_2\Big(K_{\mathbf{q}}(\cos(q_x-q_y)\mp 2) \\ &\quad +L_{\mathbf{q}}(\pm 4\cos(q_x)\cos(q_y) \\ &\quad \mp 1-\cos(q_x+q_y))\Big)\ , \end{aligned} \tag{2.19}$$

where the upper and the lower signs correspond to $\mathbf{Q_1}$ and $\mathbf{Q_2}$ vectors, respectively. It can be shown that $A^{(4)}_{\mathbf{Q_1}} = B^{(4)}_{\mathbf{Q_1}}$, but $A^{(4)}_{\mathbf{Q_2}} \neq B^{(4)}_{\mathbf{Q_2}}$. Thus, when 1/S corrections are included the spectrum at $\mathbf{Q_1}$ remains gappless, $\Omega_{\mathbf{Q_1}} = 0$, and is a true Goldstone mode, while the gap opens at $\mathbf{Q_2}$ and $\Omega_{\mathbf{Q_2}} \neq 0$, clearly indicating that $\mathbf{Q_2}$ point was an accidental zero at the linear spin wave spectrum. This can be clearly seen in Fig. 2.3, where we plot linear spin wave spectrum (top panel) and spectrum renormalized to 1/S order (bottom panel).

Chapter 3

Theory of the Evolution of Magnetic Order in Fe_{1+y} Te Compounds with Increasing Interstitial Iron

3.1 Introduction

$Fe_{1+y}Te$ chalcogenides are the parent compounds of the simplest family of iron-based superconductors [25, 56, 58, 60, 78, 79, 80, 81, 82, 83, 84, 85, 86]. Both electronic and magnetic properties in $Fe_{1+y}Te$ compounds show strong sensitivity to the amount of non-stoichiometric Fe ions. At small values of y, the low temperature crystal structure is monoclinic ($P21/m$) and the magnetic order is described by the commensurate propagation vector $\mathbf{Q} = (\pm\pi/2, \pm\pi/2)$. This is remarkably different from FeAs-based systems, in which parent compounds have the antiferromagnetic order described by $\mathbf{Q} = (\pi, 0)$ or $\mathbf{Q} = (0, \pi)$ and the crystal structure has orthorhombic symmetry (Pmmn). With an increasing amount of interstitial Fe, the magnetic structure in $Fe_{1+y}Te$ turns into an incommensurate spiral. The incommensurate ordering manifests itself as a shifted elastic scattering peak with respect to the $\mathbf{Q} = (\pm\pi/2, \pm\pi/2)$ positions. According to neutron scattering experiments [58, 78, 79, 80, 85, 86], in the range of $0.11 < y < 0.16$

the shift is approximately along the diagonal direction $\mathbf{Q} = (\pi/2 - \delta, \pi/2 - \delta)$ or $\mathbf{Q} = (-\pi/2 + \delta, \pi/2 - \delta)$; however, δ does not vary smoothly with y.

There were several theoretical attempts to understand magnetic properties of $Fe_{1+y}Te$ compounds within the localized spin scenario [27, 28, 63, 87, 88]. Although magnetic order both at low and at high levels of Fe excess can be successfully described by a $J_1 - J_2 - J_3$ super-exchange model, it is clear that the local picture by itself can not describe the magnetic properties of $Fe_{1+y}Te$, as this requires y-dependent exchange couplings.

We argue that the evolution of magnetic interactions due to y-dependent charge doping is the key to understand the experimentally observed magnetic phase diagram of $Fe_{1+y}Te$. Our study is based on the assumption that some of the orbital states are almost localized while other states still participate in the conductivity. This idea is supported by recent dynamical mean-field theory study of Fe chalcogenides [31, 89]. These studies showed that due to the strong Hund's coupling, an orbital-selective localization might be happening already in the paramagnetic phase, which justifies a partial localization.

In this work we demonstrate that the change in magnetic properties observed in $Fe_{1+y}Te$ compounds can be reasonably well captured by an effective model in which localized spins, in addition to the Heisenberg super-exchange [27] and phonon-mediated biquadratic couplings [90, 91], acquire a long-range RKKY-like interaction [92, 93]. The latter, mediated by a multiorbital spin susceptibility of itinerant electrons doped into the system from interstitial Fe, is the interaction responsible for the evolution of magnetic order with increasing level of Fe excess.

The outline of our paper is as follows. In section 3.2, we present an effective superexchange model describing localized magnetic moments in the multi-band correlated electron sea and argue that this is the minimal microscopic model to describe the magnetism of $Fe_{1+y}Te$ compounds. In section 3.3, we study the evolution of the Fermi surface of $FeTe_{1+y}$ with increasing level of the Fe excess using a tight-binding model by Wang *et al* [94]. We show that while the Fermi surface at small y has both small hole pockets at the Γ- and M-points and elliptical electron pockets at the X- and Y-points, at large y all pockets are electron-like. In section 3.4, we study spin fluctuations in the correlated multi-band electron system and compute the Pauli susceptibility within the random phase approximation (RPA) approach. We find that at small y itinerant

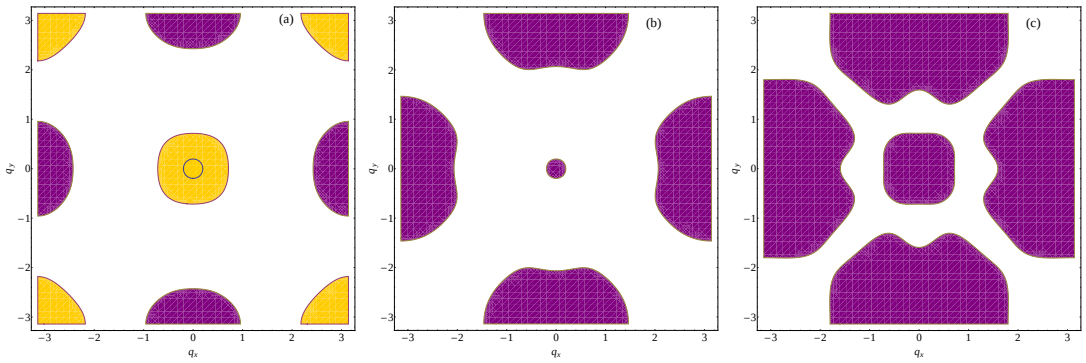

Figure 3.1: Fermi surfaces obtained for shifted chemical potential μ: (a) $\mu = 0$ eV, (b) $\mu = 0.4$ eV, (c) $\mu = 0.8$ eV. The hole and the electron pockets are shown by yellow and purple color, correspondingly. The primary contribution to the electron pockets is from the xz and yz orbitals. The primary contribution to the hole pocket is from the xy orbital. We assume the rigid band structure approximation.

spin susceptibility peaks at $(\pi, 0)$ and $(0, \pi)$ due to the weak nesting of the hole and the electron pockets corresponding to these vectors. The y-dependent charge doping suppresses the $(\pi, 0)$ and $(0, \pi)$ peaks, but it leads to an increase of the spin fluctuation in the central part of the Brillouin zone. In section 3.5, we compute the RKKY interactions. We first perform a qualitative computation of the RKKY interactions using a simple phenomenological model, and then perform a quantitative analysis based on the realistic RPA susceptibility obtained in section IV. In section 3.6, the classical phase diagram of the effective spin model is presented. In agreement with experimental findings, the computed phase diagram displays a transition from a commensurate double stripe phase, characterized by a wave vector $\mathbf{Q} = (\pi/2, \pm\pi/2)$ or $\mathbf{Q} = (\pm\pi/2, \pi/2)$, to an incommensurate spiral (IC) phase characterized by wave vectors $\mathbf{Q} = (q, q)$, above certain level of Fe excess. We conclude with a summary in section 3.7. This chapter also contains technical details in section 3.8. This contains contains the derivation of the biquadratic exchange from the magnetoelastic coupling, and also provides the explicit expression of the classical energy of the effective superexchange model describing $FeTe_{1+y}$.

3.2 Model

We start by assuming that in $Fe_{1+y}Te$ the correlation effects within the multiband structure lead to different levels of itineracy for the electrons occupying different orbitals [31, 89]. According to these studies, the most localized orbitals among the five $3d$ orbitals of Fe ions are the x^2-y^2 and $3z^2-r^2$ orbitals. This finding is also supported by several ab-initio calculations [94, 95], which show that x^2-y^2 and $3z^2-r^2$ orbitals have only a small overlap with the $4p$ orbitals of Te and are thus expected to remain less extended with stronger interaction potentials.

Here, we assume that the electrons occupying x^2-y^2 and $3z^2-r^2$ orbitals are localized, and they form local moments with $S=1$ due to the Hund's coupling. This assumption is in agreement with the ordered moment observed at low temperatures. The remaining $3d$ electrons have itinerant character. The number of itinerant electrons grows as y increases. In most of the paper, following the work of Singh [96], we assume that each excess Fe atom contributes 8 electrons. In the rigid band approximation, the doping of excess electrons shifts the chemical potential from $\mu=0$ to positive values.

The microscopic Hamiltonian describing the magnetism in $Fe_{1+y}Te$ is an effective double exchange model describing localized magnetic moments in the multi-band correlated electron sea, which can be written as

$$H = H_e + H_{\mathbf{S}} + H_{\sigma\mathbf{S}} \ . \tag{3.1}$$

The first term describes strongly interacting itinerant electrons:

$$H_e = H_0 + H_{int}. \tag{3.2}$$

The non-interacting part is based on the five-orbital tight-binding model of Wang *et al* [94]:

$$H_0 = \sum_{\mathbf{k},a,b,\sigma} \left(t^{ab}_{\mathbf{k}\sigma} c^{\dagger}_{\mathbf{k}a\sigma} c_{\mathbf{k}b\sigma} + h.c. \right) \ , \tag{3.3}$$

where $c^{\dagger}_{\mathbf{k}\sigma a}$ denotes the creation operator for an electron of momentum $\mathbf{k}$ with spin σ in the orbital a, and $t^{ab}_{\mathbf{k}\sigma}$ are the tight-binding matrix elements. The interaction part is

the three-orbital Hubbard model

$$H_{int} = \frac{1}{2}\sum_{i,ab\sigma\sigma'}(U_{ab}c^{\dagger}_{ia\sigma}c_{ia\sigma}c^{\dagger}_{ib\sigma'}c_{ib\sigma'} + J_{ab}c^{\dagger}_{ia\sigma}c_{ib\sigma'}c^{\dagger}_{ia\sigma'}c_{ib\sigma}), \tag{3.4}$$

where U_{ab} and J_{ab} denote the effective Coulomb and Hund's interaction constants. In this work we consider all diagonal Coulomb interactions elements equal to U, off-diagonal Coulomb interactions equal to $U - 2J_H$ and all $J_{ab} = J_H$, where J_H is the Hund's coupling. It is important that this choice of interaction parameters implies invariance of the interaction Hamiltonian under rotations in orbital space.

The second term in Eq. 3.1 describes the interaction between localized spins:

$$H_{\mathbf{S}} = \sum_{<ij>}\left(J_{ij}\mathbf{S}_i \cdot \mathbf{S}_j - \frac{K_{ij}}{S^2}(\mathbf{S}_i \cdot \mathbf{S}_j)^2\right), \tag{3.5}$$

where J_1, J_2, and J_3 are super-exchange couplings between first-, second-, and third-nearest neighbors. In this work, we obtain values of J_1, J_2, and J_3 from the first-principles electronic structure calculations [27] by subtracting the contributions to the couplings determined by itinerant electrons. We assume that the biquadratic exchange is likely caused by magnetoelastic couplings, and under this assumption, we derive its explicit form in the section 3.8.

The third term

$$H_{\sigma\mathbf{S}} = J_H \sum_{j,a}\sigma_{ja} \cdot \mathbf{S}_j \tag{3.6}$$

describes the coupling between the spins of localized electrons, $\mathbf{S}_j$, and itinerant electrons σ_{ja}. Here $\mathbf{S}_j$ are the localized spins of electrons on orbitals $x^2 - y^2$ and $3z^2 - r^2$, and σ_{ja} are the spins of itinerant electrons on orbitals $a = xy, yz, xz$ defined as

$$\sigma_{ja} = \frac{1}{N}\sum_{\mathbf{k},\mathbf{k}',\sigma,\sigma'} e^{i(\mathbf{k}'-\mathbf{k})\mathbf{R_j}}c^{\dagger}_{\mathbf{k}a\sigma}\tau_{\sigma\sigma'}c_{\mathbf{k}'a\sigma'}\ , \tag{3.7}$$

where $\tau_{\sigma\sigma'}$ is the Pauli matrix. According to the Hund's rule, since we are dealing with more than half-filled t_{2g} shell, the coupling between local spins and spins of itinerant electrons is antiferromagnetic, $J_H > 0$.

Eq. 3.6 is the dubbed double exchange interaction widely observed in the context of manganites. This interaction lead to additional couplings between localized moments:

$$H_{\mathrm{RKKY}} = \sum_{<ij>} J_{ij}^{\mathrm{RKKY}} \mathbf{S}_i \mathbf{S}_j. \tag{3.8}$$

The couplings J_{ij}^{RKKY}, dubbed RKKY interactions, between localized spins on lattice sites $\mathbf{R}_i$ and $\mathbf{R}_j$ can be obtained by integrating out itinerant degrees of freedom and computing their effect on localized spins. It is easy to show that J_{ij}^{RKKY} are determined by the tensor of static spin susceptibility $\chi(\mathbf{q}, \omega = 0) = \chi(\mathbf{q})$ of the multi-band conduction electron sea:

$$\begin{aligned} J_{ij}^{\mathrm{RKKY}} = & - J_H^2 \chi(\mathbf{R}_i - \mathbf{R}_j) = \\ & - J_H^2 \sum_{\mathbf{q}} e^{\imath(\mathbf{R}_i - \mathbf{R}_j)\mathbf{q}} \chi(\mathbf{q}). \end{aligned} \tag{3.9}$$

Taking into account both Heisenberg and RKKY interactions, the effective low-energy Hamiltonian can be written as

$$H_{\mathrm{eff}} = \sum_{<ij>} J_{ij}^{\mathrm{eff}} \mathbf{S}_i \mathbf{S}_j - \sum_{<ij>} \frac{K_{ij}}{S^2} (\mathbf{S}_i \cdot \mathbf{S}_j)^2, \tag{3.10}$$

where, for convenience, we defined $J_{ij}^{\mathrm{eff}} = J_{ij} + J_{ij}^{\mathrm{RKKY}}$.

3.3 Fermi Surface Evolution

We start with briefly observing how the Fermi surface of $Fe_{1+y}Te$ evolves with increasing amount of the interstitial Fe. In Fig. 3.1(a), we show the Fermi surface of FeTe ($y = 0$) obtained from the five-orbital tight-binding model by Wang *et al* [94]. The Fermi surface is characterized by the elliptical electron pockets at the $X = (\pi, 0)$ and $Y = (0, \pi)$ points and circular hole pockets centered at the $\Gamma = (0, 0)$ and $M = (\pi, \pi)$ points. We see that there is a weak nesting between electron and hole pockets with the wave vectors $(\pi, 0)$ and $(0, \pi)$. However, there is no Fermi surface nesting instability associated with the magnetic order vector $(\pm\pi/2, \pi/2)$, which would explain magnetic order from purely itinerant model. This observation is in agreement with the angle-resolved photoemission (ARPES) study of the topology of the Fermi surface [60], which also did not observe any nesting corresponding to the magnetic ordering vector.

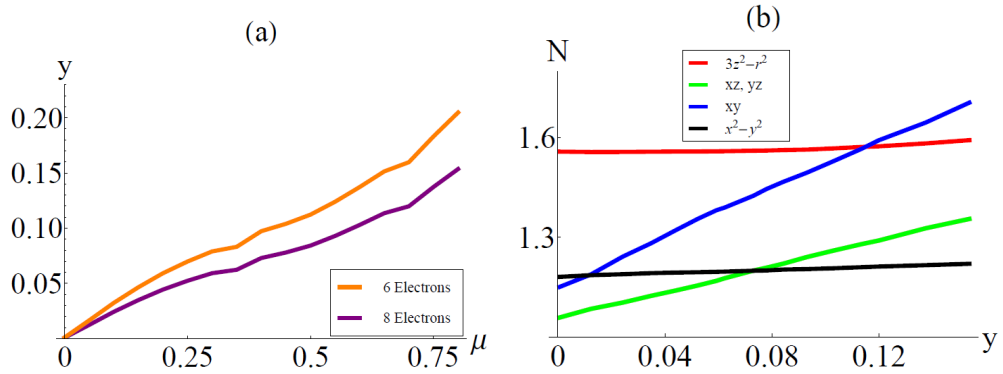

Figure 3.2: (a) The dependence of the shift of the chemical potential μ on the amount of excess iron when each excess iron provides 6 electrons per atom (orange) and 8 electrons per atom (purple). (b) The orbitally resolved electron occupation numbers N as functions of y. The occupation of $3z^2-r^2$, xz, yz, xy, and x^2-y^2 orbitals are shown by red, green, brown, blue, and black lines, respectively. The xz and yz orbitals have the same electron occupation numbers due to the symmetries of the system.

When the level of interstitial Fe increases, the chemical potential shifts up, and the geometry of the Fermi surface changes significantly. In Fig. 3.1(b) and (c) we plot constant energy cuts which correspond to the shifting of the chemical potential to (b) μ =0.4 eV, and (c) μ =0.8 eV in the rigid band approximation. The nesting between electron and hole pockets disappears very quickly as the sizes of the hole and electron pockets changes significantly with the shift of the chemical potential μ. Initially, while the size of the electron pockets is enlarged, the size of the hole pockets is reduced. The hole pockets disappear at $\mu = 0.23$ eV. Then, at bigger shifts of μ (or at larger y), the pockets at the Γ and M points change their character and become electron-like at $\mu = 0.3$ eV.

In order to relate the shift of the chemical potential μ to the amount of excess iron y, in Fig. 3.2(a) we plot the dependence of μ on y for two cases: each interstitial Fe adding 8 (purple line) and 6 (orange line) electrons. We see that the shift of 0.4 eV (Fig. 3.1(b)) corresponds to $y = 0.07$ and $y = 0.09$, if we consider each interstitial Fe adds 8 and 6 electrons, respectively, and the shift of 0.8 eV (Fig. 3.1(c)) corresponds to $y = 0.15$ and $y = 0.20$, respectively, for 8 and 6 electrons. In the following, all results

are computed assuming each interstitial iron adds 8 electrons into the band.

In Fig. 3.2(b) we show how electron occupation numbers for different orbitals depend on the level of Fe excess, y. We see that the occupation of xz, yz and xy orbitals changes significantly, indicating that the charge doping due to the Fe excess goes predominantly on these orbitals. The occupation of xz and yz barely changes with an increase of y, which is consistent with the fact that these orbitals have mostly localized character. Notice, that due to tetragonal symmetry, the occupation numbers of xz and yz orbitals are exactly the same and the corresponding lines completely overlap.

3.4 Spin Susceptibility of Itinerant Electrons

Next let us discuss in detail the form of the multi-orbital spin susceptibility $\chi(\mathbf{q},\omega)$. Here we use the formalism which was originally developed for the five orbital model for the Fe-pnictides in Ref. [97] and later extensively studied for various orbital models in Ref. [98]. We compute $\chi(\mathbf{q},\omega)$ in the random phase approximation (RPA) using the tight-binding model by Wang *et al* [94].

In the paramagnetic state, the spin-rotation invariance requires that transverse and longitudinal components of the spin susceptibility are identical. Thus, we can express $\chi(\mathbf{q},\omega)$ only in terms of components of the transverse susceptibility: $\chi(\mathbf{q},\omega) = \frac{3}{2}\chi^{+-}(\mathbf{q},\omega)$. We note that as we are dealing with multi-orbital systems, the spin susceptibility is a four-index tensor, while the total susceptibility is a sum over all components of this tensor.

3.4.1 Bare Susceptibility

In the multi-orbital model under consideration, the matrix elements of the bare spin susceptibility can be calculated from the corresponding Matsubara spin-spin correlation function of conduction electrons:

$$\chi^0_{aa'bb'}(\mathbf{q},\imath\omega) = \\ -\frac{T}{N}\sum_{\mathbf{k},\imath\omega_n} G_{ab}(\mathbf{k},\imath\omega_n)G_{a'b'}(\mathbf{k}+\mathbf{q},\imath\omega_n+\imath\omega) \tag{3.11}$$

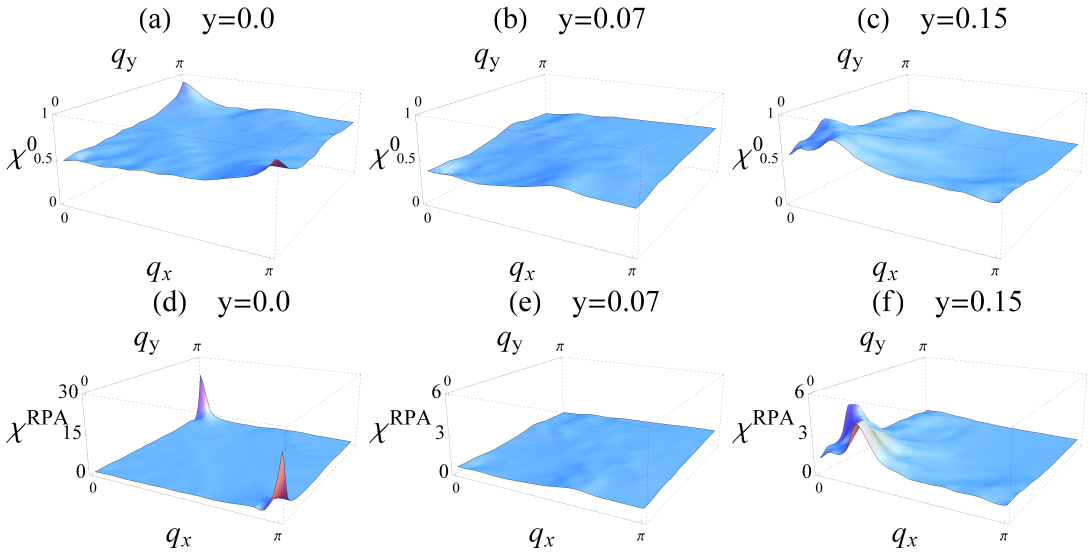

Figure 3.3: (a)-(c) The bare static spin susceptibility $\chi^0(\mathbf{q}, 0)$ and (d)-(f) the RPA spin susceptibility $\chi(\mathbf{q}, 0)$ calculated with the ab-initio bands of tight-binding model [94] after projecting out $x^2 - y^2$ and $3z^2 - r^2$ orbitals. The level of Fe excess is (a) and (d) $y = 0.0$; (b) and (e) $y = 0.07$; (c) and (f) $y = 0.15$. The RPA spin susceptibility is calculated at $U = 1.0$ eV and $J = U/5$.

where a, a', b, b' are orbital indices, and the spectral representation of the multiorbital Green's function is given by

$$G_{ab}(\mathbf{k}, \imath\omega_n) = \sum_{\nu} \frac{u^a_\nu(\mathbf{k})(u^b_\nu(\mathbf{k}))^*}{\imath\omega_n - E_\nu(\mathbf{k})} \ . \tag{3.12}$$

Here, the coefficients $u^a_\nu(\mathbf{k})$ are the components of the eigenvectors resulting from the diagonalization of the five-orbital tight-binding Hamiltonian [94], and $E_\nu(\mathbf{k})$ are the eigenvalues describing resulting bands characterized by the band index ν. The retarded bare susceptibility is then obtained by summing over the Matsubara frequency and setting $\imath\omega \to \omega + \imath\delta$:

$$\begin{aligned} \chi^0_{aa'bb'}(\mathbf{q}, \omega) \quad &= \quad -\frac{1}{N} \sum_{\mathbf{k},\nu,\nu'} \frac{u^a_{\nu\mathbf{k}}(u^b_{\nu\mathbf{k}})^* u^{b'}_{\nu'(\mathbf{k}+\mathbf{q})}(u^{a'}_{\nu'(\mathbf{k}+\mathbf{q})})^*}{E_{\nu'}(\mathbf{k}+\mathbf{q}) - E_\nu(\mathbf{k})} \\ &\quad \times (f(E_{\nu'}(\mathbf{k}+\mathbf{q})) - f(E_\nu(\mathbf{k}))) \ , \end{aligned} \tag{3.13}$$

where

$$f(E_\nu(\mathbf{k})) = \frac{1}{e^{\frac{E_\nu(\mathbf{k})-\mu}{T}} + 1}$$

denotes the Fermi distribution function.

In Fig. 3.3(a)-(c) we show results for the total static spin susceptibility $\chi(\mathbf{q},0) = \frac{1}{2}\chi_{aabb}(\mathbf{q},0)$ with the x^2-y^2 and $3z^2-r^2$ orbitals being projected out by setting all components of the eigenvectors $u_\nu^{x^2-y^2}(\mathbf{k})$ and $u_\nu^{3z^2-r^2}(\mathbf{k})$ equal to zero. The bare susceptibility $\chi^0(\mathbf{q})$ is overall rather flat with small peaks at $(0,\pi)$ and $(\pi,0)$ at $y=0$ (Fig. 3.3(a)), almost featureless shape at $y=0.07$ (Fig. 3.3(b)) and a wide region of enhanced fluctuations in the vicinity of Γ point at $y=0.15$ (Fig. 3.3(c)). All these features are well seen in Fig. 3.4(a), where we plot the bare spin susceptibilities for different values of y along the symmetry path $\Gamma=(0,0) \rightarrow X=(\pi,0) \rightarrow M=(\pi,\pi) \rightarrow \Gamma=(0,0)$. Red, green and blue lines correspond to $y=0.0$, $y=0.07$ and $y=0.15$, respectively. As in Fig. 3.3(a)-(c) we see that at $y=0.0$ the bare susceptibility shows enhanced fluctuations peaked at the $X=(\pi,0)$ point, at $y=0.15$ the weight of spin fluctuations is shifted to the vicinity of $\Gamma=(0,0)$ point, while for the intermediate values of y the bare susceptibility is basically featureless.

3.4.2 RPA Susceptibility

The effect of correlations among itinerant electrons on the spin susceptibility can be taken into account in the framework of the RPA. The RPA spin susceptibility can be obtained using the Dyson equation:

$$\begin{aligned} \chi^{\rm RPA}_{aa'bb'}(\mathbf{q},\omega) &= \chi^0_{aa'bb'}(\mathbf{q},\omega) + \\ &\quad \chi^0_{aa'cc'}(\mathbf{q},\omega)\, V_{cc'dd'}\, \chi_{dd'bb'}(\mathbf{q},\omega)\ , \end{aligned} \tag{3.14}$$

where the matrix elements $V_{cc'dd'}$ take into account all electron correlations in the RPA. The interaction parameters which give the strongest contributions are those from the matrix elements $V_{cccc}=U$, $V_{ccdd}=J_H$, $V_{cddc}=J_H$, and $V_{cdcd}=U-2J_H$. All other matrix elements are set to 0.

In Fig. 3.3(d)-(f) we present the static RPA spin susceptibility for different values of y. We see that $\chi^{\rm RPA}(\mathbf{q},0)$ shows significant enhancement due to interactions notice that different scales have been used in Fig. 3.3(a)-(c), Fig. 3.3(d), and Fig. 3.3(e)(f). In our calculations we have chosen $U=1.0$ eV and $J_H=U/5$. Both the Coulomb repulsion and the Hund's coupling are well inside the range of the interaction parameters previously considered in the literature: the lowest estimate of $J_H/U=0.15$ was used in Ref. [31]

and the upper limit of $J_H/U = 0.25$ was considered in several works, e.g. in Refs.[98, 99]. Selecting J_H inside this range ensures that an electron added to an undoped site pays more energy to Coulomb repulsion than it wins from the Hund's rule, i.e. that the onsite interaction energy suppresses charge fluctuations rather than enhancing them.[98]

In Fig. 3.3(d), the RPA susceptibility computed at $y = 0.0$. The small peaks at the wave vectors $(\pm\pi, 0)$ and $(0, \pm\pi)$ vectors observed in the bare susceptibility now show almost diverging behavior. Similarly to the bare susceptibility, $\chi^{\mathrm{RPA}}(\mathbf{q}, 0)$ at $y = 0.0$ also does not indicate any significant spin fluctuations near $(\pm\pi/2, \pi/2)$ and $(\pi/2, \pm\pi/2)$ points corresponding to the vectors of the experimentally observed magnetic order.

With increasing y (see Fig. 3.3(e) and Fig. 3.3(f)), we observe significant changes in the overall structure of the spin susceptibility. As it is particularly seen in Fig. 3.4(b), where we show the RPA spin susceptibility along the main symmetry directions, the susceptibility near $(\pm\pi, 0)$ and $(0, \pm\pi)$ rapidly decreases with increasing y and the dominant magnetic response shifts to the Γ point and its vicinity. At $y = 0.07$ (Fig. 3.3(e)), the susceptibility is of almost uniform height in the whole Brillouin zone. At higher values of y (see Fig. 3.3(f)), the susceptibility shows dominant but not diverging behavior in the central part of Brillouin zone close to the Γ point.

3.5 The RKKY Exchange Integrals

Eq. 3.9 shows that the RKKY exchange integrals J_{ij}^{RKKY} are proportional to the static magnetic susceptibility of multi-orbital conduction electrons. Thus, the changes in the spin susceptibility with the level of the interstitial Fe discussed in the previous section will lead to the corresponding changes of J_{ij}^{RKKY}.

3.5.1 Toy Model for the RKKY Interaction

Let us first understand these changes in the framework of a simple toy model with the following phenomenological expression for the static magnetic susceptibility:

$$\chi^{-1}(\mathbf{q}) = \frac{1 + \alpha\left[\cos k_x \cos k_y - \frac{1}{8}\left(\cos 2k_x + \cos 2k_y\right)\right]}{\chi_0\left(1 + \frac{3}{4}\alpha\right)} \tag{3.15}$$

Here χ_0 sets the overall scale and $\alpha < 1$ is a parameter that controls the height and width of the peaks at $(\pi, 0) / (0, \pi)$ without changing the overall amplitude of the magnetic

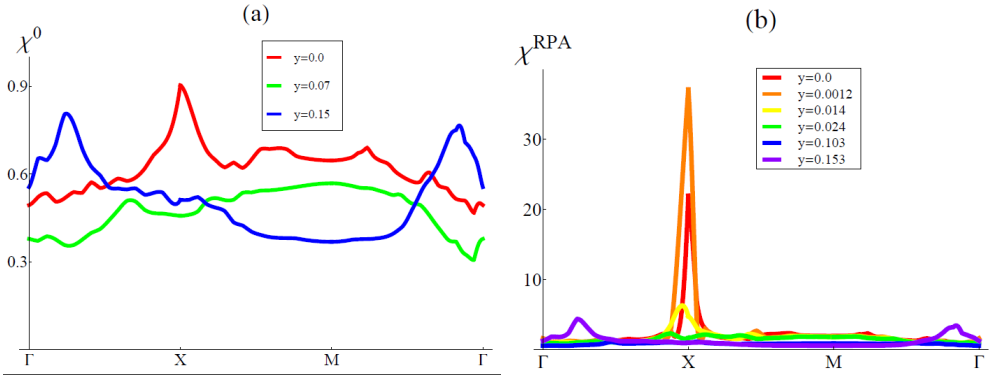

Figure 3.4: (a) The cut of the bare spin susceptibility along the main symmetry direction. Red, green and blue lines correspond to $y = 0.0$, $y = 0.07$ and $y = 0.15$, respectively. (b) The cut of the RPA enhanced spin susceptibility along the main symmetry direction. The legend provides the y values of each line. We use the following notations: $\Gamma = (0,0)$, $X = (\pi,0)$ and $M = (\pi,\pi)$. The RPA spin susceptibility is calculated for $U = 1.0$ eV and $J = U/5$.

susceptibility. In Fig. 3.5(a) we plot this phenomenological static magnetic susceptibility $\chi(q_x,0)$ for $\alpha = 0.2$ (magenta) and $\alpha = 0.6$ (blue). We see that the peak at $(\pi,0)$ decreases with decreasing α. Thus, decreasing α mimics the effect of the increasing y which leads to the suppression of the peaks at $(\pi,0)\,/\,(0,\pi)$ observed in the RPA magnetic susceptibility at $y = 0.0$.

Next we compute the RKKY interactions as a function of α. Taking the Fourier transforms, we obtain:

$$J_1^{\mathrm{RKKY}} = -J_H^2 \sum_{\mathbf{q}} \chi(\mathbf{q}) (\cos q_x + \cos q_y) \tag{3.16}$$

$$J_2^{\mathrm{RKKY}} = -J_H^2 \sum_{\mathbf{q}} \chi(\mathbf{q}) \cos q_x \cos q_y \tag{3.17}$$

$$J_3^{\mathrm{RKKY}} = -J_H^2 \sum_{\mathbf{q}} \chi(\mathbf{q}) (\cos 2q_x + \cos 2q_y) \tag{3.18}$$

Numerical evaluation gives the results shown in Fig. 3.5(b). $J_1^{\mathrm{RKKY}} \approx 0$ for nearly all values of α. The qualitative behaviors of J_2^{RKKY} and J_3^{RKKY} are the following: First, $J_2^{\mathrm{RKKY}} > 0$ and $J_3^{\mathrm{RKKY}} < 0$, with $J_2^{\mathrm{RKKY}} \approx \left|J_3^{\mathrm{RKKY}}\right|$. Second, as the peak intensity decreases (i.e. as α decreases), the absolute values of J_2^{RKKY} and J_3^{RKKY} decreases

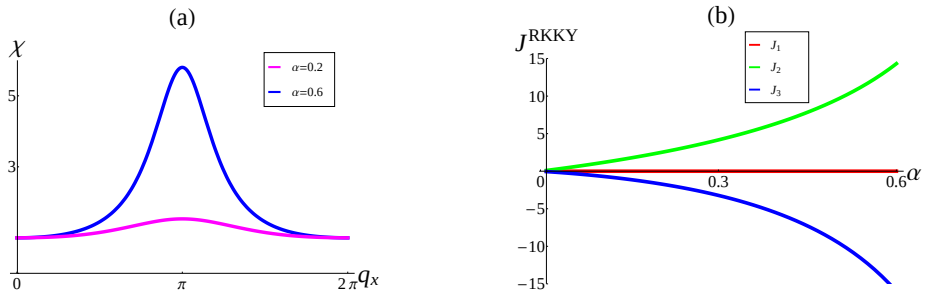

Figure 3.5: (a) Static magnetic susceptibility $\chi(q_x, 0)$ of the toy model 3.15 for $\alpha = 0.2$ (magenta) and $\alpha = 0.6$ (blue). (b) J^{RKKY} (in units of $J_H^2\chi_0$) of the same toy model as function of the $(\pi, 0)\,/\,(0, \pi)$ peak intensity α. J_1^{RKKY}, J_2^{RKKY} and J_3^{RKKY} are shown by red, green, and blue lines, respectively.

strongly.

This outcome can be understood from a simple reasoning. Let us further simplify our toy model and write, for the susceptibility, a background plus peaks at $\mathbf{Q}_X = (\pi, 0)$ and $\mathbf{Q}_Y = (0, \pi)$:

$$\frac{\chi(\mathbf{q})}{\chi_0} = 1 + \alpha\left[\delta(\mathbf{q} - \mathbf{Q}_X) + \delta(\mathbf{q} - \mathbf{Q}_Y)\right] \tag{3.19}$$

A straightforward calculation gives:

$$J_1^{\mathrm{RKKY}}/(J_H^2\chi_0) = -2\alpha(\cos\pi + \cos 0) = 0 \tag{3.20}$$

$$J_2^{\mathrm{RKKY}}/(J_H^2\chi_0) = -2\alpha(\cos\pi\cos 0) = 4\alpha \tag{3.21}$$

$$J_3^{\mathrm{RKKY}}/(J_H^2\chi_0) = -2\alpha(\cos 2\pi + \cos 0) = -4\alpha \tag{3.22}$$

This shows that peaks at $(\pi, 0)$ and $(\pi, 0)$ control only the interactions between second and third neighbors without affecting the nearest neighbor interaction. The later is, however, very sensitive to the fluctuations peaked at different wave vectors, as we will see in more realistic calculations in the next subsection, in particular to the fluctuations with small Q vectors.

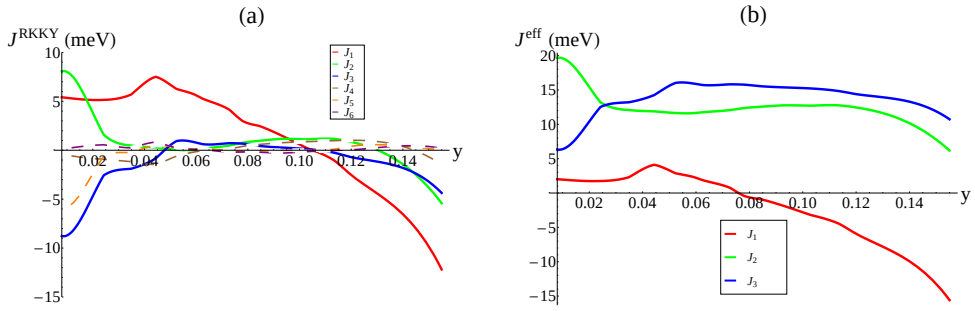

Figure 3.6: (a) The evolution of J_1^{RKKY} (red solid line), J_2^{RKKY} (green solid line), J_3^{RKKY} (blue solid line) with increasing excess of interstitial Fe atoms y. The further neighbor interactions are J_4^{RKKY} (brown dashed line), J_5^{RKKY} (orange dashed line), J_6^{RKKY} (purple dashed line). (b) The evolution of effective couplings J_{ij}^{eff}, where $J_1^{\mathrm{eff}} = -3.4 + J_1^{\mathrm{RKKY}}(y)$ (red line), $J_2^{\mathrm{eff}} = 11.6 + J_2^{\mathrm{RKKY}}(y)$ (green line), and $J_3^{\mathrm{eff}} = 15.1 + J_3^{\mathrm{RKKY}}(y)$ (blue line). All interactions are given in meV. We set $U = 1.0$ eV and $J_H = U/5$.

3.5.2 RKKY Interactions Computed in a Realistic Model

Next let us compute RKKY interactions using results for the susceptibility obtained in section 3.4. For completeness, we compute the RKKY interactions up to the sixth neighbors for different content of interstitial Fe ions. In Fig. 3.6(a) we plot J_1^{RKKY}, J_2^{RKKY} and J_3^{RKKY} shown, correspondingly, in red, green and blue solid lines, and J_4^{RKKY}, J_5^{RKKY} and J_6^{RKKY} shown, correspondingly, in brown, orange and purple dashed lines. We see that the RKKY interactions beyond third nearest neighbors are small in comparison with first, second and third neighbor interactions, and thus, can be neglected in the further analysis.

At small values of y, all considered RKKY interactions are large but for different reasons. While the large antiferromagnetic J_2^{RKKY} and ferromagnetic J_3^{RKKY} interactions can be understood as arising due to the strong peaks in the susceptibility $\chi^{\mathrm{RPA}}(\mathbf{q}, 0)$ near $(\pi, 0)$ and $(0, \pi)$ points, the dominating antiferromagnetic J_1^{RKKY} can not be explained by this reason. As we have shown in the previous section, the first neighbor interaction does not profit from almost diverging susceptibility near the $(\pi, 0)$ and $(0, \pi)$ peaks – these contributions come with opposite signs and cancel one another. Instead,

the strong spin fluctuations in broads region of the Brillouin zone in the vicinity of the M and the Γ points lead to the dominating $J_1^{\rm RKKY}$ interaction.

With a slight increase in the concentration of interstitial Fe ions, $y \leq 0.025$, the large fluctuations of itinerant electrons near $(\pi, 0)$ and $(0, \pi)$ quickly disappear, and the second and third neighbor RKKY interactions become small. However, because the diffuse peak around the M point remains, the value of the first neighbor interaction $J_1^{\rm RKKY}$ practically does not change. Between $0.05 \leq y \leq 0.1$, both $J_2^{\rm RKKY}$ and $J_3^{\rm RKKY}$ interactions become antiferromagnetic, and they remain subdominant with respect to the $J_1^{\rm RKKY}$ interaction.

The strong change in the nearest neighbor coupling $J_1^{\rm RKKY}$ starts at $y > 0.05$. This change is caused by the reduction of fluctuations around the M point. As we can see in Fig. 3.4(b), the RPA susceptibility at $y = 0.1$ does not show any significant fluctuation at around this point. At about $y = 0.11$, the $\chi^{\rm RPA}(\mathbf{q}, 0)$ becomes the strongest in the vicinity of the Γ point. Consequently, the $J_1^{\rm RKKY}$ changes sign and becomes ferromagnetic. In section 3.6, we will show that this strong change in $J_1^{\rm RKKY}$ explains experimental results which find the magnetic order changes from $\mathbf{q}$=$(\frac{\pi}{2}, \frac{\pi}{2})$ double stripe to $\mathbf{q}$=$(\frac{\pi}{2} - \delta, \frac{\pi}{2} - \delta)$ incommensurate spiral.

3.5.3 Derivation of Effective Couplings

Next, we compute the dependence of the effective couplings $J_{ij}^{\rm eff}$ between localized moments on the Fe excess content. To this end, we first need to find Heisenberg exchange couplings J_{ij} which do not change with increasing Fe excess. The values of the effective couplings $J_{ij}^{\rm eff}$ at $y \simeq 0$ were computed by the first-principles electronic structure calculations by Ma *et al.*[27] Up to the third neighbors, these values are equal to $J_1^{\rm eff}$ =2.1 meV, $J_2^{\rm eff}$ =15.8 meV, $J_3^{\rm eff}$ =10.1 meV. As even at $y \simeq 0$, $Fe_{1+y}Te$ has both itinerant and localized electrons, these effective couplings contain both the $J_{ij}^{\rm RKKY}$ interactions and Heisenberg exchange couplings J_{ij}. In order to decompose these contributions, we obtain y-independent J_{ij} couplings by subtracting the RKKY interactions computed by us at $y = 0$ from the values of superexchange interactions provided by Ma *et al.* [27] Then we got Heisenberg exchange couplings to be equal to $J_1 = -3.4$ meV, $J_2 = 11.6$ meV, and $J_3 = 15.1$ meV.

In Fig. 3.6(b), we plot $J_{ij}^{\rm eff}(y) = J_{ij} + J_{ij}^{\rm RKKY}(y)$ as a function of y. We see that

effective couplings J_2^{eff} and J_3^{eff} remain antiferromagnetic for all y, while J_1^{eff} term changes sign at $y = 0.075$. As we will see in the next section, this change of J_1^{eff} is the driving force behind the change in the magnetic order which happens in $Fe_{1+y}Te$ above a critical level of Fe excess.

3.6 Classical Phase Diagram

Due to the interplay of the exchange interactions among localized spins with RKKY interactions induced by the itinerant electrons, $Fe_{1+y}Te$ compounds bare many similarities with extensively studied double-exchange magnets and, especially, manganites. It was shown that effective coupling constants in manganites might be significantly modified by charge doping, which in turn leads to the appearance of new phases in the classical phase diagram. [100, 101, 102] We expect a similar behavior here: the phase diagram of the effective model (Eq. 3.10) might show the evolution of the magnetic order with charge doping due to interstitial Fe.

Here we compute classical phase diagram of the model (Eq. 3.10) by numerical minimization of its classical energy with a constraint that all spins have unit length. Our findings are summarized in the classical phase diagram presented in Fig. 3.7. To look for a wide variety of states, we introduce four sublattices, labelled as 0, 1, 2, and 3 (see Fig. 3.8) and perform full minimization of the classical energy. With each sublattice we associate a local frame given by angles $\varphi_0, \varphi_1, \varphi_2, \varphi_3$. We define the global reference frame by setting $\varphi_0 = 0$. In addition, we consider only spin configurations which might be characterized by a single $\mathbf{q}$-spirals, such that translating from site to site of the same sublattice the magnetic moment rotates by an angle $\theta = \mathbf{qr}$, where $\mathbf{r} = 2ma_x + 2na_y$, m and n are integers, $\mathbf{a} = (a_x, a_y)$ is the lattice vector. Then, the generic expression for the on-site magnetization is given by

$$\bar{\mathbf{S}}_\mu(\mathbf{r}) = \hat{\mathbf{x}} \sin(\mathbf{q}\cdot\mathbf{r} + \varphi_\mu) + \hat{\mathbf{y}} \cos(\mathbf{q}\cdot\mathbf{r} + \varphi_\mu), \tag{3.23}$$

where $\mu = 0, 1, 2, 3$ is the sublattice index. Substituting $\bar{\mathbf{S}}_\mu(\mathbf{r})$ into the Eq. 3.10 yields the classical energy $E_{\text{cl}} = E(\{\varphi_\mu\}, \mathbf{q})$. The explicit expression for the classical energy is rather cumbersome and, for convenience, is given in the Eq. 3.32. We minimize E_{cl} numerically and for each set of parameters find the classical ground state characterized

by $\varphi_1, \varphi_2, \varphi_3, q_x$ and q_y. In our computation we fix the second neighbor biquadratic and ring-like exchanges equal to $K_2 = -K_{diag}$=3.0 meV and vary two other parameters of the model – the nearest neighbor biquadratic exchanges K_1 and y.

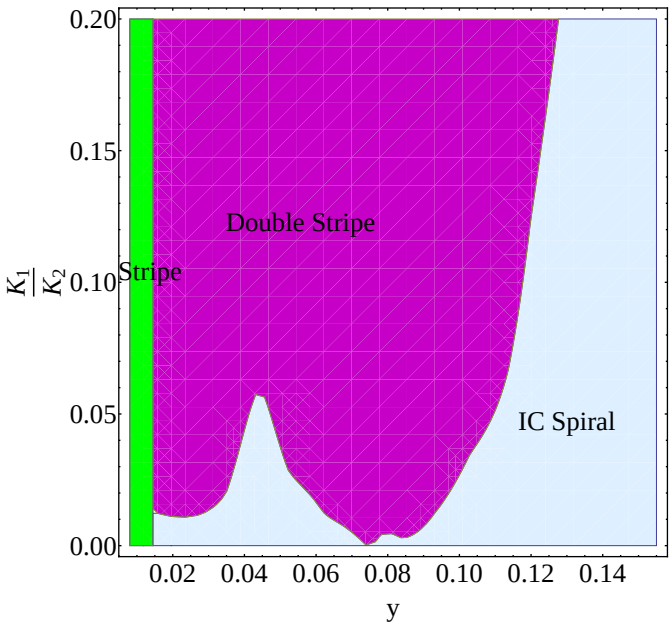

Figure 3.7: Magnetic phase diagram of effective low-energy model (10) as a function of Fe excess y and the ratio of the nearest neighbor and second neighbor biquadratic exchanges, $\frac{K_1}{K_2}$, computed with $J_1^{\text{eff}}(y) = -3.4 + J_1^{\text{RKKY}}(y)$, $J_2^{\text{eff}}(y) = 11.6 + J_2^{\text{RKKY}}(y)$, $J_3^{\text{eff}}(y) = 15.1 + J_3^{\text{RKKY}}(y)$. All interactions are given in meV. We take $K_2 = 3$ meV.

In Fig. 3.8(a)-(c), we draw possible real space spin orderings presented in Fig. 3.7. Among all possible states, in the parameter space presented in the phase diagram, only three states are realised: the stripe phase characterized by $\varphi_1 = 0, \varphi_2 = \pi, \varphi_3 = \pi, q_x = 0, q_y = 0$ shown in Fig. 3.8(a), the double stripe phase characterized by $\varphi_1 = 0, \varphi_2 = 0, \varphi_3 = \pi, q_x = \pi/2, q_y = \pi/2$ shown in Fig. 3.8(b) and the incommensurate spiral (labeled as IC) state shown in Fig. 3.8(c) characterized by $\varphi_1 = \pi/2 - \delta, \varphi_2 = \pi - 2\delta, \varphi_3 = \pi/2 - \delta, q_x = \pi/2 - \delta, q_y = \pi/2 - \delta$. Note, that in this figure we show the IC with an exaggerated canting angle.

To clarify the structure of these different orderings, we take the Fourier transforms

of the ground state spin configuration obtained by the minimization and then compute the spin structure factor in each phase to show which wavevectors the configuration mostly consists of. As expected, the structure factor exhibits peaks at the ordering wavevectors: $\mathbf{Q} = (0, \pi)$ for the stripy phase, the $\mathbf{Q} = (\pi/2, -\pi/2)$ for the bicollinear double stripe phase, and the $\mathbf{Q} = (\pi/2 - \delta, -\pi/2 + \delta)$ for the IC phase.

The structure of the phase diagram (see Fig. 3.8) is as follows. At small value of y, there is a thin strip of the stripe phase. This phase is stabilized by a strong J_2^{eff} coupling (see Fig. 3.6(b)). The stripe phase quickly disappears because J_2^{eff} decreases rapidly with increasing y. We believe that the stripe phase has not been observed in $Fe_{1+y}Te$, because all known compounds belonging to this family are, actually, non-stoichiometric and have amount of interstitial Fe significantly larger than the boundary value of $y = 0.014$, below which the stripe phase is stable.

The central region in the phase diagram ($y > 0.014$) is occupied by the bicollinear double stripe state. This is the state which is experimentally observed in Fe_{1+y}Te compound with a low level of Fe excess. The stability of this phase over a wide range of parameters is explained by the smallness of the effective nearest neighbor coupling J_1^{eff} and relatively strong strength of the third neighbor coupling J_3^{eff}. The biquadratic couplings K_1 and K_2 also play an important role in stabilizing this state. Note that except the region near $y = 0.075$, a finite value of nearest neighbor biquadratic coupling K_1 is necessary to stabilize the double stripe phase over the incommensurate spiral states. In this region, the effective nearest neighbor coupling J_1^{eff} is equal to zero or very small compared other interactions, and the bicollinear double stripe state is realized even in the absence of the biquadratic exchange. The rest of the phase diagram is occupied by an IC phase (see, Fig. 3.8(c)). This is a (q, q) spiral state experimentally observed at sufficiently large y.

In experiment [84], the phase transition from the bicollinear double stripe to the IC phase has been observed approximately at $y \approx 0.11$. Around this point, our phase diagram shows the transition for $\frac{K_1}{K_2} \simeq 0.1$ which seems to be a realistic ratio taking into account that the magnetoelastic coupling mostly supports the biquadratic and ring-like exchanges for second neighbors.

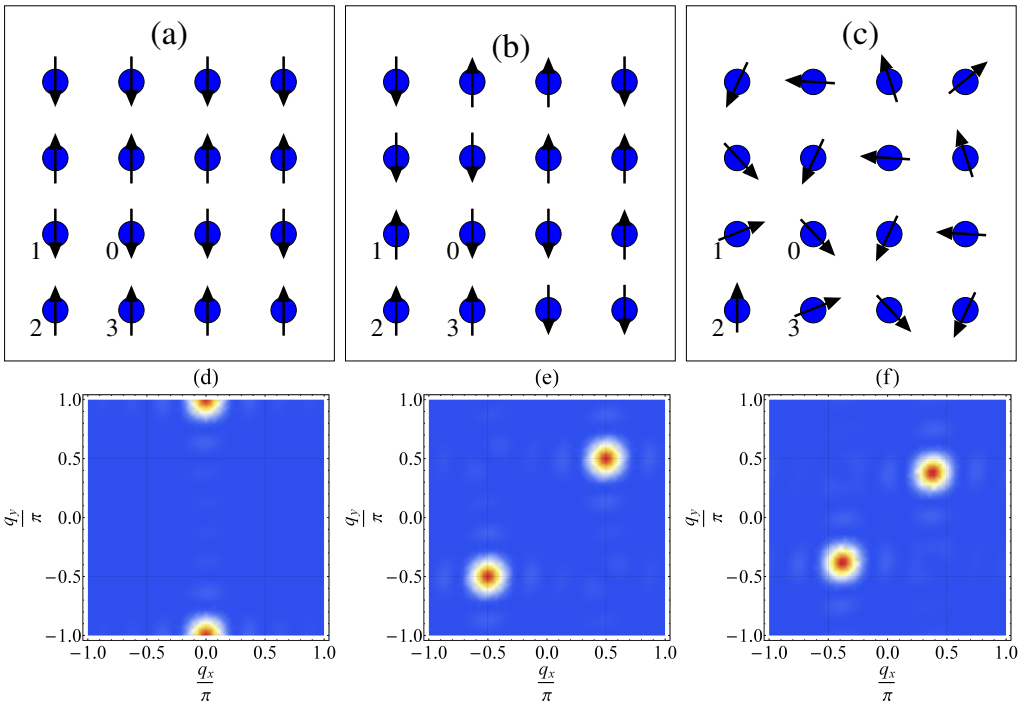

Figure 3.8: Schematic representations of spin orderings in the ground state obtained by the minimization of the classical energy with respect to $\varphi_1, \varphi_2, \varphi_3, q_x$ and q_y: (a) $\varphi_1 = 0, \varphi_2 = \pi, \varphi_3 = \pi, q_x = 0, q_y = 0$ in the stripe phase, (b) $\varphi_1 = 0, \varphi_2 = 0, \varphi_3 = \pi, q_x = \pi/2, q_y = \pi/2$ in the double stripe phase, (c) $\varphi_1 = \pi/2 - \delta, \varphi_2 = \pi - 2\delta, \varphi_3 = \pi/2 - \delta, q_x = \pi/2 - \delta, q_y = \pi/2 - \delta$, (d)-(e) The structure factors computed for magnetic orders displayed in (a)-(c), respectively. Bright spots correspond to the sharp peaks, which appear at the corresponding ordering wavevectors.

3.7 Summary

In summary, we have studied the evolution of magnetic order in $Fe_{1+y}Te$ with y. We derived an effective super-exchange model describing magnetic properties of $Fe_{1+y}Te$ in which we took into account both the long-range RKKY-type spin-spin interaction that results from integrating out the itinerant electrons and the biquadratic interactions due to magnetoelastic coupling. We computed the classical phase diagram of the this model. We showed that at small y, the magnetic order for $Fe_{1+y}Te$ is different from the parent compounds of ferropnictides. This difference can be understood due to presence of the

significant antiferromagnetic J_3^{eff} coupling in the effective model (10), which has mostly localized origin. Above some critical value of y, the phase diagram shows the transition from the bicollinear double stripe to the incommensurate spiral state. This transition is driven by the significant changes in the n.n. J_1^{eff} interaction with increasing y. This change is caused by the y-dependent RKKY part of the interaction which for $y > 0.075$ leads to a flip of the sign of J_1^{eff} to be ferromagnetic. Experimental data showing the sign of J_1^{eff} to be dependent on the interstitial Fe concentration would be a very strong validation of our model.

The proposed theory requires the coexistence of both localized and itinerant electrons, and it is in line with a more generic idea [30, 58, 64, 65, 66, 67] that in any compound belonging to the ferropnictide's and ferrochalcogenide's families, a certain percentage of electronic states are localized and phase separated from itinerant electrons.

3.8 Technical Details for Chapter 3

3.8.1 Derivation of Biquadratic Exchange Couplings

There are several microscopic mechanisms which lead to non-Heisenberg exchange couplings such as, e.g., the biquadratic and ring exchanges. Among all of them, one of the most effective ways to induce a fairly strong non-Heisenberg exchange is through magnetoelastic mechanism.

Here, we give a brief discussion of the possible magnetoelastic origin of the first and the second neighbor biquadratic exchange interactions in $Fe_{1+y}Te$. In order to consider the magnetoelastic coupling, we assume that lattice distortions are small and, thus, there is a linear regime in which exchange interactions and elastic energies depend only on the distance between lattice sites. As the magnetoelastic Hamiltonian involves more than one normal mode of a square, it is convenient to follow notations of I.Paul *et al* [103], and describe the lattice distortions by the strain tensor given by

$$u_{ij}(\mathbf{r}) = u_{ij} + \frac{\imath}{2}\sum_{q\neq 0}(q_i u_j(\mathbf{q}) + q_i u_j(\mathbf{q}))e^{\imath\mathbf{qr}}. \tag{3.24}$$

The $q = 0$ lattice modulation is characterized by either the overall compression strain $u_{xx} \equiv \partial_x u_x$ or $u_{yy} \equiv \partial_y u_y$, or by the shear strain $u_{xy} \equiv \partial_y u_x + \partial_x u_y$. The non-uniform

lattice modulation can be expressed by the Fourier transform of the displacements $\mathbf{u}(\mathbf{r})$ at the lattice point $\mathbf{r}$ with dominant contributions from $\mathbf{q}_5 = (\pi, \pi)$, $\mathbf{q}_6 = (\pi, 0)$ and $\mathbf{q}_7 = (0, \pi)$ modes. We note, that the uniform compression strains u_{xx} and u_{yy} do not couple to magnetic degrees of freedom. For shortness of notations, we call $u(\mathbf{q}_5) \equiv u_5$, $u(\mathbf{q}_6) \equiv u_6$ and $u(\mathbf{q}_7) \equiv u_7$.

The lattice distortions described by u_{xy}, u_5 and u_6 are shown in Fig. 3.9(a),(b) and (c), respectively. We see that the uniform shear mode, u_{xy}, corresponds to the monoclinic distortion. This mode generates a distortion of the square with short and long diagonals. The non-uniform mode corresponding to u_5 generates a distortion with ladders along the diagonal of shortened and lengthened nearest neighbor bonds. The non-uniform mode corresponding to the u_6 distortion for which the bonds are alternatively shorten and lengthen in the x-direction. The mode corresponding to the u_7 distortion would have the same picture but rotated by 90 degrees.

Then the magnetoelastic term arising from the dominant distortion modes is given by

$$\begin{aligned} H_{\mathrm{ME}} &= g_1(\mathbf{S}_1 \cdot \mathbf{S}_3 - \mathbf{S}_0 \cdot \mathbf{S}_2)u_{xy} \\ &+ g_2\left[(\mathbf{S}_2 \cdot \mathbf{S}_3 - \mathbf{S}_0 \cdot \mathbf{S}_1)u_5^x + (\mathbf{S}_1 \cdot \mathbf{S}_2 - \mathbf{S}_0 \cdot \mathbf{S}_3)u_5^y\right] \\ &+ g_3\left[(\mathbf{S}_2 \cdot \mathbf{S}_3 + \mathbf{S}_0 \cdot \mathbf{S}_1)u_6^x + (\mathbf{S}_1 \cdot \mathbf{S}_2 + \mathbf{S}_0 \cdot \mathbf{S}_3)u_7^y\right]. \end{aligned} \tag{3.25}$$

The elastic term grows quadratically with the distortion and, thus, can be written as

$$H_{\mathrm{elast}} = \frac{c_{66}}{2}u_{xy}^2 + \frac{\Omega_1}{2}u_5^2 + \frac{\Omega_2}{2}(u_6^2 + u_7^2)\ , \tag{3.26}$$

where the constants c_{66}, Ω_1, and Ω_2 represent the elastic stiffness of the different lattice distortions described by u_{xy}, u_5, u_6 and u_7, respectively.

The equilibrium lattice distortions u_{xy}, u_5, u_6, and u_7 are found from the condition

of a minimum of the energy:

$$\begin{aligned} u_{xy} &= -\frac{g_1}{c_{66}}(\mathbf{S}_1\cdot\mathbf{S}_3-\mathbf{S}_0\cdot\mathbf{S}_2) \\ u_5^x &= -\frac{g_2}{\Omega_1}(\mathbf{S}_2\cdot\mathbf{S}_3-\mathbf{S}_0\cdot\mathbf{S}_1) \\ u_5^y &= -\frac{g_2}{\Omega_1}(\mathbf{S}_1\cdot\mathbf{S}_2-\mathbf{S}_0\cdot\mathbf{S}_3) \\ u_6 &= -\frac{g_3}{\Omega_2}(\mathbf{S}_2\cdot\mathbf{S}_3+\mathbf{S}_0\cdot\mathbf{S}_1) \\ u_7 &= -\frac{g_3}{\Omega_2}(\mathbf{S}_1\cdot\mathbf{S}_2+\mathbf{S}_0\cdot\mathbf{S}_3). \end{aligned} \tag{3.27}$$

Integrating out lattice distortions, we obtain the following biquadratic Hamiltonian:

$$\begin{aligned} H_{\rm bi} &= -\frac{g_1^2}{2c_{66}}(\mathbf{S}_1\cdot\mathbf{S}_3-\mathbf{S}_0\cdot\mathbf{S}_2)^2 \\ &- \frac{g_2}{2\mathbf{\Omega}_1}[(\mathbf{S}_2\cdot\mathbf{S}_3-\mathbf{S}_0\cdot\mathbf{S}_1)^2+(\mathbf{S}_1\cdot\mathbf{S}_2-\mathbf{S}_0\cdot\mathbf{S}_3)^2] \\ &- \frac{g_3}{2\mathbf{\Omega}_2}[(\mathbf{S}_2\cdot\mathbf{S}_3+\mathbf{S}_0\cdot\mathbf{S}_1)^2+(\mathbf{S}_1\cdot\mathbf{S}_2+\mathbf{S}_0\cdot\mathbf{S}_3)^2]. \end{aligned} \tag{3.28}$$

Here it is convenient to rewrite this expression explicitly in the form first and second neighbor biquadratic interactions and of the for of the ring exchange:

$$\begin{aligned} H_{\rm bi} = \quad & -(\frac{g_2^2}{2\mathbf{\Omega}_1}+\frac{g_3^2}{2\mathbf{\Omega}_2})[(\mathbf{S}_2\cdot\mathbf{S}_3)^2+(\mathbf{S}_0\cdot\mathbf{S}_1)^2+(\mathbf{S}_1\cdot\mathbf{S}_2)^2+(\mathbf{S}_0\cdot\mathbf{S}_3)^2] \\ & -\frac{g_1^2}{2c_{66}}[(\mathbf{S}_1\cdot\mathbf{S}_3)^2+(\mathbf{S}_0\cdot\mathbf{S}_2)^2] \\ & +(\frac{g_2^2}{\mathbf{\Omega}_1}-\frac{g_3^2}{\mathbf{\Omega}_2})[(\mathbf{S}_2\cdot\mathbf{S}_3)(\mathbf{S}_0\cdot\mathbf{S}_1)+(\mathbf{S}_1\cdot\mathbf{S}_2)(\mathbf{S}_0\cdot\mathbf{S}_3)] \\ & +\frac{g_1^2}{c_{66}}(\mathbf{S}_1\cdot\mathbf{S}_3)(\mathbf{S}_0\cdot\mathbf{S}_2) \end{aligned} \tag{3.29}$$

$$\begin{aligned} = \quad & K_1\sum_{\langle ij\rangle}(\mathbf{S}_i\cdot\mathbf{S}_j)^2+K_2\sum_{\langle\langle ij\rangle\rangle}(\mathbf{S}_i\cdot\mathbf{S}_j)^2 \\ & +K_\Box\sum_{\Box}(\mathbf{S}_i\cdot\mathbf{S}_j)(\mathbf{S}_k\cdot\mathbf{S}_l)+K_{\rm diag}\sum_{\langle\langle ij\rangle\rangle}(\mathbf{S}_1\cdot\mathbf{S}_3)(\mathbf{S}_0\cdot\mathbf{S}_2)\ , \end{aligned} \tag{3.30}$$

where

$$\begin{aligned} K_1 &= -(\frac{g_2^2}{\Omega_1} + \frac{g_3^2}{\Omega_2}) \\ K_2 &= -\frac{g_1^2}{c_{66}} \\ K_\Box &= \frac{g_2}{\Omega_1} - \frac{g_3}{\Omega_2} \\ K_{\rm diag} &= \frac{g_1^2}{c_{66}} \end{aligned}$$

The first term with a strength K_1 describes the biquadratic exchange coupling between nearest neighbors. The second term with a strength K_2 is the second neighbor biquadratic exchange. The third term is the ring exchange with a strength $K_\Box$. The last term with a strength $K_{\rm diag}$ is a type of ring exchange which couples spins on diagonals.

Not all the terms have the equal strength. Because non-uniform strains u_5, u_6, and u_7 are much weaker than the shear distortion u_{xy}, the latter has the smallest elastic stiffness. Consequently, we have

$$\frac{g_2}{\Omega_1}, \frac{g_3}{\Omega_2} \ll \frac{g_1}{c_{66}} \ . \tag{3.31}$$

Thus, in our calculations we neglect the ring exchange term, $K_\Box$, but took into account $K_{\rm diag} = -K_2$ interaction. We also assume that $K_1 < K_2$.

3.8.2 Classical Energy

Here, we present the classical energy of the local spin model of Eq. 3.10, as a function of the local angles ϕ_i and the ordering vector (qx, qy):

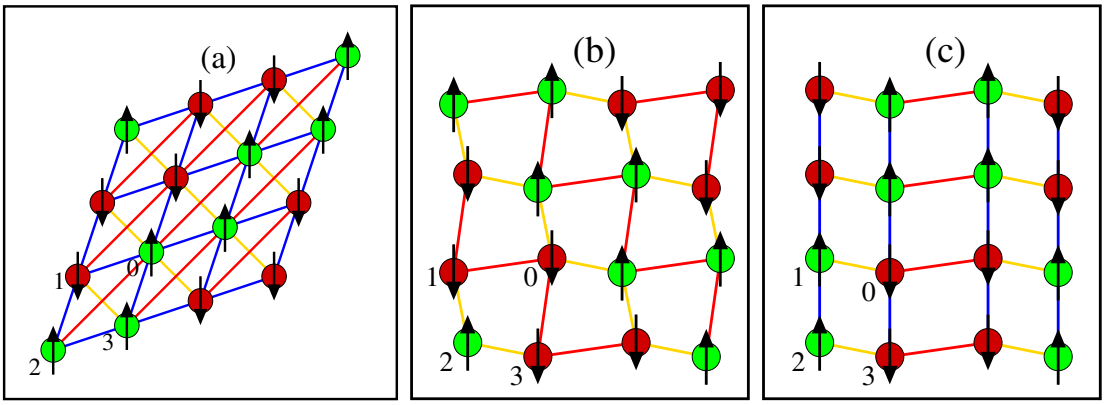

Figure 3.9: Dominant modes of lattice distortion in $Fe_{1+y}Te$. (a) A uniform shear mode, u_{xy}. This mode generates a distortion of the square with short and long diagonals. This mode corresponds to the monoclinic distortion. (b) The non-uniform mode corresponding to $u_5^x = u_5^y$. This mode generates a distortion which shortened nearest neighbor bonds and lengthen the diagonal bonds. (c) The non-uniform mode corresponding to the u_6 distortion. Bonds are alternatively shorten and lengthen in the x-direction. The mode corresponding to the u_7 distortion would have the same picture but rotated by 90 degrees. We use the following convention: red bonds are lengthened, yellow bonds are shortened, blue bonds remain of the same length. Green sites have spins ferromagnetic with each other, and these spins are antiferromagnetic with spins at the red sites.

$$
\begin{aligned}
E_{cl} &= \frac{S^2}{4}\Big[J_1\Big(\cos\varphi_1+\cos(\varphi_1+2q_x)+\cos(\varphi_3-\varphi_2)+\cos(\varphi_3-(\varphi_2+2q_x))+\cos\varphi_3 \\
&+ \cos(\varphi_3+2q_y)+\cos(\varphi_1-\varphi_2)+\cos(\varphi_1-(\varphi_2+2q_y))\Big) \\
&+ J_2\Big(\cos\varphi_2+\cos(\varphi_2+2q_x+2q_y)+\cos(\varphi_1-(\varphi_3+2q_y))+\cos(\varphi_1+2q_x-\varphi_3) \\
&+ \cos(\varphi_2+2q_y)+\cos(\varphi_1-\varphi_3)+\cos(\varphi_2+2q_x)+\cos((\varphi_1+2q_x)-(\varphi_3+2q_y))\Big) \\
&+ 4J_3\Big(\cos 2q_x+\cos 2q_y\Big)+K_1S^2\Big(\cos^2\varphi_1+\cos^2(\varphi_1+2q_x)+\cos^2(\varphi_3-\varphi_2) \\
&+ \cos^2(\varphi_3-(\varphi_2+2q_x))+\cos^2\varphi_3+\cos^2(\varphi_3+2q_y)+\cos^2(\varphi_1-\varphi_2) \\
&+ \cos^2(\varphi_1-(\varphi_2+2q_y))\Big)+K_2S^2\Big(\cos^2\varphi_2+\cos^2(\varphi_2+2q_x+2q_y) \\
&+ \cos^2(\varphi_1-(\varphi_3+2q_y))+\cos^2(\varphi_1+2q_x-\varphi_3)+\cos^2(\varphi_2+2q_y)+\cos^2(\varphi_1-\varphi_3) \\
&+ \cos^2(\varphi_2+2q_x)+\cos^2((\varphi_1+2q_x)-(\varphi_3+2q_y))+\cos\varphi_2\cos(\varphi_1-\varphi_3) \\
&+ \cos(\varphi_2+2q_x)\cos(\varphi_1+2q_x-\varphi_3)+\cos(\varphi_2+2q_y)\cos(\varphi_1-\varphi_3-2q_y) \\
&+ \cos(\varphi_2+2q_x+2q_y)\cos(\varphi_1+2q_x-\varphi_3-2q_y)\Big)\Big]\ .
\end{aligned}
$$

Chapter 4

Magnetic Excitations in Hyperhoneycomb Kitaev Systems

4.1 Introduction

The Kitaev materials [7] – transition-metal oxides with partially filled $4d$ and $5d$ shells on the tri-coordinated lattice structures – have recently attracted much interest in condensed matter physics [6, 7, 32, 33, 104, 105, 106]. Among the Kitaev materials, the most studied systems have magnetic moments arising either from Ir^{4+} or Ru^{3+} ions. These ions, due to strong spin-orbit coupling (SOC), are characterized by effective $J_{\text{eff}} = 1/2$ pseudospins. In all these systems, edge-sharing IrO_6 or $RuCl_6$ octahedra provide 90° paths for the dominant bond-directional Ising-like interaction among magnetic moments with the exchange easy axis which depends on the spatial orientation of the bond [6, 105]. This interaction is precisely the Kitaev interaction that drives quantum spin liquid behavior on all tri-coordinated lattices with equidistant bonds and approximately 120° bond angles at every vertex [5, 38]. This is why these materials are considered to be candidates for realization of Kitaev model [5].

Unfortunately for the search of exciting quantum spin liquids, all so far known Kitaev materials order magnetically at low enough temperatures [8, 9, 10, 11, 96, 107, 108, 109, 110]. Nevertheless, the magnetic ground states of the Kitaev materials are not at all boring. In these materials, a variety of non-collinear magnetic ground state configurations may emerge as a result of the competition among anisotropic exchange

interactions [8, 9, 10, 11, 110], or from the competition between exchange couplings and external magnetic field [12, 111, 112, 113]. Of particular interest are the possibility of realization of complex magnetic states with particle- or soliton-like magnetization modulations, e.g. Z_2 vortex crystal [114, 115], incommensurate spirals, or multiple-$\mathbf{Q}$ magnetic orders [40, 112, 113, 116, 117, 118, 119, 120, 121], which might appear in real materials because the strong spin-orbit coupling entangles real-space and spin-space anisotropies. Indeed, measurements on the three structural polytypes of the lithium iridate, α, β, γ-Li_2IrO_3, revealed that all of them order into remarkably similar non-coplanar spiral phases, where spirals on neighboring sublattices are counter-rotating [8, 9, 10, 11, 110].

In this work we focus on the analysis of the microscopic origin and the dynamics of the counterrotating spiral order observed in the β-Li_2IrO_3 compound [9, 11, 12], which was discovered by Takayama *et al* [11]. The origin of the unusual magnetic order in this compound has been a subject of intensive investigation by two theoretical groups [40, 41, 119, 122, 123, 124]. Despite the fact that these two groups used different models and utilized different approaches, both groups found that counterrotating spirals required a ferromagnetic nearest neighbor Kitaev term.

In the first scenario, proposed by Lee *et al* [40, 41], the experimentally observed counterrotating spiral was obtained in the dubbed J-K-Γ model using a classical approach and the soft-spin analysis. In the second scenario, proposed by Kimchi *et al* [119, 123, 124], acheived within a minimal 1D model on an isolated zigzag chain. With a help of Klein duality transformation mapping the counterrotating spiral to the co-rotating spiral of the dual J_1-J_2 Hamiltonian [124], Kimchi *et al* also managed to identifiy some features in the dynamical structure factor that could be tested via polarized and unpolarized inelastic neutron scattering or resonant inelastic x-ray scattering experiments.

In this paper we study the magnetism of β-Li_2IrO_3 compound using J-K-Γ model which is the common minimal model for Kitaev materials [40, 41]. Our ultimate goal is to compute the spin dynamics in this compound without being restricted to a single zigzag chain, since not all of the features of the experimentally observed ground state can be captured within one-chain approach. This is, apparently, not an easy task. The computation of spin dynamics is tricky even when all magnetic moments rotate uniformly,

through the same **Q**-wavevector. It is, certainly, significantly more challenging when a magnetic order consists of a collection of counterrotating incommensurate spirals. To attack this problem, we search for the simplest commensurate state which has the same irreducible representation, similar periodicity and bear the main feature of the experimentally observed ground state, i.e., the counterrotation. Using the Luttinger-Tisza approach [125, 126] and dynamical simulation based on the Landau-Lifshitz-Gilbert equations[127, 128] we show that in the red region of our phase diagram (see Fig. 4.2), the region of experimentally relevant parameters, the state we find has non-linear modulation with a periodicity-3 and consists of the majority and the minority spins. Our state can not be described by a single **Q** but mimics well the experimentally observed counterrotation of even and odd sites belonging to each zigzag chain. Then, we take advantage of the commensurability of this "period 3"-state and study the spin dynamics of the J-K-Γ model using a semiclassical approach.

The chapter has the following structure. In sections 4.2 and 4.3, we review the details of J-K-Γ model on the hyperhoneycomb lattice and discuss the classical phase diagram of this model obtained from the Luttinger-Tisza approach. In section 4.4, we further examine the region of the phase diagram representing incommensurate phase IC_a using a dynamical simulation based on the Landau-Lifshitz-Gilbert equations which allows us to explore multiple-**Q** states. From the simulations, we found a "period 3"-state, which we described using a notation of majority and minority spins. We study this "period 3"-state in detail in section 4.4. Here we also perform the analysis of the symmetry of this state and reveal that in terms of magnetic vectors it transforms as (A_a, C_b, F_c) in agreement with experimental findings.[9] In section 4.5, we study the spin dynamics of the "period 3"-state. The commensurability of the "period 3"-state in enlarged magnetic unit cell composed of three orthorhombic unit cells along the **a** axis allows us to study the spin dynamics of the J-K-Γ model on infinite lattice using the semiclassical approach. We first calculated the linear spin wave spectrum, and then computed the dynamical structure factor by diagonalizing the spin wave Hamiltonian. The only difficulty which we encounter in our computation is the complicated band-folding due to large unit cell. We give a brief discussion in section 4.6. Technical details and derivations are relegated to section 4.7.

4.2 J-K-Γ model on the Hyperhoneycomb Lattice

The hyperhoneycomb lattice of $\beta-Li_2IrO_3$ has a primitive unit cell with 4 Ir ions but is more conveniently described by the orthorhombic unit cell containing 4 primitive cells and thus 16 Ir ions (see Fig. 4.1). The Ir atoms form zigzag chains stacked along the **c**-axis and directed alternatingly along $\mathbf{a} \pm \mathbf{b}$-directions. For calculating the spin structure, it is useful to define the "Kitaev" axes $\mathbf{x} = \frac{\mathbf{a}+\mathbf{c}}{\sqrt{2}}$, $\mathbf{y} = \frac{\mathbf{c}-\mathbf{a}}{\sqrt{2}}$, and $\mathbf{z} = -\mathbf{b}$, as compared to the orthorhombic **a**, **b**, **c** axes. The effective moment of the Ir ions is about 1.7 μ_B,[9, 11, 12] which is very close to the expected value for the ideal pseudospins $J_{\text{eff}} = 1/2$. Hereafter, we denote pseudospins simply as S.

While the edge-sharing IrO_6 octrahedra and tri-coordinated lattice structure give rise to the dominant Kitaev interaction, additional couplings among pseudospins are allowed by symmetry and are not negligible. Thus, the realistic Hamiltonian has the following general form [40, 116]:

$$H = \sum_{\langle ij\rangle \in \alpha,\beta(\gamma)} \left(J\, \mathbf{S}_i \cdot \mathbf{S}_j + K\, S_j^{\gamma} S_j^{\gamma} \pm \Gamma (S_i^{\alpha} S_j^{\beta} + S_i^{\beta} S_j^{\alpha}) \right), \tag{4.1}$$

where J, K and Γ denote nearest neighbor Heisenberg, Kitaev, and symmetric anisotropic interactions. In the above equation, the indices α, β, and γ running through x, y, and z which label the spin component involved in the Kitaev (Ising) coupling on the corresponding bond. Symmetry arguments require that the Γ interaction has a different sign on the x and y bonds, and the sign must also be flipped between "primed" and "unprimed" bonds of the same type (see Fig. 4.1 for the conventions for primed and unprimed bonds). We use the convention that the Γ term has "+" sign on x and y' bonds and "-" sign on x' and y bonds.

The full parameter space of the model (eq. 4.1) can be conveniently described by the following parameterization:

$$J = \sin r \cos \phi,\ K = \sin r \sin \phi,\ \Gamma = -\cos r, \tag{4.2}$$

where $\phi \in [0, 2\pi)$ is and $r \in [0, \frac{\pi}{2}]$. Here we only focus on the range of parameters which are believed to be relevant for $\beta-Li_2IrO_3$, i.e., the ferromagnetic Kitaev interaction, $K < 0$, and antiferromagnetic Heisenberg interaction, $J > 0$, which correspond to $\phi \in [\frac{3\pi}{2}, \pi]$. The sign flips of Γ are explicitly taken into account in the model (eq. 4.1),

so in the following we assume $\Gamma < 0$. Also, with this parametrization $r = 0$ corresponds to the pure Γ model ($J = K = 0$) and $r = \pi/2$ corresponds to the J-K model ($\Gamma = 0$).

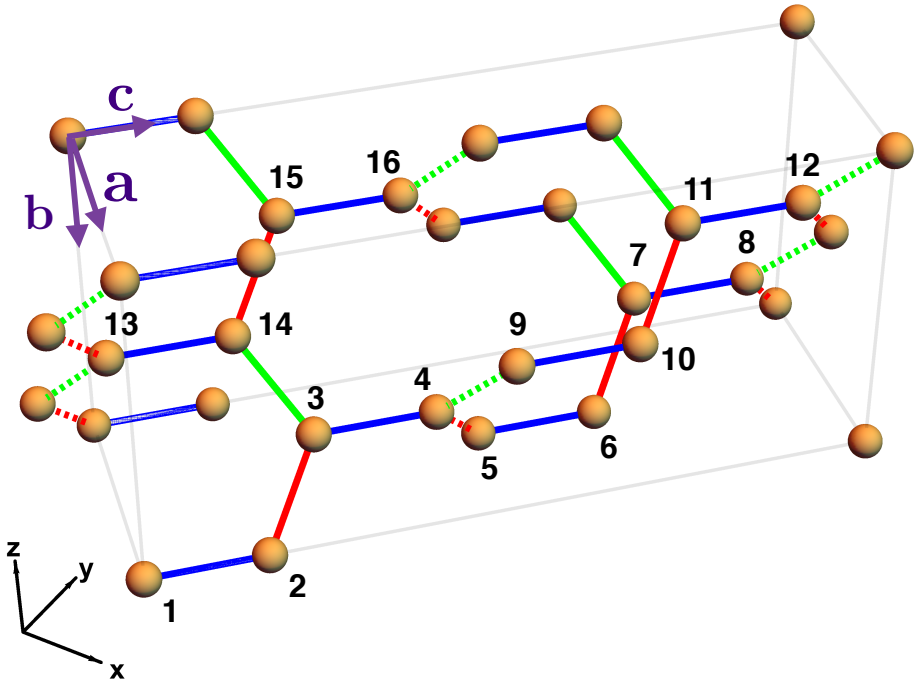

Figure 4.1: The lattice structure of β-Li_2IrO_3. The bonds are color coded according to their Kitaev label: red, green and blue correspond to x, y and z bonds, respectively. Dashed and solid red and green bonds denote x' and y' versus x and y bonds, respectively .

4.3 Classical Phase Diagram from the Luttinger-Tisza Approach

We start by exploring the classical ground state of the model (eq. 4.1). It is convenient to rewrite the Hamiltonian (eq. 4.1) in a more compact form,

$$H = \sum_{\langle ij \rangle} \sum_{\alpha,\beta} \sum_{\mu,\nu} S^{\alpha}_{i,\mu} H^{\alpha\beta}_{i\mu,j\nu} S^{\beta}_{j,\nu}, \tag{4.3}$$

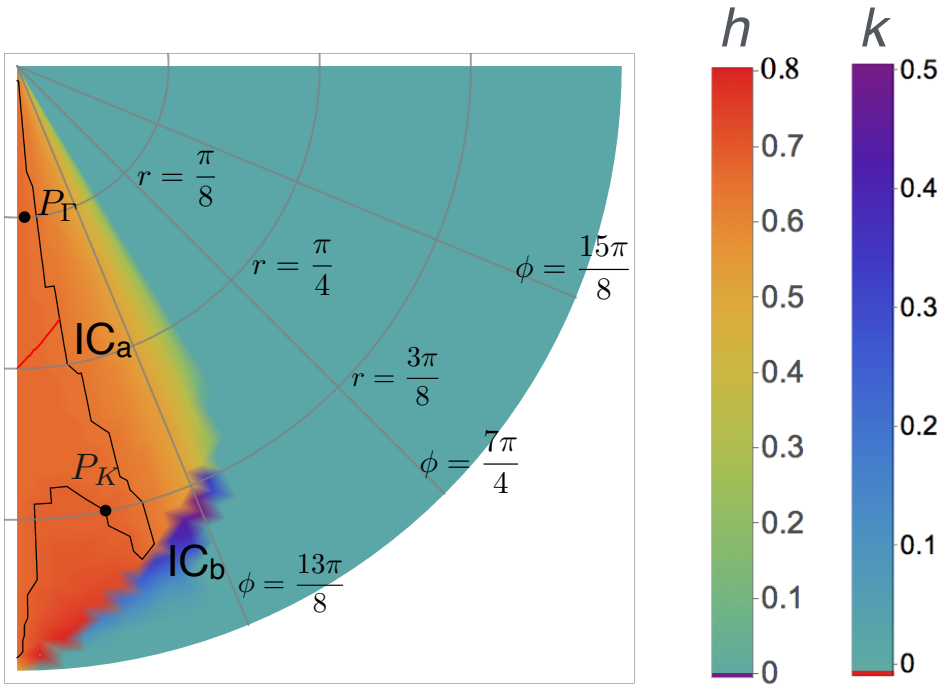

Figure 4.2: (Color online) Classical phase diagram of the J-K-Γ model on the hyperhoneycomb lattice based on the Luttinger-Tisza method. The colors on the contour plot represent the magnitude of the components h and k of the wavevector $\mathbf{Q} = h\mathbf{b_1} + k\mathbf{b_2} + l\mathbf{b_3}$ that minimizes the classical energy (4.5). There are three phases presented in the phase diagram. The first phase (light blue) is the simple $\mathbf{Q} = (0, 0, 0)$ phase. The second phase is the IC_a-phase (mostly orange) is an incommensurate spiral with $\mathbf{Q} = (h, 0, 0)$ running along the a orthorhombic axis. In a large portion of this phase inside the black line, the magnitude of h is very close to $\frac{2}{3}$. The third phase (small bluish purple region) is the IC_b-phase, an incommensurate spiral with $\mathbf{Q} = (0, k, 0)$ running along running along the b orthorhombic axis. Two points shown in the phase diagram are P_K ($r = \frac{3\pi}{8}$ and $\phi = \frac{25\pi}{16}$) and P_Γ ($r = \frac{\pi}{8}$ and $\phi = \frac{97\pi}{64}$). The red line separates two qualitatively different states inside IC_a phase, which we discuss in section 4.4.

where $\mu, \nu = 1, 16$ are the sublattice indeces. Defining

$$S^{\alpha}_{i,\mu} = \sum_{\mathbf{k}} \; e^{i \; \mathbf{k}\cdot\mathbf{R}_i} \; S^{\alpha}_{\mathbf{k},\mu} \; , \tag{4.4}$$

where wavevectors $\mathbf{k}$ belong to the orthorhombic Brillouin zone (BZ), we get the classical energy per site to be equal to

$$\epsilon = \frac{1}{N_{uc}} \sum_{\mathbf{k}} \sum_{\alpha,\beta} \sum_{\mu,\nu} S^{\alpha}_{\mathbf{k},\mu} H^{\alpha\beta}_{\mu\nu}(\mathbf{k}) S^{\beta}_{-\mathbf{k},\nu}. \tag{4.5}$$

Here $N_{uc} = \frac{N}{16}$ is the number of unit cells, N is the total number of sites, and each of the $H_{\mu\nu}(\mathbf{k})$ matrix is given by

$$H_{\mu\nu}(\mathbf{k}) = \begin{pmatrix} H^{xx}_{\mu\nu}(\mathbf{k}) & H^{xy}_{\mu\nu}(\mathbf{k}) & H^{xz}_{\mu\nu}(\mathbf{k}) \\ H^{xy}_{\mu\nu}(\mathbf{k}) & H^{yy}_{\mu\nu}(\mathbf{k}) & H^{yz}_{\mu\nu}(\mathbf{k}) \\ H^{xz}_{\mu\nu}(\mathbf{k}) & H^{yz}_{\mu\nu}(\mathbf{k}) & H^{zz}_{\mu\nu}(\mathbf{k}) \end{pmatrix}. \tag{4.6}$$

To find the classical minimum, we need to minimize the energy (eq. 4.5) under the strong constraints, $\mathbf{S}^2_{i,\mu} = S^2 \; \forall(i,\mu)$. We will do this by applying the Luttinger-Tisza (LT) method [125, 126], which amounts to replacing the strong constraints with a weaker one, $\sum_{i,\mu} \mathbf{S}^2_{i,\mu} = NS^2$, or, equivalently, by satisfying $\sum_{\mathbf{k},\mu} \mathbf{S}_{\mathbf{k},\mu} \cdot \mathbf{S}_{-\mathbf{k},\mu} = S^2$. If we can find a minimum under the weak constraint that also satisfies the strong constraints, then the obtained solution is the true spin configuration which minimizes the classical energy, and the problem is solved.

However, one needs to remember that, essentially, the LT method corresponds to minimizing the classical energy over a restricted ansatz of the states characterized a single $\mathbf{Q}$-wavevector. It does not include inhomogeneous states characterized by non-linear modulations of magnetic structure such as multiple-$\mathbf{Q}$ incommesurate spirals [113] or higher dimensional generalizations such as, e.g., Z_2 vortex crystals [114, 115] or skyrmion lattices [129], which often appear in highly anisotropic models realized in correlated systems with strong SOC [7, 104, 106]. The model (eq. 4.1) allows for realization of both homogeneous and inhomogeneous states in the phase diagram, and therefore we know a priori that the LT analysis will not be sufficient. However, as a first step, it can give us some qualitative insights about possible classical states realized in the classical phase diagram of eq. 4.1.

After diagonalization of Eq. 4.3, we can rewrite the classical energy (Eq. 4.5) as

$$\epsilon = \frac{1}{N_{uc}} \sum_{\mathbf{k},\eta} \lambda_{\mathbf{k},\eta} S^2, \tag{4.7}$$

where $\lambda_{\mathbf{k},\eta}$ is the η-th eigenvalue with η running from 1 to 48. For each $\mathbf{k}$ point we search for a minimum eigenvalue from the 48 components of the λ-vector and then find the minimum among all $\mathbf{k}$ points of the BZ, which we call $\lambda_{\min} \equiv \lambda_{\mathbf{Q}}$. To construct the ground state spin configuration, we express all the spins of the systems in terms of eigenvectors of $H(\mathbf{k})$ corresponding to the minimum eigenvalue $\lambda_{\mathbf{Q}}$ as

$$\mathbf{S}_{i,\mu} = \sum_{\kappa=1}^{48} c_{\mathbf{Q},\kappa} \mathbf{V}_{\mathbf{Q},\kappa}, \tag{4.8}$$

where $\mathbf{V}_{\mathbf{Q}}$ is a 48 entry column vector. The eigenvector $\mathbf{V}_{\mathbf{Q}}$ satisfies the soft constraint, that is $|\mathbf{V}_{\mathbf{Q}}|^2 = S^2$. If the eigenvectors' entries satisfy the spin length constraint, $S^2_{i,\mu} = (S^x_{i,\mu})^2 + (S^y_{i,\mu})^2 + (S^z_{i,\mu})^2 = S^2 \ \forall(i)$, we say that the state found satisfies the hard constraint.

The results of the classical analysis are presented in Fig. 4.2 which shows the magnitude of the ordering wavevector $\mathbf{Q}$ as a function of r and $\phi \in [\frac{3\pi}{2}, 2\pi]$. Our findings are very similar to the ones reported in Ref. [40]. There are three distinct phases corresponding to this set of parameters. The largest part of the phase diagram (light blue) is the $\mathbf{Q} = (0, 0, 0)$ phase. The other two phases are incommensurate spirals, IC_a and IC_b. We note that the LT method fails to satisfy the hard-constraint in most of the phase diagram, and in particular in the entire regions of IC_a and IC_b phases.

IC_a-phase (mostly orange) is an incommensurate spiral with $\mathbf{Q} = (h, 0, 0)$ running along the a orthorhombic axis. The magnitude of h is very close to $\frac{2}{3}$ for values ϕ close to $\frac{3\pi}{2}$ and does not strongly depend on r. Inside the region bounded by the black line, the lowest LT energy is lower for the commensurate wavevector $\mathbf{Q} = (\frac{2}{3}, 0, 0)$ than for other nearby commensurate wave vectors such as $(\frac{5}{8}, 0, 0)$ or $(\frac{7}{10}, 0, 0)$. The red line, those origin we will discuss later, separates two qualitatively different states in this region. One corresponds to the dominant Kitaev interaction and another to the dominant Γ-interaction. Outside of the region enclosed by the black line, the magnitude of h slowly decreases with increasing ϕ and reaches zero in the boundary with the $\mathbf{Q} = (0, 0, 0)$ phase.

The small bluish purple region, IC_b-phase, is an incommensurate spiral with $\mathbf{Q} \approx (0, k, 0)$ running along the b orthorhombic axis. The magnitude of k is found to be close to $\frac{1}{3}$, but we are not interested in this phase since it doesn't correspond to the experimentally observed magnetic order.

4.4 Classical Ground State From the Relaxation Dynamics Simulations

Another efficient approach to obtain the classical magnetic ground state is by using overdamped dynamics simulations based on the Landau-Lifshitz-Gilbert (LLG) equations [127, 128, 130, 131]. Since the LT solution obtained in the previous section already provides a close approximation to the true ground state, such relaxation simulations initiated from the LT state can potentially bring the system to the desired magnetic order.

The LLG equation can be written in the following form:

$$\frac{\partial \mathbf{S}_{i,\mu}}{\partial t} = \mathbf{S}_{i,\mu} \times (\mathbf{h}_{i,\mu} + \frac{\alpha_G}{S} \frac{\partial \mathbf{S}_{i,\mu}}{\partial t}), \tag{4.9}$$

where $\mathbf{h_{i},_{\mu}}$ is the effective exchange field and α_G is a dimensionless damping parameter. The components of the effective exchange field can be easily defined from Eq. 4.6 as

$$h^{\alpha}_{i,\mu} = \frac{\partial H}{\partial S^{\alpha}_{i,\mu}} = \sum_{j,\nu} \sum_{\beta} H^{\alpha\beta}_{i\mu,j\nu} S^{\beta}_{j,\nu}, \tag{4.10}$$

We integrate the LLG equation numerically by adopting the finite-difference method introduced by Serpico *et al* [127]. The technical details of the numerical method can be found in Refs. [127] and [131].

Here we present the results of the dynamics simulation for two characteristic points of the incommensurate IC_a state: the point P_K at $r = \frac{3\pi}{8}$ and $\phi = \frac{25\pi}{16}$ corresponding to the dominant Kitaev interaction, and the point P_Γ at $r = \frac{\pi}{8}$ and $\phi = \frac{97\pi}{64}$, corresponding to the dominant Γ interaction. In our simulations we used a cluster of $240 \times 2 \times 2$ orthorhombic unit cells for both P_K and P_Γ, with N=15360 spins. Periodic boundary conditions were used in all simulations.

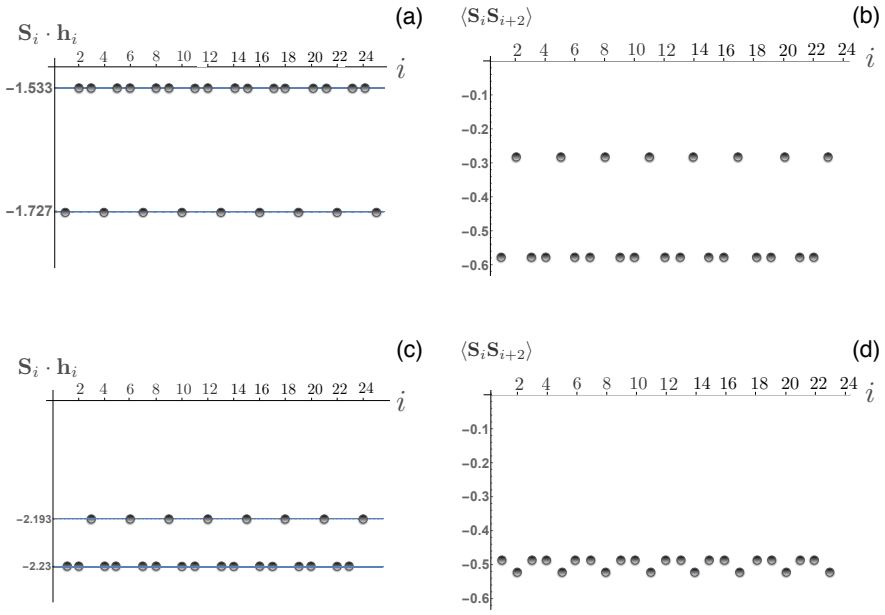

Figure 4.3: (a) and (c): Solid lines correspond to the two values of the local energies, $\mathbf{S}_i \cdot \mathbf{h}_i$, obtained at P_K point and at P_Γ points, respectively. Circles show the distribution of the local energies along the odd (even) sites of a zigzag chain. (b) and (d) show the distribution of the spin-spin correlation functions between the odd (even) spins of a zigzag chain. All results are obtained from the non-linear LLG simulation initialized from the commensurate $\mathbf{Q} = \frac{2}{3}\mathbf{b_1}$ state.

4.4.1 K-Dominant State

We first discuss our findings at the P_K point. The LT wavevector that minimizes the classical energy (4.7) is $\mathbf{Q}_K \simeq 0.675\,\mathbf{b_1}$. The corresponding eigenvalue is $E_{\rm LT}(\mathbf{Q}_K) \simeq -1.58845$. Using the LT result, we construct the initial state for the non-linear LLG simulations by requiring that all spins point along the directions determined by the eigenvector $\mathbf{V}_{\mathbf{Q}_K}$ and have unit length. The energy per site in the spin configuration resulting from this simulation is found to be equal to $E_{\rm LLG} \simeq -1.577718 > E_{\rm LT}(\mathbf{Q}_K)$. The difference in energy is only 0.6 percent. However, this LLG-state does not seem to be close enough to the true classical ground state since despite having most of the local torques being very small, $\mathbf{S}_i \times \mathbf{h}_i \simeq 10^{-7}$, some of the local torques are an order

of magnitude larger, and we see many different environments for the local fields and torques.

In order to check whether there are any other close by local minima states, we perform another LLG simulation initialized from the commensurate $\mathbf{Q} = \frac{2}{3}\,\mathbf{b_1} \approx 0.667\,\mathbf{b_1}$ state. In this case, the LLG simulation gives the state with an energy per site equal to $E_{\rm LLG} = -1.578237$, which is only slightly lower than the energy obtained in the LLG simulation initiated from the LT state. However, this new LLG state finds the local torques to be numerically small (of order 10^{-7}).

In Fig. 4.3(a) we plot the distribution of local energies, $\mathbf{S}_i \cdot \mathbf{h}_i$, in the state resulting from the LLG simulation for all the sites of lattice. We see that local energies, instead of being randomly distributed in the vicinity of the local minimum, take only two values approximately equal to -1.499 and -1.737. This suggests that there are two different local fields acting on the spins and, thus, two different kinds of sites. In Fig. 4.3 (b) we plot the distribution of local energies on even sites of a single zigzag chain (either xy- or $x'y'$-chains in Fig. 4.1). We see that the magnitude of the local fields alternates between these two values: -1.499 for the "minority" spins (1/3 of total number of spins on the half zigzag chain) and -1.533 for the "majority" spins (2/3 of total number of spins on the half zigzag chain). We have checked that the same behavior is observed along all 4 zigzag chains of the orthorhombic unit cell for both even and odd sites. In Fig. 4.3(c) we plot the spin-spin correlation function between even (odd) spins along the zigzag chain. Here, we also see that the spin-spin correlation function is non-uniform and alternates between two different values with the same periodicity 3.

These findings clearly show that the state obtained in the LLG simulation has periodicity 3. Moreover, it is not a "simple" counter-rotating spiral described by $+\mathbf{Q}$ on even and $-\mathbf{Q}$ on odd sites; for a counter-rotating spiral, the dot product of each pair of spins on even (odd) sites should be equal to the same constant given by the pitch of the spiral, and we do not have this.

Let us further analyze this "period 3"- state with "majority" and "minority" spins. By inspection we find that if the spin on a site n has components $\mathbf{S}_n = [x_1, y_1, z_1]$ then the right and left second neighbors have components $\mathbf{S}_{n+2} = [-y_1, -x_1, z_1]$ and $\mathbf{S}_{n-2} = [-x_2, x_2, -z_2]$, respectively. The spin components satisfy the following relations: $x_1 \neq x_2$, $y_1 \neq y_2$, $z_1 \neq z_2$ and $|x_2| = |y_2|$. All spins are given in the form $\mathbf{S} = [S^x, S^y, S^z]$,

where x, y and z axes are shown in Fig.1. Notice that two "majority" spins of the "period 3"- state have the same S^z component, i.e. $\mathbf{S}_n$ and $\mathbf{S}_{n+2}$, and the spin belonging to the "minority" spins is $\mathbf{S}_{n-2}$. This can be seen in Fig. 4.4(a) where we also denoted the "majority" spins as **A** and **B**, and the "minority" spins as **C**.

The spin structure of the magnetic unit cell is explicitly given in the technical details at the end of the chapter (section 4.7, also see Fig. 4.8). The local field (Eq. 4.10) acting on each spin can now be computed by using only five parameters, namely x_1, y_1, z_1 for the "majority" spins and x_2, z_2 for the "minority" spins. We find:

$$\begin{aligned}
\mathbf{h}_n^{\text{maj}} &= \Big(J\left(x_1 - x_2 + y_1\right) + Kx_1 + \Gamma\left(x_1 + z_2\right), J\left(x_1 + x_2 + y_1\right) + Kx_2 + \Gamma\left(y_1 + z_1\right), \\
&\quad J\left(2z_1 - z_2\right) + Kz_1 + \Gamma\left(x_2 + y_1\right)\Big) \\
\mathbf{h}_{n+2}^{\text{maj}} &= \Big(-J\left(x_1 + x_2 + y_1\right) - Kx_2 + \Gamma\left(y_1 + z_1\right), \\
&\quad -J\left(x_1 - x_2 + y_1\right) - Kx_1 - \Gamma\left(x_1 + z_2\right), J\left(2z_1 - z_2\right) + Kz_1 + \Gamma\left(x_2 + y_1\right)\Big) \\
\mathbf{h}_{n-2}^{\text{min}} &= \Big(J\left(x_1 + x_2 - y_1\right) - Ky_1 - \Gamma\left(x_2 + z_1\right), -J\left(x_1 + x_2 - y_1\right) + Ky_1 + \Gamma\left(x_2 + z_1\right), \\
&\quad J\left(2z_1 - z_2\right) - Kz_2 - 2\Gamma x_1\Big)
\end{aligned} \tag{4.11}$$

We can solve Eq. 4.11 for x_1, y_1, z_1, x_2 and z_2 by minimizing the energy per site, $E_{\text{site}} = \frac{1}{3}\sum_{i=1}^{3} \mathbf{S}_i \cdot \mathbf{h}_i$. We use this solution to explicitly compute the spin's components along the zigzag chain, which we plot in Fig. 4.4(a). Now the spin structure is completely clear. In order to maximize energy gain due to the dominant ferromagnetic Kitaev interaction, every third bond is ferromagnetic (highlighted in yellow in the bottom of Fig. 4.4(a). We also note that since the components of any NN spins connected by a z-bond are related as $[x, y, z] \to [y, x, z]$, both the Γ and the Kitaev interaction are satisfied on all z-bonds.

4.4.2 Γ-Dominant State

The analysis at the P_Γ ($r = \pi/8$ and $\phi = 97\pi/64$) with dominant Γ interaction goes along the same line. Again we found that the non-linear LLG simulations starting from the initial incommensurate state determined by the LT method does not find the

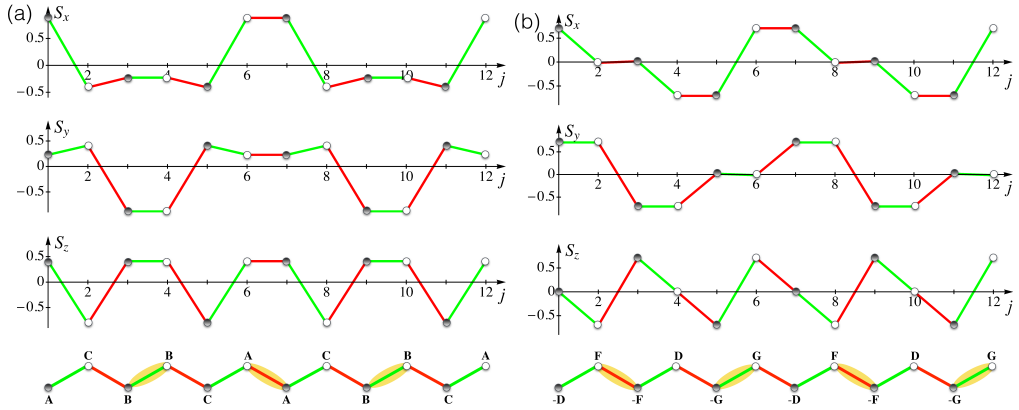

Figure 4.4: The modulation of S^x, S^y and S^z spin components along a single zigzag chain computed at (a) P_K and (b) P_Γ points. Thin red and green lines are shown only as guide to eyes. The bottom figures show the chain configuration with the white and gray circles representing spins on the top and bottom halves of the zigzag chain, respectively. The green and red lines denote the x and y bonds. While at the K-dominant state, every third bond is ferromagnetic (shown as a filled oval), at the Γ-dominant state, every third bond is antiferromagnetic (shown as an open oval).

magnetic configuration which is close to the true ground state. The local torques in the obtained state are not uniform, and larger than those of the LLG simulation initialized from the commensurate $\mathbf{Q} = \frac{2}{3}\,\mathbf{b_1}$ state. Again, we find that when we initialize our LLG simulation with the $\mathbf{Q} = \frac{2}{3}\,\mathbf{b_1}$, we find a "period 3"- state. The local energies and spin-spin correlation functions between the even(odd) sites on the zigzag chain computed from this state are shown in Figs. 4.3 (d)-(f)). We see that, compared to the K-dominant state, the local fields acting on the "minority" and the "majority" spin are much closer; -2.193 and -2.230, respectively. Also, for the Γ-dominant state the local fields acting on the majority spins are more negative, whereas for the K-dominant state the local fields acting on the minority spins are more negative.

We find that in the Γ-dominant state all spins in the unit cell can be described by only four parameters, x_3, y_3, z_3, and x_4 parameters (here, $y_4 = x_4$ and z_4=0). However, a close inspection shows that the relations between the spin's components are different from those of the K-dominant state. We find that if the spin of the zigzag chain on the site n has components $\mathbf{S}_n = (x_3, -y_3, z_3)$, then one of its NNN spin has components

$\mathbf{S}_{n+2} = (-y_3, x_3, -z_3)$, and another NNN spin has components $\mathbf{S}_{n-2} = (-x_4, x_4, 0)$. Similar to the K-dominant state, these spins correspond to **G**, **F**, and **D** respectively (Fig. 4.4, see section 4.7 and Fig. 4.8 for additional details). This lead to the following expressions of local fields acting on majority and minority spins:

$$\begin{aligned}
\mathbf{h}_n^{\rm maj} &= \Big(-J(x_3 - x_4 + y_3) + Kx_4 + \Gamma(x_3 + z_3), J(x_3 + x_4 + y_3) + Ky_3 - Gy_3, \\
&\quad Kz_3 + G(x_3 + x_4)\Big) \\
\mathbf{h}_{n+2}^{\rm min} &= \Big(J(x_3 + x_4 + y_3) + Ky_3 - \Gamma y_3, -J(x_3 - x_4 + y_3) + Kx_4 + \Gamma(x_3 + z_3), \\
&\quad -Kz_3 - \Gamma(x_3 + x_4)\Big) \\
\mathbf{h}_{n-2}^{\rm maj} &= \Big(-J(x_3 + x_4 - y_3) - Ky_3 - \Gamma(x_4 + z_3), \\
&\quad -J(x_3 + x_4 - y_3) - Kx_3 - \Gamma(x_4 + z_3), 0\Big)
\end{aligned} \tag{4.12}$$

The minimization of the energy with these local fields (eq. 4.12) gives a solution shown in Fig. 4.4(b). We see that in the Γ-dominant state every third bond is antiferromagnetic with spins laying almost entirely either in the xz or in the yz plane with spins pointing along the corresponding diagonals. This ordering maximize the energy gain due to the dominant Γ interaction.

Finally, we would like to check what controls the angles between the "majority" spins, θ_{AB}, and between the "majority" and the "minority" spins, $\theta_{AC} = \theta_{BC}$. In Fig. 4.5 we plot these angles along a single zigzag chain as a function of r representing the strength of the Γ interaction for two different values of ϕ controlling the relative strength of the Kitaev and Heisenberg interactions: (a) $\phi = \frac{97\pi}{64}$ and (b) $\phi = \frac{25\pi}{16}$. The angles θ_{AB} and $\theta_{AC} = \theta_{BC}$ are shown by red and blue lines, respectively.

We see that at small $r \gtrsim 0$ corresponding to a dominant Γ-interaction and for both values of ϕ all three angles, θ_{AB} and $\theta_{AC} = \theta_{BC}$, are almost equal to 120° degrees. The deviation from 120° degrees is particularly small for $\phi = \frac{97\pi}{64}$ and it only slightly increases for the larger $\phi = \frac{25\pi}{16}$. Thus, at this parameter range the magnetic ground state can be very closely described by a collection of zigzags in which each half of the chain is in almost a 120° coplanar spiral laying in the (1,-1,1) plane. Spins on the odd and even sites rotates in opposite direction.

With increasing r (decreasing Γ), the deviation from this simple spiral state increases. At the boundary to the K-dominant state all three angles, θ_{AB}, θ_{AC} and

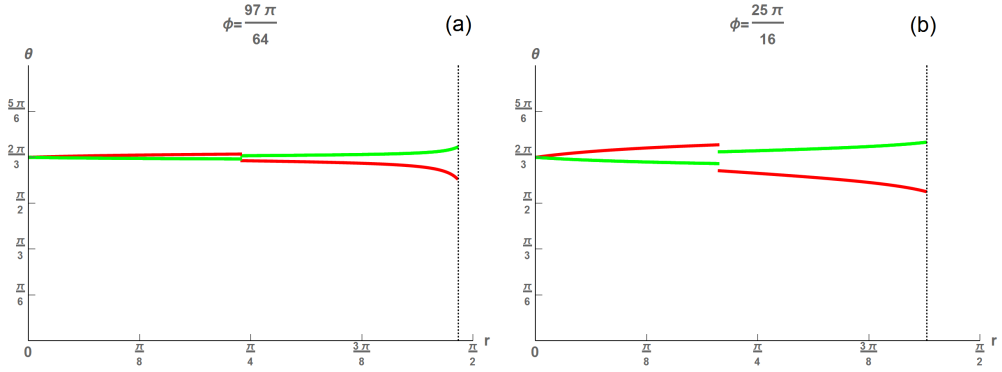

Figure 4.5: Red and blue solid lines correspondingly show the dependence on the parameter r of the angles between "majority" spins and between the "majority" and "minority" spins belonging to the same zigzag chain. (a) $\phi = \frac{97\pi}{64} \simeq 1.516$, (b) $\phi = \frac{25\pi}{16} \simeq 1.563$. The discontinuity in the angles occurs at the point of phase transition between the Γ-dominant and K-dominant states. This indicates a first-order phase transition. The dashed black vertical line indicates when the system enters the IC_b phase.

θ_{BC}, exhibit a discontinuous jump. This discontinuity indicates that the transition between the Γ-dominant and K-dominant states is a first-order phase transition. Interestingly, the dependences of $\theta_{AB}(r)$ and $\theta_{AC}(r)$ are opposite in the Γ-dominant and the K-dominant states. In the Γ-dominant state, while θ_{AB} is larger than $2\pi/3$ and increasing, θ_{AC} is smaller than $2\pi/3$ and decreasing. The situation is reversed in the K-dominant state. For large r, the system undergoes a first-order transitions into the IC_b phase; this point of this transition is shown by the vertical black dashed line. This phase is discussed in Ref. [40].

4.4.3 Symmetry Analysis

In order to compare the obtained magnetic structure with the experimentally observed magnetic order, we follow the symmetry analysis performed by Biffin *et al* [9]. A natural way to describe the magnetic structure is through the language of the basis vectors which contain symmetry-imposed relations between the Fourier components of the magnetic structure between the various sites in the primitive unit cell. The details of the analysis are given in section 4.7.

For both the K- and the Γ-dominant states we found that non-zero Fourier components of the magnetic structure are given by

$$\mathbf{M}_{(2/3,0,0)} = (iM_aA,\, iM_bC,\, M_cF), \tag{4.13}$$

which is the Γ_4 irreducible representation, and

$$\mathbf{M}_{(4/3,0,0)} = (-iM_aA,\, -iM_bF,\, M_cC), \tag{4.14}$$

which is the Γ_3 irreducible representation. In Eqs. 4.13 and 4.14,
$\mathbf{M}_{\mathbf{q}}^T = (\mathbf{M}_{\mathbf{q},1}, \mathbf{M}_{\mathbf{q},2}, \mathbf{M}_{\mathbf{q},3}, \mathbf{M}_{\mathbf{q},4})$ is a four-component vector and $\mathbf{M}_{\mathbf{q},n}$ denote the Fourier components of the magnetic moments at the four sites $n = 1, ..4$ in the primitive cell. M_a, M_b, and M_c are the components of the sublattice magnetization along orthorhombic a, b and c axes. If we normalize $M_c = 1$, we find that for the K-dominant state, the ratios of the components computed at P_K point for $\mathbf{q} = (2/3, 0, 0)$ is $M_a : M_b : M_c = 0.77 : 0.90 : 1$ and for $\mathbf{q} = (4/3, 0, 0)$ is again $M_a : M_b : M_c = 0.77 : 0.90 : 1$. For the the Γ-dominant state, the ratio of the components computed at P_Γ point for $\mathbf{q} = (2/3, 0, 0)$ is $M_a : M_b : M_c = 0.59 : 0.82 : 1$ and for $\mathbf{q} = (4/3, 0, 0)$ is again the same $M_a : M_b : M_c = 0.59 : 0.82 : 1$.

Our result that $\mathbf{M}_{(2/3,0,0)}$ follows the Γ_4 representation is in line with Ref. [9], as are the relative complex phases between the different components of Eq. 4.13 and the relative amplitudes $M_a < M_b < M_c$. As Biffin *et al.* worked under the assumption of a single $\mathbf{Q}$ state, they do not discuss $\mathbf{M}_{(4/3,0,0)}$, but we note that our static structure factor had the largest spectral weight from at $\mathbf{Q} = \frac{2}{3}\mathbf{b}_1$.

4.5 Spin Wave Excitations

As discussed in the previous section, the "period 3"- states cannot be modeled as a single-$\mathbf{Q}$ spirals or even as a more complicated $+\mathbf{Q}/-\mathbf{Q}$ state if we consider the orthorhombic unit cell. However, our periodicity-3 state is commensurate if we use an enlarged magnetic unit cell composed of three orthorhombic unit cells along the $\mathbf{a}_1$ axis. In this case, the magnetic unit cell contains 48 sites. The corresponding magnetic Brillouin zone together with the high-symmetry paths is shown in the inset of Fig. 4.6(b). Enlarging the unit cell allows us to study the magnetic excitations in the

periodicity-3 magnetic ground state by employing the semiclassical analysis. Here, we confine ourselves to the linear spin-wave (LSW) consideration.

4.5.1 Linear Spin Wave Spectra

We start by aligning the local $\tilde{z}_{i,\mu}$-axis on each site along the direction of the ordered moment, which can be done by a local transformation

$$\begin{aligned} S^a_{i,\mu} &= \cos\theta_i \cos\varphi_{i,\mu}\, S^{\tilde{x}}_{i,\mu} - \sin\varphi_{i,\mu}, S^{\tilde{y}}_{i,\mu} + \sin\theta_{i,\mu}\cos\varphi_{i,\mu}\, S^{\tilde{z}}_{i,\mu}, \\ S^b_{i,\mu} &= \cos\theta_{i,\mu}\sin\varphi_{i,\mu}\, S^{\tilde{x}}_{i,\mu} + \cos\varphi_{i,\mu}\, S^{\tilde{y}}_{i,\mu} + \sin\theta_{i,\mu}\sin\varphi_{i,\mu}\, S^{\tilde{z}}_{i,\mu}, \\ S^c_{i,\mu} &= -\sin\theta_{i,\mu}\, S^{\tilde{x}}_{i,\mu} + \cos\theta_{i,\mu}, S^{\tilde{z}}_{i,\mu}, \end{aligned} \tag{4.15}$$

or in a short notation $S^{\alpha}_{i,\mu} = \mathcal{R}_{\alpha\beta}(\theta_{i,\mu}, \varphi_{i,\mu}) S^{\tilde{\beta}}_{i,\mu} i$. In the enlarged unit cell $\mu = 1, ...48$. Note that by the laboratory reference frame we assume the orthorhombic frame, so the spin components are $\alpha = a, b, c$.

Using the local spin basis, we perform usual Holstein-Primakoff expansion:

$$\begin{aligned} S^{\tilde{x}}_{i,\mu} &= \sqrt{\frac{S}{2}}(a_{i,\mu} + a^{\dagger}_{i,\mu}), \\ S^{\tilde{y}}_{i,\mu} &= -i\sqrt{\frac{S}{2}}(a_{i,\mu} - a^{\dagger}_{i,\mu}), \\ S^{\tilde{z}}_{i,\mu} &= S - a^{\dagger}_{i,\mu} a_{i,\mu}. \end{aligned} \tag{4.16}$$

By the Fourier transform,

$$a_{i,\mu} = \sqrt{\frac{1}{N_m}} \sum_{\mathbf{q}} e^{i\mathbf{q}\mathbf{R_i}} \tag{4.17}$$

where N_m is the number of magnetic unit cells and $\mathbf{q}$ is defined in the magnetic Brillouin zone shown in Fig.6 (c), we get the quadratic Hamiltonian which in the matrix form can be written as

$$H_2 = E_2 + \frac{S}{2} \sum_{\mathbf{q}} x^{\dagger}_{\mathbf{q}} H_{\mathbf{q}} x_{\mathbf{q}} \tag{4.18}$$

where the interaction matrix is given by

$$H_{\mathbf{q}} = \begin{pmatrix} Q_{\mathbf{q}} & R_{\mathbf{q}} \\ R^*_{-\mathbf{q}} & Q^*_{-\mathbf{q}} \end{pmatrix} \tag{4.19}$$

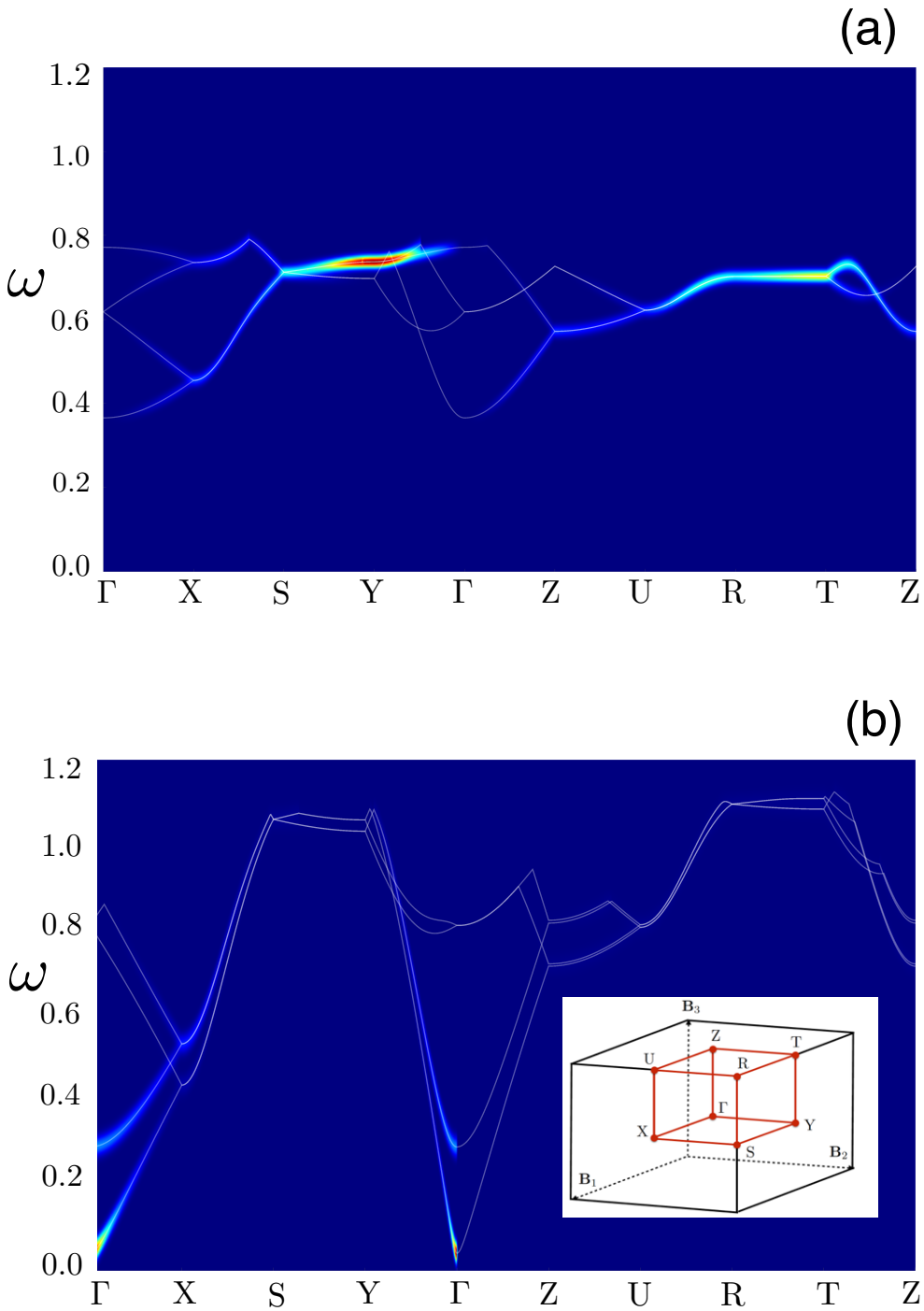

Figure 4.6: The intensity plot of the dynamical structure factor computed at (a) P_K and (b)P_Γ points. The LSW spectra are shown by white solid lines along the high-symmetry paths. Only four lowest branches are shown. Inset of (b): the magnetic Brillouin zone together and the high-symmetry paths.

$x_{\mathbf{q}} = (a_{1,\mathbf{q}}, ..., a_{48,\mathbf{q}}, a^{\dagger}_{1,-\mathbf{q}}, ..., a^{\dagger}_{48,-\mathbf{q}})^T$ and $E_2 = \frac{S}{2}\sum_{\mathbf{q},i}(-Q_{ii_{\mathbf{q}}} + \Omega_{i_{\mathbf{q}}})$, where $Q_{ii_{\mathbf{q}}}$ are the diagonal components of $Q_{\mathbf{q}}$ and $\Omega_{\mathbf{q}}$ is defined further down in Eq. 4.24.

To diagonalize the Hamiltonian (Eq. 4.18), we introduce the transformation

$$x_{\mathbf{q}} = \mathcal{T}_{\mathbf{q}} y_{\mathbf{q}}, \tag{4.20}$$

where vector $y_{\mathbf{q}} = (b_{1,\mathbf{q}}, ..., b_{48,\mathbf{q}}, b^{\dagger}_{1,-\mathbf{q}}, ..., b^{\dagger}_{48,-\mathbf{q}})^T$ represents the vector of Bogoluibov quasiparticles and $\mathcal{T}_{\mathbf{q}}$ is the transformation matrix. In order to preserve the bosonic commutation relations, $\mathcal{T}_{\mathbf{q}}$ must satisfy $\mathcal{T}^{\dagger}_{\mathbf{q}}\eta\mathcal{T}_{\mathbf{q}} = \eta$, where

$$\eta = \begin{pmatrix} I & 0 \\ 0 & -I \end{pmatrix}. \tag{4.21}$$

We construct the transformation matrix $\mathcal{T}_{\mathbf{q}}$ numerically using the eigenvectors of the matrix $\eta H_{\mathbf{q}}$, and get

$$\mathcal{T}_{\mathbf{q}} = \begin{pmatrix} U_{\mathbf{q}} & V^{*}_{-\mathbf{q}} \\ V_{\mathbf{q}} & U^{*}_{-\mathbf{q}} \end{pmatrix}. \tag{4.22}$$

Using Eqs. 4.20 through 4.22, the Bogoliubov transformation can be written in a familiar form:

$$\begin{aligned} a_{\mu,\mathbf{q}} &= U_{\mu\nu,\mathbf{q}} b_{\nu,\mathbf{q}} + V^{*}_{\mu\nu,-\mathbf{q}} b^{\dagger}_{\nu,-\mathbf{q}} \\ a^{\dagger}_{\mu,-\mathbf{q}} &= U^{*}_{\mu\nu,-\mathbf{q}} b^{\dagger}_{\nu,-\mathbf{q}} + V_{\mu\nu,\mathbf{q}} b_{\nu,\mathbf{q}}. \end{aligned} \tag{4.23}$$

After diagonalization we get

$$H_2 = \frac{S}{2}\sum_{\mathbf{q}} y^{\dagger}_{\mathbf{q}} \Omega_{\mathbf{q}} y_{\mathbf{q}}, \tag{4.24}$$

where $\Omega_{\mathbf{q}} = \mathcal{T}^{\dagger}_{\mathbf{q}} H_{\mathbf{q}} \mathcal{T}_{\mathbf{q}}$ and is equal to

$$\Omega_{\mathbf{q}} = \begin{pmatrix} \omega_{\mathbf{q}} & 0 \\ 0 & -\omega_{\mathbf{q}} \end{pmatrix}, \tag{4.25}$$

with $\omega_{\mathbf{q}} = \mathrm{diag}[\omega_{1,\mathbf{q}}, \omega_{2,\mathbf{q}}, ..., \omega_{48,\mathbf{q}}]$ being a diagonal 48×48 matrix.

The LSW spectra computed at the P_K and P_Γ points are shown by white solid lines in Fig. 4.6 (a) and (b), respectively. From the forty eight magnon branches, we only show the lowest four. As expected, we find that LSW spectra are gapped. This is due

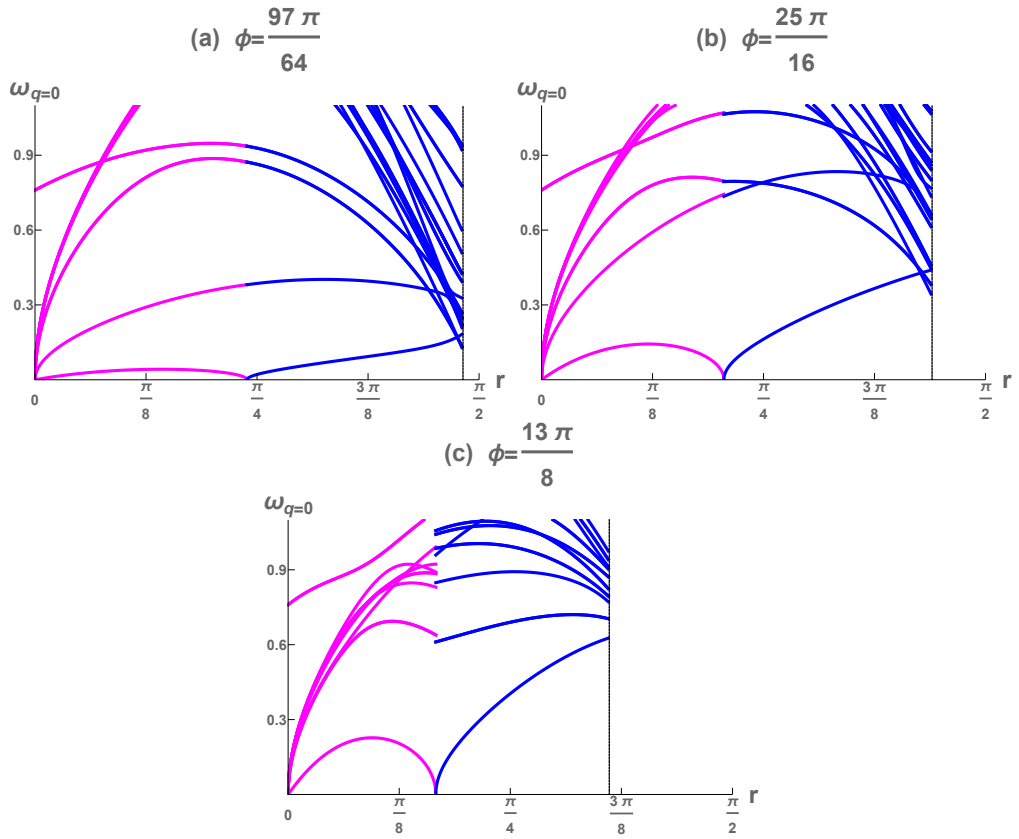

Figure 4.7: The $\mathbf{q} = 0$ low energy branches of the spin wave spectrum $\omega_{\mathbf{q}=0}$ as a function of the parameter r, for (a) $\phi = \frac{97\pi}{16}$, (b) $\phi = \frac{25\pi}{16}$, and (c) $\phi = \frac{13\pi}{8}$. For small r the system exists in the Γ-dominant state (purple). At some point $r < \frac{\pi}{4}$, the system undergoes a first-order phase transition to the K-dominant state (blue). The lowest branch of the spectrum becomes gapless ($\Delta = 0$) at this point. The discrepancy between the first-order phase transistion and $\Delta = 0$ is discussed in section 4.7.3. For large r, the system transitions into the IC_b phase; the point where this happens is shown by black vertical line.

to the anisotropic K and Γ interactions in Eq. 4.1. In the enlarged magnetic BZ, the lowest pseudo-Goldstone mode has a minimum, Δ, at the $\Gamma = (0, 0, 0)$ point (we refer to this point in the BZ as $\mathbf{q} = 0$ below for convenience).

In Fig. 4.7(a)(b)(c) we plot the $\mathbf{q} = 0$ low energy branches of the spin wave spectra, $\omega_{\mathbf{q}=0}$, as a function of the parameter r for three different values of ϕ: (a) $\phi = \frac{97\pi}{64}$, (b) $\phi = \frac{25\pi}{16}$, and (c) $\phi = \frac{13\pi}{8}$. For small r, the system exists in the Γ-dominant state, shown in purple. At some point ($r < \frac{\pi}{4}$), the system undergoes a first-order phase transition into the K-dominant state, shown in blue.

We can find the dependence on the gap parameter Δ on r and ϕ from examining the lowest branch of $\omega_{\mathbf{q}=0}$ in each panel of Fig. 4.7. When $\Delta = 0$ (for example, at $r = 0$), the spectrum is said to be "gapless"–it costs nothing to make excitations. When $r = 0$, $\Gamma = 1$ and $J = K = 0$, the model is highly degenerate, and multiple branches are gapless. The physics at this point of the phase diagram is discussed in reference [121], and they find that the many gapless modes are an artifact of calculating spin waves only to linear order. In the vicinity of $r = 0$, we would expect non-linear spin waves, which we did not calculate here, to create a gap ($\Delta \neq 0$).

In Fig. 4.7 (a)-(c), we also see that $\Delta = 0$ at the point of the first-order phase transition between the Γ and K dominant states. We note that generically, the spin-wave spectrum has a gap and is discontinuous at a first-order phase transistion. We reconcile the gapless spectrum with the first order phase transition in section 4.7.3. We find that at the point of transition, there exists an "accidental" SO(2) symmetry, causing the softening of the spectrum. We expect that if we were to calculate non-linear spin waves (similar to our work in chapter 2), the "accidental zero" would be lifted. The spectrum would become gapped and discontinuous at the point of the first-order phase transistion.

We note that there is a discontinuity in the higher branches of the LSW spectra at the point of phase transition, also indicative of a first-order phase transition between the two states. The discontinuity is larger for larger ϕ values (larger J). This is consistent with the larger discontinuity in our angle data in Fig. 4.5(b) when compared to Fig. 4.5(a). We attribute the much smaller discontinuity in Fig. 4.5(a) to how near the P_Γ point is to the highly symmetric point $\phi = \frac{3\pi}{2}$, $r = \frac{\pi}{4}$, where $J = 0$, and $K = \Gamma = \frac{1}{\sqrt{2}}$.

Finally, we note that as we continue to increase r, the system undergoes another first-order phase transition to the IC_b state; the point where this happens is shown by the black vertical line.

4.5.2 Dynamical Spin-Spin Structure Factor

Next, we evaluate the diagonal components of the dynamical structure factor $\mathcal{S}(\mathbf{q},\omega)$, the quantity directly observed in the inelastic neutron scattering experiments. It is convenient to express the dynamic structure factor using the laboratory reference frame in which it takes the following form:

$$\mathcal{S}^{\alpha\beta}(\mathbf{q},\omega) = \int \frac{dt}{2\pi} e^{i\omega t} \langle S^{\alpha}(\mathbf{q},t) S^{\beta}(\mathbf{q},0)\rangle. \tag{4.26}$$

Using the fluctuation dissipation theorem, we get

$$S^{\alpha\beta}(\mathbf{q},\omega) = -\frac{1}{\pi}[1+n_B(\omega)]\mathrm{Im}[G^{\alpha\beta}(\mathbf{q},\omega)], \tag{4.27}$$

where n_B is the Bose distribution function and $G^{\alpha\alpha}(\mathbf{q},\omega)$ is the retarded Green's function

$$G^{\alpha\beta}(\mathbf{q},\omega) = \sum_{\mu,\mu',\nu} \frac{\langle 0|S^{\alpha}_{\mu',\mathbf{q}}|\nu\rangle\langle\nu|S^{\beta}_{\mu,-\mathbf{q}}|0\rangle}{\omega-\omega_{\nu,\mathbf{q}}+i\epsilon}. \tag{4.28}$$

At zero temperature, the structure factor reduces to $S^{\alpha\beta}(\mathbf{q},\omega) = -\frac{1}{\pi}\mathrm{Im}[G^{\alpha\beta}(\mathbf{q},\omega)]$.

In order to compute the Green's function (Eq. 4.28), we transform the spins components to the local reference frame using Eq. 4.16 and get

$$G^{\alpha\beta}(\mathbf{q},\omega) = \sum_{\mu,\mu',\nu} F^{\alpha\tilde{\alpha}}_{\mu'} F^{\beta\tilde{\alpha}}_{\mu} \frac{\langle 0|S^{\tilde{\alpha}}_{\mu',\mathbf{q}}|\nu\rangle\langle\nu|S^{\tilde{\beta}}_{\mu,-\mathbf{q}}|0\rangle}{\omega-\omega_{\nu,\mathbf{q}}+i\epsilon}, \tag{4.29}$$

where $F^{\alpha\tilde{\alpha}}_{\mu}$ are some functions of the angles of local rotation θ_μ and φ_μ on the sublattice μ. Note that the in the local frame, only the transverse terms $S^{\tilde{x}\tilde{x}}, S^{\tilde{y}\tilde{y}}, S^{\tilde{x}\tilde{y}}$, and $S^{\tilde{y}\tilde{x}}$ contribute to lowest order. Other terms will contribute to the dynamical structure factor only at higher orders which we ignore and in the following will be interested only with the transverse dynamical structure factor.

The matrix elements entering to Eq. 4.29 can be easily computed using Eq. 4.23:

$$\begin{aligned}\langle 0|S^{\tilde{x}}_{\mu,\mathbf{q}}|\nu\rangle &= \sqrt{\frac{S}{2}}(U_{\mu\nu,\mathbf{q}} + V_{\mu\nu,\mathbf{q}}) \\ \langle 0|S^{\tilde{y}}_{\mu,\mathbf{q}}|\nu\rangle &= -i\sqrt{\frac{S}{2}}(U_{\mu\nu,\mathbf{q}} - V_{\mu\nu,\mathbf{q}}).\end{aligned} \tag{4.30}$$

Finally, we note that the scattering intensity (or inelastic neutron scattering cross section), as compared to the dynamic structure factor, requires an additional summation over α and β: Thus, we compute intensity using the following expressions:

$$I(\mathbf{q},\omega) \propto \sum_{\alpha,\beta}(\delta_{\alpha,\beta} - \frac{q_\alpha q_\beta}{q^2})S^{\alpha\beta}(\mathbf{q},\omega) \tag{4.31}$$

where q_α is the component of $\mathbf{q}$ pointing in the α direction. Thus, the inelastic scattering is strongest when the scattering vector $\mathbf{q}$ is along the magnetic moments. In Fig. 4.6 (a) and (b) we present a plot of scattering intensity on top of the the LSW spectrum computed at P_K and P_Γ points, respectively. The colors and the width indicate the magnitude of the intensity after convolving the structure factor with a gaussian of finite width to emulate finite experimental resolution.

4.6 Conclusion and Discussion

In this chapter, we examined the possible ground states of β-Li_2IrO_3. We found that relaxing the hard spin constraint using the Luttinger-Tisza method did not give a ground state with fixed length spins, but was suggestive of a ground state with a propagation vector of $\mathbf{Q} \approx \frac{2}{3}\mathbf{b}_1$. We employed a non-linear numerical method of solving the LLG equation to find possible ground states with fixed spin length, and we found two possible ground states in the region of interest of our parameter space, both "period-3" states. We characterized these states, and then used a Holstein-Primakoff transformation to compute spin waves. We found the spectrum was gapped, except at special points such as when $\Gamma = 1$, J,$K = 0$, or at the point of phase transition between the K-dominant state and the Γ-Dominant state. Finally, we computed the dynamic structure factor, in order to help experimentalists test our predictions.

4.7 Technical Details for Chapter 4

4.7.1 Structure of the Periodicity-3 State

We first consider the K-dominant state. The 48 spins of the magnetic unit cell can be splitted into 6 groups using the A,B,C- notations and the symmetry operation connecting each two chains, such as $\mathbf{A} = [x_1, y_1, z_1]$, $\mathbf{B} = [-y_1, -x_1, z_1]$, $\mathbf{C} = [-x_2, x_2, -z_2]$, $\mathbf{A'} = [y_1, x_1, z_1]$, $\mathbf{B'} = [-x_1, -y_1, z_1]$ and $\mathbf{C'} = [x_2, -x_2, -z_2]$. Then we get

$$\begin{aligned}
\mathbf{A}: &\quad \{18, 19, 26, 27, 38, 39, 46, 47\} \\
\mathbf{A'}: &\quad \{17, 20, 25, 28, 37, 40, 45, 48\} \\
\mathbf{B}: &\quad \{3, 6, 11, 14, 23, 31, 34, 42\} \\
\mathbf{B'}: &\quad \{4, 5, 12, 13, 24, 32, 33, 41\} \\
\mathbf{C}: &\quad \{2, 7, 10, 15, 22, 30, 35, 43\} \\
\mathbf{C'}: &\quad \{1, 8, 9, 16, 21, 29, 36, 44\}
\end{aligned} \tag{4.32}$$

In the Γ-dominant state, the structure is similar but instead of 6 groups the spins are spitted into 10 groups: $\mathbf{G} = [x_3, -y_3, z_3]$, $\mathbf{G'} = [-y_3, x_3, z_3]$, $\mathbf{F} = [-y_3, x_3, -z_3]$, $\mathbf{F'} = [x_3, -y_3, -z_3]$, $\mathbf{D} = [-1, -1, 0]/\sqrt{2}$, where the variables x_3, y_3 and z_3 are positive. We get the following distribution of 48 sites of the magnetic unit cell between the groups:

$$\begin{aligned}
\mathbf{G}: &\quad \{18, 26, 38, 46\} \\
-\mathbf{G}: &\quad \{7, 15, 35, 43\} \\
\mathbf{G'}: &\quad \{17, 25, 37, 45\} \\
-\mathbf{G'}: &\quad \{8, 16, 36, 44\} \\
\mathbf{F}: &\quad \{2, 10, 22, 30\} \\
-\mathbf{F}: &\quad \{3, 11, 23, 31\} \\
\mathbf{F'}: &\quad \{1, 9, 21, 29\} \\
-\mathbf{F'}: &\quad \{4, 12, 24, 32\} \\
\mathbf{D}: &\quad \{5, 6, 13, 14, 33, 34, 41, 42\} \\
-\mathbf{D}: &\quad \{19, 20, 27, 28, 39, 40, 47, 48\}
\end{aligned} \tag{4.33}$$

4.7.2 Magnetic Symmetry Analysis

In this subsection we derive the irreducible representations and magnetic basis vectors for out periodicity-3 magnetic structure.

The primitive unit cell has 4 sites. In Fig. 1 we denote them as

$$\begin{aligned} \mathbf{r}_1 &= (0,0,0) \\ \mathbf{r}_2 &= (0,0,\frac{1}{6}) \\ \mathbf{r}_3 &= (-\frac{1}{4},-\frac{1}{4},\frac{1}{4}) \\ \mathbf{r}_4 &= (-\frac{1}{4},-\frac{1}{4},\frac{5}{12}), \end{aligned} \tag{4.34}$$

where all distances are measured in terms of fractions of the orthorhombic lattice vectors **a**, **b**, and **c**. The orthorhombic structural unit cell contains 4 primitive cells which can be obtained from the primitive unit cell using translations with lattice vectors $\boldsymbol{\rho}_p$ given by

$$\begin{aligned} \boldsymbol{\rho}_0 &= (0,0,0) \\ \boldsymbol{\rho}_1 &= (\frac{-1}{2},0,\frac{1}{2}) \\ \boldsymbol{\rho}_2 &= (0,-\frac{1}{2},\frac{1}{2}) \\ \boldsymbol{\rho}_3 &= (-\frac{1}{2},-\frac{1}{2},0). \end{aligned} \tag{4.35}$$

Thus, the positions of Ir sites shown in Fig. 4.1, labeled $\mathbf{r}_5$-$\mathbf{r}_8$, $\mathbf{r}_9$-$\mathbf{r}_{12}$ and $\mathbf{r}_{13}$-$\mathbf{r}_{16}$ can be obtained by adding, correspondingly, $\boldsymbol{\rho}_1$, $\boldsymbol{\rho}_2$, and $\boldsymbol{\rho}_3$ to sites $\mathbf{r}_1$ through $\mathbf{r}_4$. Generally, the position of any site can now be labelled as

$$\mathbf{r} = \mathbf{R} + \mathbf{r}_\alpha \tag{4.36}$$

where $\alpha = 1,...16$ is the position of the site inside the orthorhombic unit cell and $\mathbf{R} = m_1\mathbf{a} + m_2\mathbf{b} + m_3\mathbf{c}$ describes the position of the orthorhombic unit cell to which this site belongs.

The magnetic unit cell describing a periodicity-3 state is characterized by lattice vectors $\mathbf{A} = 3\mathbf{a}$, $\mathbf{B} = \mathbf{b}$, and $\mathbf{C} = \mathbf{c}$ and has 48 sites. The Fourier components, $\mathbf{M}_{q,n}$, of the magnetic moments at the four sites $n = 1,..4$ in the primitive cell can be now written as

$$\mathbf{M}_{\mathbf{q},n} = \sum_{\mathbf{R}} \sum_{p=0}^{3} \mathbf{S}(\mathbf{R}, \boldsymbol{\rho_p}, \mathbf{r}_n) e^{i\mathbf{q}\cdot(\mathbf{R}+\boldsymbol{\rho_p}+\mathbf{r}_n)} \tag{4.37}$$

Here we note that the site labeling in the Ref. [9] is different from our notations. Namely, the primitive unit cell used in Ref. [9] contains the following 4 sites (we denote notations from the Ref. [9] with a superscript c):

$$\begin{aligned} \mathbf{r}_1^c &= (\frac{1}{8},\frac{1}{8},z) \\ \mathbf{r}_2^c &= (\frac{1}{8},\frac{5}{8},\frac{3}{4}-z) \\ \mathbf{r}_3^c &= (\frac{3}{8},\frac{3}{8},1-z) \\ \mathbf{r}_4^c &= (\frac{3}{8},\frac{7}{8},\frac{1}{4}+z), \end{aligned} \tag{4.38}$$

where $z=\frac{17}{24}$. Therefore, there is the following mapping between the notations of the sites belonging to the primitive unit cell given in the Ref. [9] and our labeling of the sites presented in Fig.1: $\mathbf{r}_1^c \to \mathbf{r}_4$, $\mathbf{r}_2^c \to \mathbf{r}_{11}$, $\mathbf{r}_3^c \to \mathbf{r}_1$ and $\mathbf{r}_4^c \to \mathbf{r}_{10}$. In order to effectively compare the basic states describing our periodicity-3 magnetic orders to the ones used in Ref. [9], we relabel the sites of our magnetic unit cell according to this mapping.

We find the following results. At $\mathbf{q}=(1/3,0,0)$ (working in (h,k,l) units), all $\mathbf{M}_{\mathbf{q},n}=0$. At $\mathbf{q}=(2/3,0,0)$, we get

$$\begin{aligned} \mathbf{M}_{\mathbf{q},1} &= (iM_a, iM_b, M_c) \\ \mathbf{M}_{\mathbf{q},2} &= (-iM_a, iM_b, M_c) \\ \mathbf{M}_{\mathbf{q},2} &= (-iM_a, -iM_b, M_c) \\ \mathbf{M}_{\mathbf{q},4} &= (iM_a, -iM_b, M_c) \end{aligned} \tag{4.39}$$

At $\mathbf{q}=(4/3,0,0)$, we get

$$\begin{aligned} \mathbf{M}_{\mathbf{q},1} &= (-iM_a, -iM_b, M_c) \\ \mathbf{M}_{\mathbf{q},2} &= (iM_a, -iM_b, M_c) \\ \mathbf{M}_{\mathbf{q},2} &= (-iM_a, -iM_b, -M_c) \\ \mathbf{M}_{\mathbf{q},4} &= (iM_a, -iM_b, -M_c) \end{aligned} \tag{4.40}$$

Using the definition of the basis vectors as in Ref. [9]

$$F=\begin{bmatrix}1\\1\\1\\1\end{bmatrix}, G=\begin{bmatrix}1\\-1\\1\\-1\end{bmatrix}, C=\begin{bmatrix}1\\1\\-1\\-1\end{bmatrix}, A=\begin{bmatrix}1\\-1\\-1\\1\end{bmatrix},$$

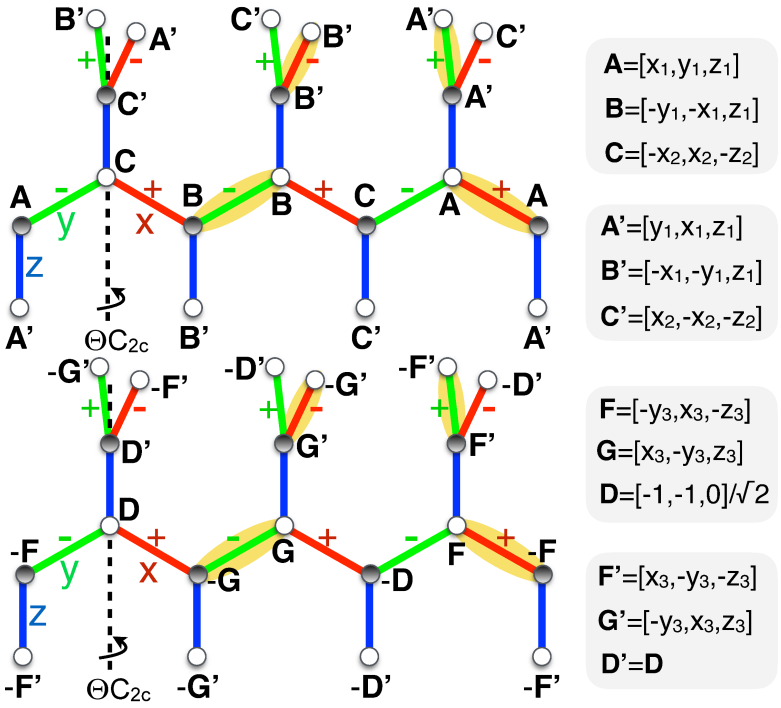

Figure 4.8: Geometry of the (top) K-dominant and (bottom) Γ-dominant state along a single zigzag chain. The spins on each site are given by the letters A, B, C (K-dominant state) or D, F, G (Γ-dominant state), with components given along the side panel.

we get

$$\mathbf{M}_{(2/3,0,0)} = (iM_aA, iM_bC, M_cF), \tag{4.41}$$

which is the Γ_4 irreducible representation and

$$\mathbf{M}_{(4/3,0,0)} = (-iM_aA, -iM_bF, M_cC), \tag{4.42}$$

which is the Γ_3 irreducible representation.

4.7.3 Explanation of why $\Delta = 0$ along the Γ-K Phase Boundary

In this subsection, we explain the origin of how $\Delta = 0$ at the point of first-order phase transition between the Γ and K dominant states in Fig. 4.7. At the point of

phase transition, not only are the ground state energies per site of the two states equal ($E_\Gamma = E_K$); but in addition, so are all linear combinations of the two states.

If we take the two states, shown in Fig. 4.8, we can create a linear combination by defining the spin at each site, $\mathbf{S}_{i_{LC}}$ as a combination of $\mathbf{S}_{i_K}$, the spin in the K-dominant state at that site, and $\mathbf{S}_{i_\Gamma}$, the spin in the Γ-dominant state at that site:

$$\mathbf{S}_{i_{LC}} = \cos\alpha\, \mathbf{S}_{i_K} + \sin\alpha\, \mathbf{S}_{i_\Gamma} \tag{4.43}$$

Furthermore, we can define the local field at each site in the same manner

$$\mathbf{h}_{i_{LC}} = \cos\alpha\, \mathbf{h}_{i_K} + \sin\alpha\, \mathbf{h}_{i_\Gamma} \tag{4.44}$$

and the energy of site i is $E_{LC_i} = \mathbf{S}_{i_{LC}} \cdot \mathbf{h}_{i_{LC}}$. At first glance, we will have cross-terms of the form $\cos\alpha \sin\alpha(\mathbf{S}_{i_K}\mathbf{h}_{i_\Gamma} + \mathbf{S}_{i_\Gamma}\mathbf{h}_{i_K})$

However, looking at the bottom panel of figure Fig. 4.8, we note that for every spin $\mathbf{S}_{i_\Gamma}$ along the top half of the chain (white dots labeled D, G, or F), there is a corresponding spin $\mathbf{S}_{j_\Gamma}$ (grey dots labeled -G, -D, or -F) along the bottom half of the chain pointing in the opposite direction. That is, $\mathbf{S}_{j_\Gamma} = -\mathbf{S}_{i_\Gamma}$.

Furthermore, the local fields at site i and j are equal in magnitude and point opposite in direction, $\mathbf{h}_{j_\Gamma} = -\mathbf{h}_{i_\Gamma}$. This can be seen in Fig. 4.8, if we look at the neighbors of any site i (D, F, or G) and the corresponding site j (-D, -F, or -G), we note that neighboring spins of j latter are equal in magnitude and point opposite in direction when compared to the corresponding neighboring spins of i. Naturally, this leads to the relationship $\mathbf{h}_{j_\Gamma} = -\mathbf{h}_{i_\Gamma}$.

If we look at the top panel of Fig. 4.8, we note that for every spin $\mathbf{S}_{i_K}$ along the top half of the chain (white dots labeled A, B, or C), there is a corresponding spin along the bottom half of the chain $\mathbf{S}_{j_K}$ (grey dots, also labeled A, B, or C) that points in the same direction. That is, $\mathbf{S}_{j_K} = \mathbf{S}_{i_K}$. Similarly, we find $\mathbf{h}_{j_K} = \mathbf{h}_{i_K}$

Referring back to Eq. 4.43, for every spin at site i, $\mathbf{S}_{i_{LC}} = \cos\alpha\, \mathbf{S}_{i_K} + \sin\alpha\, \mathbf{S}_{i_\Gamma}$ on the top half of the chain , we have the corresponding spin at site j

$$\mathbf{S}_{j_{LC}} = \cos\alpha\ \mathbf{S}_{i_K} - \sin\alpha\ \mathbf{S}_{i_\Gamma} \tag{4.45}$$

on the bottom half of the chain. The corresponding local field at site j is

$$\mathbf{h}_{j_{LC}} = \cos\alpha\ \mathbf{h}_{i_K} - \sin\alpha\ \mathbf{h}_{i_\Gamma} \tag{4.46}$$

We can use Eqs. 4.43, 4.44, 4.45, and 4.46 to calculate the sum:

$$\mathbf{S}_{i_{LC}} \cdot \mathbf{h}_{i_{LC}} + \mathbf{S}_{j_{LC}} \cdot \mathbf{h}_{j_{LC}} = 2(\cos^2 \alpha \, \mathbf{S}_{i_K} \cdot \mathbf{h}_{i_K} + \sin^2 \alpha \, \mathbf{S}_{i_\Gamma} \cdot \mathbf{h}_{i_\Gamma}) \tag{4.47}$$

and we note that the cross terms have canceled in Eq. 4.47. This can be generalized if we average the energy over all n sites. We find:

$$\begin{aligned} \frac{1}{N} \sum_n \mathbf{S}_{n_{LC}} \cdot \mathbf{h}_{n_{LC}} &= \frac{1}{N} \sum_n (\cos^2 \alpha \, \mathbf{S}_{n_K} \cdot \mathbf{h}_{n_K} + \sin^2 \alpha \mathbf{S}_{n_\Gamma} \cdot \mathbf{h}_{n_\Gamma}) \\ &= \cos^2 \alpha \, E_k + \sin^2 \alpha \, E_\Gamma \end{aligned} \tag{4.48}$$

In the case where $E_k = E_\Gamma$, Eq. 4.48 simplifies, and $E_{LC} = E_k = E_\Gamma$, regardless of how we pick α. Thus, whenever the K and Γ dominant states are equal in energy, there exists a continuous SO(2) symmetry defined by the parameter α, leading to the gapless modes like we see in Fig. 4.7. We note this is an "accidental zero," higher order corrections should increase the gap Δ to a finite value at this point.

Chapter 5

Conclusion and Discussion

In this dissertation I have shown how effective models can be employed to help our understanding of strongly correlated electron systems with orbital degrees of freedom. In this class of systems, emergent behavior such as superconductivity, orbital ordering, or magnetism may arise. In this dissertation, I focus on working with effective models to describe the magnetic properties of two particular compounds, $Fe_{1+y}Te$ and β-Li_2IrO_3.

In chapter 2, I begin by introducing $Fe_{1+y}Te$, and I ask the question "What is the magnetic ground state of the observed $\mathbf{Q}=(\pm\frac{\pi}{2},\frac{\pi}{2})$ order?" I briefly review the two candidates, the bicollinear and plaquette magnetic orders, both of which are consistent with the experimentally observed order. Interestingly, the plaquette state cannot be described by a single-$\mathbf{Q}$ state but instead requires a superposition of wavevectors $\mathbf{Q}=(\pm\frac{\pi}{2},\pm\frac{\pi}{2})$, and for this reason it has often been neglected in the literature. In fact, many possible magnetic ground states cannot be described by a single-$\mathbf{Q}$ wavevector, and like the plaquette state, are often overlooked in theoretical studies. Throughout the work presented in this dissertation I have been careful to allow for states with multiple-$\mathbf{Q}$ wavevectors.

In order to compare the bicollinear and plaquette magnetic orders beyond the level of the classical energy, I introduce one of the main techniques I employ throughout the dissertation, the Holstein-Primakoff transformation. This technique can be used to calculate the spin wave spectrum, which can be directly compared to the results of inelastic neutron scattering. In chapter 2, I employ the Holstein-Primakoff technique to calculate the magnon spectrum with $1/S$ corrections. I find that quantum fluctuations

select the plaquette state over the bicollinear state.

Unfortunately, the model I utilized in chapter 2 could not account for the phase transition the material underwent from a $\mathbf{Q}=(\pm\frac{\pi}{2},\frac{\pi}{2})$ magnetic order to a spiral order with $\mathbf{Q}=\pm(\frac{\pi}{2}-\delta,\frac{\pi}{2}-\delta)$ as excess iron y was increased. In chapter 3, I argued that our previous model described adequately the exchanges between the localized spins for small y; however, some electrons in $Fe_{1+y}Te$ remained itinerant due to orbital selective localization, which we must also account for. As excess iron y is increased, it contributes more electrons to the bands, increasing the chemical potential μ. In fact, we model increasing excess iron as a form of charge doping. The itinerant electrons interact with the local moments via Hund's coupling, and this leads to a long range RKKY interaction between the local moments which enhances or screens our various Heisenberg interactions. We note that similar models have been employed to describe the magnatites, whose effective couplings were also modified by charge doping.

Overall, we find that increasing y leads the RKKY interaction to enhance nearest neighbor and reduce further neighbor Heisenberg interactions, driving the system into the observed spiral order. Using our model, we are able to recreate the experimental phase diagram, and we further predict that for very small y the system will be driven into a stripe magnetic order. This framework, where localized moments live in a multiband correlated electron sea, will perhaps be useful in explaining the behaviors of other iron chalcogenides.

In chapter 4, I work to find the ground state of a J-K-Γ model of β-Li_2IrO_3. I begin by employing the Luttinger-Tisza method to find an approximate ground state. I find that while the Luttinger-Tisza method gives an state with an incommensurate propagation vector $\mathbf{Q}$, in a large portion of the phase diagram $\mathbf{Q}$ varies slowly, with $\mathbf{Q}\approx\frac{2}{3}\mathbf{B}_1$. I use the results of the Luttinger-Tisza method as an input for a numerical nonlinear Landau-Lifshitz-Gilbert equation. This technique is very powerful at reducing to zero the torque on each spin in a simulation, which guarantees the state found is a good local minimum. I found that the multiple-$\mathbf{Q}$ "period-3" solutions of the Landau-Lifshitz-Gilbert equation, which were commensurate in the enlarged magnetic Brillioun zone, were both lower in energy and more stable than incommensurate single-$\mathbf{Q}$ solutions found both in this work and by others. I found two different possible "period-3" ground states in the phase diagram, one of which, the K-dominant state, has not been found

by others. Furthermore, because the states two states I found are commensurate in the enlarged Brillioun zone; I was able to find both the linear spin wave spectrum and the dynamic structure factor, the first calculation of both for this system. As of yet, single crystal inelastic neutron scattering has not been performed for β-Li_2IrO_3. I note that once such data exists, it will be either directly confirm or refute my predictions.

In this dissertation, I show the power of effective models and the ease with which they can be utilized. Throughout, I have been able to explain and fit many experimental features with the models I have employed. However, I have also consistently gone a step further, making predictions when possible. I note that although $Fe_{1+y}Te$ and β-Li_2IrO_3 are very different systems, some techniques, such as calculating and examining the spin wave spectrum, have proven to be useful with both. However, more so than stick to any one technique, it has been my goal perform research in the exciting area in between microscopic theories and experimentally observed macroscopic properties through the use of phenomenological models. By working with well-justified low-energy models, employing multiple techniques towards the analysis of the model, connecting the results of these techniques, and always focusing on the most relevant details, I shed light on the behavior of $Fe_{1+y}Te$ and β-Li_2IrO_3.

It has been both challenging and rewarding to perform research on low-energy effective magnetic models of strongly correlated electron systems. The sub-field has has many future challenges which can be generically divided into creating effective models and testing the models' accuracy. We are seeing closer and closer cooperation between experimentalists and theorists, and also between different theorists using analytic and numerical methods, which has and will continue to lead to the creation of more and more phenomenological models. In fact, often several different groups propose multiple non-equivalent phenomenological models, which is a sign that the field is thriving and healthy. Thus, in the future, we will see increased demand for high quality research which works to connect low-energy models with the experimentally observed macroscopic properties.

References

[1] Y. Tokura and N. Nagaosa. Orbital physics in transition-metal oxides. *Science*, 288:462–468, 2000.

[2] Yoichi Kamihara, Takumi Watanabe, Masahiro Hirano, and Hideo Hosono. Iron-based layered superconductor la[o1-xfx]feas (x = 0.050.12) with tc = 26 k. *Journal of the American Chemical Society*, 130(11):3296–3297, 2008, http://dx.doi.org/10.1021/ja800073m. PMID: 18293989.

[3] J. G. Bednorz and K. A. Müller. Possible hightc superconductivity in the balacuo system. *Zeitschrift für Physik B Condensed Matter*, 64(2):189–193, 1986.

[4] D. N. Basov and Andrey V. Chubukov. Manifesto for a higher tc. *Nature Physics*, 7:272–276, 2011.

[5] Alexei Kitaev. Anyons in an exactly solved model and beyond. *Annals of Physics*, 321(1):2 – 111, 2006.

[6] G. Jackeli and G. Khaliullin. Mott insulators in the strong spin-orbit coupling limit: From heisenberg to a quantum compass and kitaev models. *Phys. Rev. Lett.*, 102:017205, Jan 2009.

[7] Simon Trebst. Kitaev materials. *arXiv:1701.07056*, 2017.

[8] KA Modic, Tess E Smidt, Itamar Kimchi, Nicholas P Breznay, Alun Biffin, Sungkyun Choi, Roger D Johnson, Radu Coldea, Pilanda Watkins-Curry, Gregory T McCandess, et al. Realization of a three-dimensional spin-anisotropic harmonic honeycomb iridate. *Nature communications*, 5, 2014.

[9] A. Biffin, R. D. Johnson, Sungkyun Choi, F. Freund, S. Manni, A. Bombardi, P. Manuel, P. Gegenwart, and R. Coldea. Unconventional magnetic order on the hyperhoneycomb kitaev lattice in $\beta-li_2iro_3$: Full solution via magnetic resonant x-ray diffraction. *Phys. Rev. B*, 90:205116, Nov 2014.

[10] A. Biffin, R. D. Johnson, I. Kimchi, R. Morris, A. Bombardi, J. G. Analytis, A. Vishwanath, and R. Coldea. Noncoplanar and counterrotating incommensurate magnetic order stabilized by kitaev interactions in $\gamma-li_2iro_3$. *Phys. Rev. Lett.*, 113:197201, Nov 2014.

[11] T. Takayama, A. Kato, R. Dinnebier, J. Nuss, H. Kono, L. S. I. Veiga, G. Fabbris, D. Haskel, and H. Takagi. Hyperhoneycomb iridate β-li_2iro_3 as a platform for kitaev magnetism. *Phys. Rev. Lett.*, 114:077202, Feb 2015.

[12] Alejandro Ruiz, Alex Frano, Nicholas P. Breznay, Itamar Kimchi, Toni Helm, Iain Oswald, Julia Y. Chan, R. J. Birgeneau, Z. Islam, and James G. Analytis. Kitaev materials. *arXiv:1703.02531*, 2017.

[13] H. K. Onnes. The resistance of pure mercury at helium temperatures. *Commun. Phys. Lab. Univ. Leiden*, 12:120+, 1911.

[14] J. Bardeen, L. N. Cooper, and J. R. Schrieffer. Theory of Superconductivity. *Physical Review*, 108:1175–1204, December 1957.

[15] L. N. Cooper. Bound Electron Pairs in a Degenerate Fermi Gas. *Physical Review*, 104:1189–1190, November 1956.

[16] J. Bardeen, L. N. Cooper, and J. R. Schrieffer. Microscopic Theory of Superconductivity. *Physical Review*, 106:162–164, April 1957.

[17] Kenji Ishida, Yusuke Nakai, and Hideo Hosono. To what extent iron-pnictide new superconductors have been clarified: A progress report. *Journal of the Physical Society of Japan*, 78(6):062001, 2009, http://dx.doi.org/10.1143/JPSJ.78.062001.

[18] Z. A. Ren, J. Yang, W. Lu, W. Yi, G. C. Che, X. L. Dong, L. L. Sun, and Z. X. Zhao. Superconductivity at 52 k in iron based f doped layered quaternary

compound pr[o1xfx]feas. *Materials Research Innovations*, 12(3):105–106, 2008, http://dx.doi.org/10.1179/143307508X333686.

[19] G. Wu, Y. L. Xie, H. Chen, M. Zhong, R. H. Liu, B. C. Shi, Q. J. Li, X. F. Wang, T. Wu, Y. J. Yan, J. J. Ying, and X. H. Chen. FAST TRACK COMMUNICATION: Superconductivity at 56 K in samarium-doped SrFeAsF. *Journal of Physics Condensed Matter*, 21(14):142203, April 2009.

[20] Hideo Hosono, Keiichi Tanabe, Eiji Takayama-Muromachi, Hiroshi Kageyama, Shoji Yamanaka, Hiroaki Kumakura, Minoru Nohara, Hidenori Hiramatsu, and Satoru Fujitsu. Exploration of new superconductors and functional materials, and fabrication of superconducting tapes and wires of iron pnictides. *Science and Technology of Advanced Materials*, 16(3):033503, 2015, http://dx.doi.org/10.1088/1468-6996/16/3/033503.

[21] Andrey Chubukov. *Itinerant Electron Scenario*, pages 255–329. Springer International Publishing, Cham, 2015.

[22] David C. Johnston. The puzzle of high temperature superconductivity in layered iron pnictides and chalcogenides. *Advances in Physics*, 59(6):803–1061, 2010, http://dx.doi.org/10.1080/00018732.2010.513480.

[23] Fa Wang and Dung-Hai Lee. The electron-pairing mechanism of iron-based superconductors. *Science*, 332(6026):200–204, 2011, http://science.sciencemag.org/content/332/6026/200.full.pdf.

[24] R. M. Fernandes, A. V. Chubukov, and J. Schmalian. What drives nematic order in iron-based superconductors? *Nat Phys*, 10(2):97–104, Feb 2014. Review.

[25] T. J. Liu, J. Hu, B. Qian, D. Fobes, Z. Q. Mao, W. Bao, M. Reehuis, S. A. J. Kimber, K. Prokes, S. Matas, D. N. Argyriou, A. Hiess, A. Rotaru, H. Pham, L. Spinu, Y. Qiu, V. Thampy, A. T. Savici, J. A. Rodriguez, and C. Broholm. From (pi,0) magnetic order to superconductivity with (pi,pi) magnetic resonance in fe1.02te1-xsex. *Nat Mater*, 9(9):718–720, Sep 2010.

[26] Shiliang Li, Clarina de la Cruz, Q. Huang, Y. Chen, J. W. Lynn, Jiangping Hu, Yi-Lin Huang, Fong-Chi Hsu, Kuo-Wei Yeh, Maw-Kuen Wu, and Pengcheng Dai.

First-order magnetic and structural phase transitions in $fe_{1+y}se_xte_{1-x}$. *Phys. Rev. B*, 79:054503, Feb 2009.

[27] Fengjie Ma, Wei Ji, Jiangping Hu, Zhong-Yi Lu, and Tao Xiang. First-principles calculations of the electronic structure of tetragonal α-fete and α-fese crystals: Evidence for a bicollinear antiferromagnetic order. *Phys. Rev. Lett.*, 102:177003, Apr 2009.

[28] Samuel Ducatman, Natalia B. Perkins, and Andrey Chubukov. Magnetism in parent iron chalcogenides: Quantum fluctuations select plaquette order. *Phys. Rev. Lett.*, 109:157206, Oct 2012.

[29] Samuel Ducatman, Rafael M. Fernandes, and Natalia B. Perkins. Theory of the evolution of magnetic order in $fe_{1+y}Te$ compounds with increasing interstitial iron. *Phys. Rev. B*, 90:165123, Oct 2014.

[30] Wei-Guo Yin, Chi-Cheng Lee, and Wei Ku. Unified picture for magnetic correlations in iron-based superconductors. *Phys. Rev. Lett.*, 105:107004, Sep 2010.

[31] Nicola Lanatà, Hugo U. R. Strand, Gianluca Giovannetti, Bo Hellsing, Luca de' Medici, and Massimo Capone. Orbital selectivity in hund's metals: The iron chalcogenides. *Phys. Rev. B*, 87:045122, Jan 2013.

[32] Gang Cao and Lance DeLong. Frontiers of 4d- and 5d-Transition Metal Oxides. *World Scientific Publishing Co. Pte. Ltd.*, 2013.

[33] William Witczak-Krempa, Gang Chen, Yong Baek Kim, and Leon Balents. Correlated Quantum Phenomena in the Strong Spin-Orbit Regime. *Ann. Rev. Cond. Matt. Phys.*, 5(1):57–82, 2014.

[34] Fa Wang and T. Senthil. Twisted hubbard model for sr_2iro_4: Magnetism and possible high temperature superconductivity. *Phys. Rev. Lett.*, 106:136402, Mar 2011.

[35] B. J. Kim, Hosub Jin, S. J. Moon, J.-Y. Kim, B.-G. Park, C. S. Leem, Jaejun Yu, T. W. Noh, C. Kim, S.-J. Oh, J.-H. Park, V. Durairaj, G. Cao, and E. Rotenberg.

Novel $J_{\text{eff}} = 1/2$ mott state induced by relativistic spin-orbit coupling in sr_2iro_4. *Phys. Rev. Lett.*, 101:076402, Aug 2008.

[36] John J. Randall, Lewis Katz, and Roland Ward. The preparation of a strontium-iridium oxide sr2iro41,2. *Journal of the American Chemical Society*, 79(2):266–267, 1957, http://dx.doi.org/10.1021/ja01559a004.

[37] G. Cao, J. Bolivar, S. McCall, J. E. Crow, and R. P. Guertin. Weak ferromagnetism, metal-to-nonmetal transition, and negative differential resistivity in single-crystal sr_2iro_4. *Phys. Rev. B*, 57:R11039–R11042, May 1998.

[38] Kevin O'Brien, Maria Hermanns, and Simon Trebst. Classification of gapless F_2 spin liquids in three-dimensional kitaev models. *Phys. Rev. B*, 93:085101, Feb 2016.

[39] Brent Perreault, Johannes Knolle, Natalia B. Perkins, and F. J. Burnell. Theory of raman response in three-dimensional kitaev spin liquids: Application to β- and $\gamma - \text{li}_2\text{iro}_3$ compounds. *Phys. Rev. B*, 92:094439, Sep 2015.

[40] Eric Kin-Ho Lee and Yong Baek Kim. Theory of magnetic phase diagrams in hyperhoneycomb and harmonic-honeycomb iridates. *Phys. Rev. B*, 91:064407, Feb 2015.

[41] Eric Kin-Ho Lee, Jeffrey G. Rau, and Yong Baek Kim. Two iridates, two models, and two approaches: A comparative study on magnetism in three-dimensional honeycomb materials. *Phys. Rev. B*, 93:184420, May 2016.

[42] M. D. Johannes and I. I. Mazin. Microscopic origin of magnetism and magnetic interactions in ferropnictides. *Phys. Rev. B*, 79:220510, Jun 2009.

[43] Johnpierre Paglione and Richard L. Greene. High-temperature superconductivity in iron-based materials. *Nat Phys*, 6(9):645–658, Sep 2010.

[44] M. M. Qazilbash, J. J. Hamlin, R. E. Baumbach, Lijun Zhang, D. J. Singh, M. B. Maple, and D. N. Basov. Electronic correlations in the iron pnictides. *Nat Phys*, 5(9):647–650, Sep 2009.

[45] A.V. Chubukov. Renormalization group analysis of competing orders and the pairing symmetry in fe-based superconductors. *Physica C: Superconductivity*, 469(9):640 – 650, 2009. Superconductivity in Iron-Pnictides.

[46] I.I. Mazin and J. Schmalian. Pairing symmetry and pairing state in ferropnictides: Theoretical overview. *Physica C: Superconductivity*, 469(9):614 – 627, 2009. Superconductivity in Iron-Pnictides.

[47] Valentin Stanev, Jian Kang, and Zlatko Tesanovic. Spin fluctuation dynamics and multiband superconductivity in iron pnictides. *Phys. Rev. B*, 78:184509, Nov 2008.

[48] Vladimir Cvetkovic and Zlatko Tesanovic. Valley density-wave and multiband superconductivity in iron-based pnictide superconductors. *Phys. Rev. B*, 80:024512, Jul 2009.

[49] I. Eremin and A. V. Chubukov. Magnetic degeneracy and hidden metallicity of the spin-density-wave state in ferropnictides. *Phys. Rev. B*, 81:024511, Jan 2010.

[50] P J Hirschfeld, M M Korshunov, and I I Mazin. Gap symmetry and structure of fe-based superconductors. *Reports on Progress in Physics*, 74(12):124508, 2011.

[51] A Chubukov. Pairing mechanism in fe based superconductors. *Annual review of Condensed Matter Physics*, 3(57), 2012.

[52] Ying Ran, Fa Wang, Hui Zhai, Ashvin Vishwanath, and Dung-Hai Lee. Nodal spin density wave and band topology of the feas-based materials. *Phys. Rev. B*, 79:014505, Jan 2009.

[53] R. M. Fernandes, A. V. Chubukov, J. Knolle, I. Eremin, and J. Schmalian. Preemptive nematic order, pseudogap, and orbital order in the iron pnictides. *Phys. Rev. B*, 85:024534, Jan 2012.

[54] Elihu Abrahams and Qimiao Si. Quantum criticality in the iron pnictides and chalcogenides. *Journal of Physics: Condensed Matter*, 23(22):223201, 2011.

[55] Cédric Weber and Frédéric Mila. Anticollinear magnetic order induced by impurities in the frustrated heisenberg model of pnictides. *Phys. Rev. B*, 86:184432, Nov 2012.

[56] O. J. Lipscombe, G. F. Chen, Chen Fang, T. G. Perring, D. L. Abernathy, A. D. Christianson, Takeshi Egami, Nanlin Wang, Jiangping Hu, and Pengcheng Dai. Spin waves in the $(\pi, 0)$ magnetically ordered iron chalcogenide $\mathrm{fe}_{1.05}\mathrm{Te}$. *Phys. Rev. Lett.*, 106:057004, Feb 2011.

[57] Igor A. Zaliznyak, Zhijun Xu, John M. Tranquada, Genda Gu, Alexei M. Tsvelik, and Matthew B. Stone. Unconventional temperature enhanced magnetism in $\mathrm{fe}_{1.1}\mathrm{Te}$. *Phys. Rev. Lett.*, 107:216403, Nov 2011.

[58] I. A. Zaliznyak, Z. J. Xu, J. S. Wen, J. M. Tranquada, G. D. Gu, V. Solovyov, V. N. Glazkov, A. I. Zheludev, V. O. Garlea, and M. B. Stone. Continuous magnetic and structural phase transitions in $\mathrm{fe}_{1+y}\mathrm{te}$. *Phys. Rev. B*, 85:085105, Feb 2012.

[59] Yoshikazu Mizuguchi and Yoshihiko Takano. Review of fe chalcogenides as the simplest fe-based superconductor. *Journal of the Physical Society of Japan*, 79(10):102001, 2010, http://dx.doi.org/10.1143/JPSJ.79.102001.

[60] Y. Xia, D. Qian, L. Wray, D. Hsieh, G. F. Chen, J. L. Luo, N. L. Wang, and M. Z. Hasan. Fermi surface topology and low-lying quasiparticle dynamics of parent $\mathrm{fe}_{1+x}\mathrm{Te/Se}$ superconductor. *Phys. Rev. Lett.*, 103:037002, Jul 2009.

[61] Alaska Subedi, Lijun Zhang, D. J. Singh, and M. H. Du. Density functional study of fes, fese, and fete: Electronic structure, magnetism, phonons, and superconductivity. *Phys. Rev. B*, 78:134514, Oct 2008.

[62] Rong Yu, Zhentao Wang, Pallab Goswami, Andriy H. Nevidomskyy, Qimiao Si, and Elihu Abrahams. Spin dynamics of a J_1-J_2-k model for the paramagnetic phase of iron pnictides. *Phys. Rev. B*, 86:085148, Aug 2012.

[63] Jiangping Hu, Bao Xu, Wuming Liu, Ning-Ning Hao, and Yupeng Wang. Unified minimum effective model of magnetic properties of iron-based superconductors. *Phys. Rev. B*, 85:144403, Apr 2012.

[64] Qimiao Si and Elihu Abrahams. Strong correlations and magnetic frustration in the high T_c iron pnictides. *Phys. Rev. Lett.*, 101:076401, Aug 2008.

[65] Jun Zhao, Dao-Xin Yao, Shiliang Li, Tao Hong, Y. Chen, S. Chang, W. Ratcliff, J. W. Lynn, H. A. Mook, G. F. Chen, J. L. Luo, N. L. Wang, E. W. Carlson, Jiangping Hu, and Pengcheng Dai. Low energy spin waves and magnetic interactions in $srfe_2as_2$. *Phys. Rev. Lett.*, 101:167203, Oct 2008.

[66] Dao-Xin Yao and E. W. Carlson. Magnetic excitations in the high-T_c iron pnictides. *Phys. Rev. B*, 78:052507, Aug 2008.

[67] Ari M. Turner, Fa Wang, and Ashvin Vishwanath. Kinetic magnetism and orbital order in iron telluride. *Phys. Rev. B*, 80:224504, Dec 2009.

[68] Philippe Sindzingre, Nic Shannon, and Tsutomu Momoi. Phase diagram of the spin-1/2 j 1 - j 2 - j 3 heisenberg model on the square lattice. *Journal of Physics: Conference Series*, 200(2):022058, 2010.

[69] Yuan-Yen Tai, Jian-Xin Zhu, Matthias J. Graf, and C. S. Ting. Fermi surface evolution and checker-board block-spin antiferromagnetism in $A_xfe_{2-y}se_2$. *Phys. Rev. B*, 86:134512, Oct 2012.

[70] Johannes Reuther, Peter Wölfle, Rachid Darradi, Wolfram Brenig, Marcelo Arlego, and Johannes Richter. Quantum phases of the planar antiferromagnetic $J_1 - J_2 - J_3$ heisenberg model. *Phys. Rev. B*, 83:064416, Feb 2011.

[71] Matthieu Mambrini, Andreas Läuchli, Didier Poilblanc, and Frédéric Mila. Plaquette valence-bond crystal in the frustrated heisenberg quantum antiferromagnet on the square lattice. *Phys. Rev. B*, 74:144422, Oct 2006.

[72] P. Chandra and B. Doucot. Possible spin-liquid state at large s for the frustrated square heisenberg lattice. *Phys. Rev. B*, 38:9335–9338, Nov 1988.

[73] Adriana Moreo, Elbio Dagotto, Thierry Jolicoeur, and José Riera. Incommensurate correlations in the t-j and frustrated spin-1/2 heisenberg models. *Phys. Rev. B*, 42:6283–6293, Oct 1990.

[74] Andrey Chubukov. First-order transition in frustrated quantum antiferromagnets. *Phys. Rev. B*, 44:392–394, Jul 1991.

[75] A. Tamai, A. Y. Ganin, E. Rozbicki, J. Bacsa, W. Meevasana, P. D. C. King, M. Caffio, R. Schaub, S. Margadonna, K. Prassides, M. J. Rosseinsky, and F. Baumberger. Strong electron correlations in the normal state of the iron-based $fese_{0.42}te_{0.58}$ superconductor observed by angle-resolved photoemission spectroscopy. *Phys. Rev. Lett.*, 104:097002, Mar 2010.

[76] Chen Fang, Bao Xu, Pengcheng Dai, Tao Xiang, and Jiangping Hu. Magnetic frustration and iron-vacancy ordering in iron chalcogenide. *Phys. Rev. B*, 85:134406, Apr 2012.

[77] Gia-Wei Chern, Rafael M. Fernandes, Rahul Nandkishore, and Andrey V. Chubukov. Broken translational symmetry in an emergent paramagnetic phase of graphene. *Phys. Rev. B*, 86:115443, Sep 2012.

[78] Wei Bao, Y. Qiu, Q. Huang, M. A. Green, P. Zajdel, M. R. Fitzsimmons, M. Zhernenkov, S. Chang, Minghu Fang, B. Qian, E. K. Vehstedt, Jinhu Yang, H. M. Pham, L. Spinu, and Z. Q. Mao. Tunable ($\delta\pi$, $\delta\pi$)-type antiferromagnetic order in α-fe(te,se) superconductors. *Phys. Rev. Lett.*, 102:247001, Jun 2009.

[79] E. E. Rodriguez, C. Stock, P. Zajdel, K. L. Krycka, C. F. Majkrzak, P. Zavalij, and M. A. Green. Magnetic-crystallographic phase diagram of the superconducting parent compound $fe_{1+x}te$. *Phys. Rev. B*, 84:064403, Aug 2011.

[80] Chris Stock, Efrain E. Rodriguez, Mark A. Green, Peter Zavalij, and Jose A. Rodriguez-Rivera. Interstitial iron tuning of the spin fluctuations in the non-superconducting parent phase $\mathbf{fe}_{1+x}\mathbf{Te}$. *Phys. Rev. B*, 84:045124, Jul 2011.

[81] Yoshikazu Mizuguchi, Kentaro Hamada, Kazuki Goto, Hiroshi Takatsu, Hiroaki Kadowaki, and Osuke Miura. Evolution of two-step structural phase transition in fe1+dte detected by low-temperature x-ray diffraction. *Solid State Communications*, 152(12):1047 – 1051, 2012.

[82] S. Rößler, Dona Cherian, W. Lorenz, M. Doerr, C. Koz, C. Curfs, Yu. Prots, U. K. Rößler, U. Schwarz, Suja Elizabeth, and S. Wirth. First-order structural

transition in the magnetically ordered phase of $fe_{1.13}te$. *Phys. Rev. B*, 84:174506, Nov 2011.

[83] C. Koz, S. Rößler, A. A. Tsirlin, D. Kasinathan, C. Börrnert, M. Hanfland, H. Rosner, S. Wirth, and U. Schwarz. Pressure-induced successive structural transitions and high-pressure tetragonal phase of $fe_{1.08}te$. *Phys. Rev. B*, 86:094505, Sep 2012.

[84] Cevriye Koz, Sahana Rößler, Alexander A. Tsirlin, Steffen Wirth, and Ulrich Schwarz. Low-temperature phase diagram of $fe_{1+y}te$ studied using x-ray diffraction. *Phys. Rev. B*, 88:094509, Sep 2013.

[85] D. Parshall, G. Chen, L. Pintschovius, D. Lamago, Th. Wolf, L. Radzihovsky, and D. Reznik. Competition between commensurate and incommensurate magnetic ordering in $fe_{1+y}te$. *Phys. Rev. B*, 85:140515, Apr 2012.

[86] E. E. Rodriguez, D. A. Sokolov, C. Stock, M. A. Green, O. Sobolev, Jose A. Rodriguez-Rivera, H. Cao, and A. Daoud-Aladine. Magnetic and structural properties near the lifshitz point in $fe_{1+x}te$. *Phys. Rev. B*, 88:165110, Oct 2013.

[87] Chen Fang, B. Andrei Bernevig, and Jiangping Hu. Theory of magnetic order in fe 1+ y te 1- x se x. *EPL (Europhysics Letters)*, 86(6):67005, 2009.

[88] G. Chen, S. Choi, and L. Radzihovsky. Magnetic orders, excitations, and phase transitions in $fe_{1+y}te$. *Phys. Rev. B*, 88:165117, Oct 2013.

[89] K Haule and G Kotliar. Coherenceincoherence crossover in the normal state of iron oxypnictides and importance of hund's rule coupling. *New Journal of Physics*, 11(2):025021, 2009.

[90] Aleksander L. Wysocki, Kirill D. Belashchenko, and Vladimir P. Antropov. Consistent model of magnetism in ferropnictides. *Nat Phys*, 7(6):485–489, Jun 2011.

[91] J. K. Glasbrenner, J. P. Velev, and I. I. Mazin. First-principles study of the minimal model of magnetic interactions in fe-based superconductors. *Phys. Rev. B*, 89:064509, Feb 2014.

[92] Alireza Akbari, Ilya Eremin, and Peter Thalmeier. Rkky interaction in the spin-density-wave phase of iron-based superconductors. *Phys. Rev. B*, 84:134513, Oct 2011.

[93] Alireza Akbari, Peter Thalmeier, and Ilya Eremin. Evolution of the multiband rudermankittelkasuyayosida interaction: application to iron pnictides and chalcogenides. *New Journal of Physics*, 15(3):033034, 2013.

[94] Fa Wang, Hui Zhai, and Dung-Hai Lee. Nodes in the gap function of lafepo, the gap function of the fe(se,te) systems, and the stm signature of the $s_{\pm}$ pairing. *Phys. Rev. B*, 81:184512, May 2010.

[95] Motoaki Hirayama, Takashi Miyake, and Masatoshi Imada. Derivation of static low-energy effective models by an ab initio downfolding method without double counting of coulomb correlations: Application to $srvo_3$, fese, and fete. *Phys. Rev. B*, 87:195144, May 2013.

[96] Yogesh Singh and P. Gegenwart. Antiferromagnetic mott insulating state in single crystals of the honeycomb lattice material na_2iro_3. *Phys. Rev. B*, 82:064412, Aug 2010.

[97] S Graser, T A Maier, P J Hirschfeld, and D J Scalapino. Near-degeneracy of several pairing channels in multiorbital models for the fe pnictides. *New Journal of Physics*, 11(2):025016, 2009.

[98] P M R Brydon, Maria Daghofer, and Carsten Timm. Magnetic order in orbital models of the iron pnictides. *Journal of Physics: Condensed Matter*, 23(24):246001, 2011.

[99] Ming-Cui Ding, Hai-Qing Lin, and Yu-Zhong Zhang. Hidden $(\pi, 0)$ instability as an itinerant origin of bicollinear antiferromagnetism in $fe_{1+x}te$. *Phys. Rev. B*, 87:125129, Mar 2013.

[100] N. B. Perkins and N. M. Plakida. Spin dynamics in the generalized ferromagnetic kondo model for manganites. *Theoretical and Mathematical Physics*, 120(3):1182–1193, 1999.

[101] F. Mancini, N.B. Perkins, and N.M. Plakida. Spin-wave dispersion softening in the ferromagnetic kondo lattice model for manganites. *Physics Letters A*, 284(6):286 – 293, 2001.

[102] G. Jackeli and N. B. Perkins. Doping dependence of the exchange energies in bilayer manganites: Role of orbital degrees of freedom. *Phys. Rev. B*, 65:212402, May 2002.

[103] I. Paul. Magnetoelastic quantum fluctuations and phase transitions in the iron superconductors. *Phys. Rev. Lett.*, 107:047004, Jul 2011.

[104] Jeffrey G. Rau, Eric Kin-Ho Lee, and Hae-Young Kee. Spin-Orbit Physics Giving Rise to Novel Phases in Correlated Systems: Iridates and Related Materials. *Ann. Rev. Cond. Matt. Phys.*, 7:195, 2016.

[105] Ji ří Chaloupka, George Jackeli, and Giniyat Khaliullin. Kitaev-heisenberg model on a honeycomb lattice: Possible exotic phases in iridium oxides A_2iro$_3$. *Phys. Rev. Lett.*, 105:027204, Jul 2010.

[106] Zohar Nussinov and Jeroen van den Brink. Compass models: Theory and physical motivations. *Rev. Mod. Phys.*, 87:1–59, Jan 2015.

[107] Yogesh Singh, S. Manni, J. Reuther, T. Berlijn, R. Thomale, W. Ku, S. Trebst, and P. Gegenwart. Relevance of the heisenberg-kitaev model for the honeycomb lattice iridates A_2iro$_3$. *Phys. Rev. Lett.*, 108:127203, Mar 2012.

[108] X. Liu, T. Berlijn, W.-G. Yin, W. Ku, A. Tsvelik, Young-June Kim, H. Gretarsson, Yogesh Singh, P. Gegenwart, and J. P. Hill. Long-range magnetic ordering in na$_2$iro$_3$. *Phys. Rev. B*, 83:220403, Jun 2011.

[109] R. D. Johnson, S. C. Williams, A. A. Haghighirad, J. Singleton, V. Zapf, P. Manuel, I. I. Mazin, Y. Li, H. O. Jeschke, R. Valentí, and R. Coldea. Monoclinic crystal structure of $\alpha - \mathrm{rucl}_3$ and the zigzag antiferromagnetic ground state. *Phys. Rev. B*, 92:235119, Dec 2015.

[110] S. C. Williams, R. D. Johnson, F. Freund, Sungkyun Choi, A. Jesche, I. Kimchi, S. Manni, A. Bombardi, P. Manuel, P. Gegenwart, and R. Coldea. Incommensurate counterrotating magnetic order stabilized by kitaev interactions in the layered honeycomb $\alpha-li_2iro_3$. *Phys. Rev. B*, 93:195158, May 2016.

[111] Hong-Chen Jiang, Zheng-Cheng Gu, Xiao-Liang Qi, and Simon Trebst. Possible proximity of the mott insulating iridate na_2iro_3 to a topological phase: Phase diagram of the heisenberg-kitaev model in a magnetic field. *Phys. Rev. B*, 83:245104, Jun 2011.

[112] Lukas Janssen, Eric C. Andrade, and Matthias Vojta. Honeycomb-lattice heisenberg-kitaev model in a magnetic field: Spin canting, metamagnetism, and vortex crystals. *Phys. Rev. Lett.*, 117:277202, Dec 2016.

[113] Gia-Wei Chern, Yuriy Sizyuk, Craig Price, and Natalia B. Perkins. Kitaev-Heisenberg model in a magnetic field: order-by-disorder and commensurate-incommensurate transitions. *arXiv:1611.03436*, 2016.

[114] Ioannis Rousochatzakis, Ulrich K. Rössler, Jeroen van den Brink, and Maria Daghofer. Kitaev anisotropy induces mesoscopic F_2 vortex crystals in frustrated hexagonal antiferromagnets. *Phys. Rev. B*, 93:104417, Mar 2016.

[115] Michael Becker, Maria Hermanns, Bela Bauer, Markus Garst, and Simon Trebst. Spin-orbit physics of $j = \frac{1}{2}$ mott insulators on the triangular lattice. *Phys. Rev. B*, 91:155135, Apr 2015.

[116] Jeffrey G. Rau, Eric Kin-Ho Lee, and Hae-Young Kee. Generic spin model for the honeycomb iridates beyond the kitaev limit. *Phys. Rev. Lett.*, 112:077204, Feb 2014.

[117] Johannes Reuther, Ronny Thomale, and Stephan Rachel. Spiral order in the honeycomb iridate li_2iro_3. *Phys. Rev. B*, 90:100405, Sep 2014.

[118] Yuriy Sizyuk, Craig Price, Peter Wölfle, and Natalia B. Perkins. Importance of anisotropic exchange interactions in honeycomb iridates: Minimal model for zigzag antiferromagnetic order in na_2iro_3. *Phys. Rev. B*, 90:155126, Oct 2014.

[119] Itamar Kimchi, James G. Analytis, and Ashvin Vishwanath. Three-dimensional quantum spin liquids in models of harmonic-honeycomb iridates and phase diagram in an infinite-D approximation. *Phys. Rev. B*, 90:205126, Nov 2014.

[120] Ioannis Rousochatzakis, Johannes Reuther, Ronny Thomale, Stephan Rachel, and N. B. Perkins. Phase diagram and quantum order by disorder in the kitaev K_1-K_2 honeycomb magnet. *Phys. Rev. X*, 5:041035, Dec 2015.

[121] Ioannis Rousochatzakis and Natalia B. Perkins. Classical spin liquid instability driven by off-diagonal exchange in strong spin-orbit magnets. *Phys. Rev. Lett.*, 118:147204, Apr 2017.

[122] Heung-Sik Kim, Yong Baek Kim, and Hae-Young Kee. Revealing frustrated local moment model for pressurized hyperhoneycomb iridate: Paving the way toward a quantum spin liquid. *Phys. Rev. B*, 94:245127, Dec 2016.

[123] Itamar Kimchi, Radu Coldea, and Ashvin Vishwanath. Unified theory of spiral magnetism in the harmonic-honeycomb iridates α, β, and $\gamma\,\mathrm{li_2iro_3}$. *Phys. Rev. B*, 91:245134, Jun 2015.

[124] Itamar Kimchi and Radu Coldea. Spin dynamics of counterrotating kitaev spirals via duality. *Phys. Rev. B*, 94:201110, Nov 2016.

[125] J. M. Luttinger and L. Tisza. Theory of dipole interaction in crystals. *Phys. Rev.*, 70:954–964, Dec 1946.

[126] D. B. Litvin. The luttinger-tisza method. *Physica*, 77:205–219, 1974.

[127] C. Serpico, I. D. Mayergoyz, and G. Bertotti. Chiral magnetism and helimagnons in a pyrochlore antiferromagnet. *Journal of Applied Physics*, 89:6991, 2001.

[128] Masahito Mochizuki, Nobuo Furukawa, and Naoto Nagaosa. Theory of electromagnons in the multiferroic mn perovskites: The vital role of higher harmonic components of the spiral spin order. *Phys. Rev. Lett.*, 104:177206, Apr 2010.

[129] Oleg Janson, Ioannis Rousochatzakis, Alexander A. Tsirlin, Marilena Belesi, Andrei A. Leonov, Ulrich K. Roessler, Jeroen van den Brink, and Helge Rosner. The

quantum nature of skyrmions and half-skyrmions in Cu2OSeO3. *Nature Communications*, 5:6376, 2014.

[130] Eunsong Choi, Gia-Wei Chern, and Natalia B. Perkins. Helimagnons in a chiral ground state of the pyrochlore antiferromagnets. *EPL*, 101:37004, Feb 2013.

[131] Eunsong Choi, Gia-Wei Chern, and Natalia B. Perkins. Chiral magnetism and helimagnons in a pyrochlore antiferromagnet. *Phys. Rev. B*, 87:054418, Feb 2013.

Appendix A

Glossary and Acronyms

Care has been taken in this thesis to minimize the use of jargon and acronyms, but this cannot always be achieved. This appendix defines jargon terms in a glossary, and contains a table of acronyms and their meaning.

A.1 Glossary

the abundant energetic particles originating outside of the Earth's atmosphere.

- **Strongly Correlated Electron System** – A system which cannot be modelled with a single-particle description due to strong electron-electron repulsion. atmosphere.
- **Stripe Order** – A magnetic order where neighboring sites in one direction align ferromagnetically (forming "stripes"), and neighboring sites in the the perpendicular direction align antiferromagnetically.
- **Plaquette Order** – sometimes abbreviated ODS (Orthogonal Double Stripe), a magnetic order found in square lattice where four neighboring sites, forming a square, align ferromagnetically, and these "plaquettes" then tile antiferromagnetically.
- **Bicollinear Order** – sometimes abbreviated DDS (Diagonal Double Stripe), a magnetic order found in square lattices where spins along ferromagnetically along

one of the diagonal directions, and two diagonals in a row align in this same ferromagnetic pattern. These ferromagnetic stripes are then tiled antiferromagnetically.

- **Spiral Order** – a magnetic order where neighboring spins rotate relative to each other by a fixed "pitch angle" θ.
- **"Period 3" State** – Two different magnetic orders we found modelling β-Li_2IrO_3 where, a particular spin configuration repeats itself when we translate by $3\mathbf{A}_1$.
- **Goldstone Mode** – A branch of a spectrum that becomes gapless due to the existence of a continuous symmetry.
- **RKKY Interaction** – The RudermanKittelKasuyaYosida (RKKY) interaction is a long range interaction between local moments which occurs due to their mutual interactions with itinerant electrons.

A.2 Acronyms

Table A.1: Acronyms

Acronym	Meaning
FeSC	Iron Based Superconductor
SOC	Spin-Orbit Coupling
SDW	Spin-Density Wave
FS	Fermi Surface
BZ	Brillioun Zone
RPA	Random Phase Approximation
ARPES	angle-resolved photoemission spectroscopy
IC	incommensurate
LT	Luttinger-Tisza
LLG	Landau-Lifshitz-Gilbert equation
LSW	Linear Spin Wave